DABLE: a Facility for Measuring Fission Product Transport in Gas-cooled Reactors

by

Jerry Lynn Martin

S.B. Nuclear Eng., MIT (1987)
S.M. Nuclear Eng., MIT (1987)

Submitted to the Department of Nuclear Engineering
in Partial Fulfillment of the Requirements for the Degree of

Doctor of Philosophy in Nuclear Engineering

at the

Massachusetts Institute of Technology

June 1991

Signature of Author____ _____
Department of Nuclear Engineering
May,1991

Certified by_____
Lawrence M. Lidsky
Professor of Nuclear Engineering
Thesis Supervisor

Certified by____
David D. Lanning
Professor of Nuclear Engineering
Thesis Reader

Certified by_____
Allan Henry
Chairman, Department Committee on Graduate Students

DABLE: a Facility for Measuring Fission Product Transport in Gas-cooled Reactors

by

Jerry L. Martin

Submitted to the Department of Nuclear Engineering
on May 9, 1991 in partial fulfillment of the
requirements for the degree of Doctor of Philosophy in
Nuclear Engineering

ABSTRACT

A facility for the investigation of fission product transport in gas-cooled reactors has been developed. This facility, the Deposition and Blowdown/Liftoff Experiment (DABLE), is an out-of pile loop built at the Massachusetts Institute of Technology. The loop is designed to simulate the conditions typical of modular gas reactor heat exchangers. The loop consists of a 8 m length of 25 mm diameter pipe with a helium circulator, heaters and a fission product source.

The loop is designed to be capable of near-isothermal operation at pressures up to 8 MPa, and temperatures to 700°C. Fission product deposition on the walls is measured *in-situ*, in real time, by a movable gamma detector array. As part of the work, a high temperature helium circulator has been developed. The current version is designed for operation at > 500°C and 8 MPa. Planned modifications will increase the operating temperature to 700°C. This circulator has been used to circulate helium at 5.4 MPa and 300°C at speeds of up to 25 m/s in a 2.4 cm ID test section. The circulator is an electric motor driven, centrifugal machine with a 125 mm diameter impeller, 0.0186 actual m^3/sec flow rate, absorbing 1.1 kW at 20,000 rpm. The loop atmosphere is monitored by a quadrupole RGA system using a pressure regulator and a fused quartz capillary to reduce the loop pressure before sampling. The loop has been constructed and initial flow and temperature testing have been completed.

The DABLE loop provides a unique and flexible facility for investigating the transport of fission products in gas-cooled reactors. The design eliminates the need for large heat exchangers, leading to a substantially less expensive and simpler facility than earlier test loops. Tightly integrated data acquisition and control software allows automated operation. By providing a platform for the generation of very well characterized data on basic deposition and lift-off physics, it will support the development of improved plateout and lift-off models and computer codes.

Thesis supervisor:

Lawrence M. Lidsky	Title: Professor of Nuclear Engineering
David D. Lanning	Title: Professor of Nuclear Engineering

ACKNOWLEDGEMENTS

Despite the one author listed on the title page, no thesis is the work of a single individual, and this one is no exception. The work described in these pages was shaped, guided, and assisted by colleagues and friends scattered about MIT and across two continents. I cannot even attempt to list all those who have helped me in my efforts at the Institute, but perhaps there is some space here to list some that had the greatest influence on me.

I give much of the credit for the direction I have taken in academia to Professor Ron Ballinger, whose friendship and guidance shaped my undergraduate career and set me firmly on the path of experimental research. Under his tutelage I experienced some of my greatest successes; for that I will always remain in his debt.

Professor Ballinger took me on as a UROP student when I was a wide-eyed freshman, and introduced me to experimental work. I was able to share that experience from the other side with the string of UROP students who assisted me in my own research. Bhavya Lal and Namuk Cho gave me valuable assistance in the early stages of the project. Much of the success of the mechanical systems in the loop may be directly attributed to Nathan Getrich and Steve Derezinski, whose able assistance, insight, and engineering skill made difficult jobs enjoyable, and setbacks tolerable.

I must give special thanks to Professor Lidsky, my thesis advisor. Working with him gave me an education in ethics which may turn out to be as important as my Ph.D. His insistence on integrity, on refusing to get caught up in the party line, has served me in good stead. His advice on oral presentations–"Tell them what you know; tell them what you don't know." remains a monument of simplicity in a complex world. Lidsky had faith in me and my work when I had lost mine. Without his support, I might have been overwhelmed by the endless series of setbacks we seemed to suffer.

I would also like to give special thanks to Heinz Nabielek, of KFA, Jülich West Germany. He treated me as a colleague and friend, introduced me to fuel failure modelling, and made my stay in Germany a richly rewarding experience. He also was also the most important contributor of data and references to my research.

Throughout my career as a graduate student, the single most joyful aspect of life has been the time spent with my wife, Christine. She has contributed enormously to my health and happiness, edited my writing, checked my calculations, and helped me solve many a vexing problem. Her skill as an engineer and her love as a friend have contributed equally to my success.

This research was performed under appointment to the Nuclear Engineering & Health Physics Fellowship Program administered by Oak Ridge Associated Universities for the U.S. Department of Energy. Additional funding was provided by the DOE through Oak Ridge National Laboratories.

TABLE OF CONTENTS

ABSTRACT 2
ACKNOWLEDGEMENTS 3
TABLE OF CONTENTS 4
List of Figures 6
List of Tables 8
Nomenclature 9

THE HTGR 10
1.1. Introduction 10
1.2. Particle fuels 10
1.3. German design 12
1.4. U.S. Design 15
1.5. Direct Brayton Cycle designs 15
1.6. Safety of MHTGR's 16
1.6.1. fuel failure 16
1.6.2. depressurization accident source term 17

FISSION PRODUCT TRANSPORT IN HTGR'S 20
2.1 Fission Product Transport in HTGR's 20
2.2 Theory 20
2.2.1 Deposition 20
2.2.2 Lift-off 23
2.3 Observation 30
2.3.1 plateout probes 30
2.3.2 VAMPYR I & II 31
2.4 Experimental studies 32
2.4.1 GA loop 32
2.4.2 Comedie 34
2.4.3 LAMINAR 35

AN OVERVIEW OF THE DABLE LOOP DESIGN 38
3.1. DABLE System Overview 38
3.1.1. History 38
3.1.2. Goals 38
3.1.3. major systems 40

SELECTION OF THE OPERATING ENVELOPE 45
4.1 Scaling Issues 45
4.2 Issues of Geometric Similarity 45
4.2.1 Importance of Boundary Layer Thickness 46
4.3 Flow Similiarity 47
4.3.1 Controlling Parameters for Deposition 47
4.3.2 Controlling Parameters for Lift-off 48
4.4 Selection of Model Parameters 48
4.4.1 Operating Envelope 48

DESIGN OF THE CIRCULATOR 53
5.1. A Scoping-Level Discussion of the Helium Circulator 53
5.2. Detailed Aerodyamic Design of the Helium Circulator 57
5.2.1. Enthalpy rise 58

5.2.2. Specific speed 59
5.2.3. Inlet Velocity 59
5.2.4. Outlet velocity diagram 59
5.2.5. Radial-diffuser stability 60
5.2.6. Scroll 61
5.3. Mechanical Design of the Circulator 61
5.3.1. Pressure Vessel 63
5.3.2. Circulator Housing and Motor Support Structure 73
5.3.3. Drive System 74
5.3.4. Bearing System 79

OTHER LOOP SUBSYSTEMS 81
6.1. Temperature Measurement and Control 81
6.1.1. System Description 81
6.1.2. Thermocouple Locations 81
6.1.3. Wall and Gas Temperature Comparison 82
6.1.4. Signal Processing 83
6.1.5. Accuracy 84
6.2. Gas Purity Measurement and Control 85
6.2.1. Gaseous Impurities in HTGR Coolants 85
6.2.2. Gaseous Impurity Measurement in the DABLE Loop 86
6.2.3. Gaseous Impurity Control in the DABLE Loop 91
6.3. Flow Rate Measurement and Control 92
6.4. Iodine Source 93
6.5. Gamma Detection 97
6.5.1. Optimization of the detector geometry 98
6.5.2. Selection of the isotopes 102
6.5.3. Prediction of detector system performance 103
6.5.4. Detector Mechanical Systems 105
6.6. Safety 105
6.7. Data Acquisition and Control Software 107

SOME EXPERIMENTAL RESULTS 110
7.1 Shakedown testing 110
7.1.1 Circulator map 110
7.1.2 Gas Purity measurement 127

RECOMENDATIONS 130
8.1 Improvements to existing systems 130
8.2 Additions to loop capabilities 133
8.3 Proposed experiments 137

SUMMARY AND CONCLUSIONS 139

APPENDICIES
Calculations Supporting the Pressure Vessel Design 142
Analysis of Flow Measurement Differences 146

REFERENCES 149

List of Figures

Figure 1.1 Coated fuel particle, ... 11
Figure 1.2 The HTR Modul, ... 14

Figure 2.1 Correlation between dust and fission product concentration in AVR, ... 25
Figure 2.2 Effect of coherent structures in the wall layers on the sublayer, ... 28
Figure 2.3 The contact of an elastic sphere with an elastic flat surface (exaggerated), ... 29
Figure 2.4 Cs Plateout Distribution in the GA Loop, ... 33
Figure 2.5 Cs Plateout Distribution in the GA Loop (Dust Added), ... 34

Figure 3.1 DABLE Loop Elevation (Schematic), ... 42
Figure 3.2 Top view of NW13-225, ... 43
Figure 3.3 DABLE Loop elevation with hot cell, ... 44

Figure 4.1 Re* = 1 at various pressure ratios P*, ... 49
Figure 4.2 The curves Re*=1 and t*=1 on the V*-D* plane, ... 50
Figure 4.3 Operating Envelope, ... 51

Figure 5.1 Outlet Velocity Diagram, ... 60
Figure 5.2 Velocity Triangles at Blade Inlet, ... 62
Figure 5.3 Pressure Vessel for Immersed Motor Circulator, ... 65
Figure 5.4 Pressure Vessel, ... 66
Figure 5.5 Pressure Vessel Location in Loop, ... 67
Figure 5.6 Cross-section of Nozzles, ... 70
Figure 5.7 FEM Analysis of Heat Transfer in the Nozzles, ... 71
Figure 5.8 Pressure vessel internal insulation., ... 73

Figure 6.1 Thermocouple attachment to pipe wall., ... 82
Figure 6.2. Signal Processing with Multiplexer Before Isolation Amplifiers, ... 84
Figure 6.3. Signal Processing with Multiplexer after Isolation Amplifiers, ... 85
Figure 6.4 RGA Scan of room air, ... 88
Figure 6.5 RGA Scan of Vacuum System Background, ... 90
Figure 6.6 RGA Scan of Loop Atmosphere with Background Subtracted, ... 91
Figure 6.7 Flow Velocity vs Circulator rpm, ... 94
Figure 6.8 Vapor Pressure of Iodine above Iron, ... 96
Figure 6.9 High Pressure Iodine Source (schematic), ... 97
Figure 6.10 Detector Model, ... 99
Figure 6.11 Solid angle for a source in region II, ... 100
Figure 6.12 Solid angle for a source in region III, ... 101
Figure 6.13 View factor for sources on the detector axis vs distance from detector center, ... 101
Figure 6.14 Interface to the Controller Code, ... 109

Figure 7.1 Pitot tube and turbine flow meter readings, ... 115
Figure 7.2 Ratio of pitot tube to turbine flow meter measured velocity, ... 116
Figure 7.3 Hysteresis in the pitot tube readings, ... 117
Figure 7.4 Example Circulator Map, ... 118
Figure 7.5 Variation of rpm at constant voltage, ... 119
Figure 7.6 Circulator Map at 1.82 MPa, 105°C, ... 120
Figure 7.7 Circulator Map at 3.5 MPa, 236°C, ... 121
Figure 7.8 Partial circulator map at 5.34 MPa, 300°C, ... 122

Figure 7.9 Flow rate vs system pressure, ... 123
Figure 7.10 Flow vs rpm at two pressures, ... 124
Figure 7.11 Flow rate vs circulator speed at 5.34 MPa, and 290°C, ... 125
Figure 7.12 Predicted circulator performance at 6 MPa, 350°C, ... 126
Figure 7.13 Background in the RGA Vacuum Chamber, ... 128
Figure 7.14 Loop Atmosphere with background subtracted, ... 129

Figure 8.1 Alignment Points in the Current Housing Design, ... 132
Figure 8.2 Revised Circulator Housing, ... 134
Figure 8.3 New Impeller Shaft Design, ... 135
Figure 8.4 Assembly Drawing for Updated Circulator and Bearing Housing, ... 136

List of Tables

Table 1.1 Fuel Failure Probabilities, ... 17
Table 1.2 Limits on radionuclide releases during accidents, ... 18

Table 2.1 Parameters for the evaluation of mass transfer coefficients,..... 22
Table 2.2 Fission product concentrations in the AVR hot gas, ... 32
Table 2.3 Comparison of Operating Conditions for GA Deposition Loop and 1160 MWe HTGR, ... 32
Table 2.4 Characteristics of COMEDIE Loop, ... 35

Table 5.1 Design Goals: Conditions at Design Point, ... 55
Table 5.2 Design Goals and Selected Blade Geometry (Conditions at Design Point), ... 58
Table 5.3 Principle Dimensions and Operating Parameters of the DABLE Circulator, .. 63
Table 5.4 Comparison of electric motor technologies, ... 78

Table 6.1 Thermocouple Locations and Connections,..... 81
Table 6.2 Gaseous contaminants in MGR primary coolant, ... 86
Table 6.3 Regions in the detector model, ... 99
Table 6.4 Isotopes considered for use in deposition experiments, ... 103

Table 7.1 Preliminary Analysis of Loop Gas Composition, ... 127

Nomenclature

A	Area	β	cohesive force constant
a,b	constants	η	efficiency
C_θ	tangential component of velocity	ϕ	flow coefficient
C_x	axial velocity	σ	shear ratio
c_p	specific heat	θ	$T - T_\infty$
D,d	diameter	τ	shear stress
$\mathcal{D}$	diffusivity	ρ	density
E	Young's modulus	ν	kinematic viscosity
g	mass transfer coefficient	ω_n	natural frequency of vibration
h	heat transfer coefficient		
h_0	total enthalpy	*Sh*	Sherwood Number
k	thermal conductivity	*Sc*	Schmidt Number
L	Length	*Re*	Reynolds Number
m	mass		
$\dot{m}$	mass flow rate	*MWth*	Megawatt thermal
N	rotational speed, rpm	*MWe*	Megawatt electric
N_s	non-dimensional specific speed		
P	Perimeter	*AGR*	Advanced Gas Reactor
P,p	pressure or proability	*AVR*	Arbeitsgemeinschaft VersuchsReaktor
Q	potential well height	*DOE*	Department of Energy
r	radius	*FRG*	Federal Republic of Germany
R	resuspension rate, gas constant	*GA*	General Atomics
t	time	*FIMA*	Fissions in Initial Metal Atoms
T	temperature	*FSV*	Fort Saint Vrain
u	velocity, rotor peripheral speed	*THTR*	Thorium HochTemperature Reaktor
$\dot{V}$	volumetric flow rate		
V_0	nominal test section velocity		
v	velocity		
$\dot{W}$	power		
Z	number of blades		

Chapter 1

THE HTGR

1.1. Introduction

In an age of rising fossil fuel prices, increased concern for the environment, and a pervasive dissatisfaction with the current generation of nuclear power plants, it seems that the nuclear power industry must adapt or become extinct. A number of "next-generation" power plants have been proposed; each has been received with varying degrees of interest or apathy. Some engineers call for an "evolutionary" development of the current generation of light water reactors, others for a break with existing technology and the adoption of "passively safe" designs. Whatever their background, analysts and engineers alike agree that the new designs must satisfy a few key criteria:

- It should be relatively small (<600 MWe).
- It must be easier to license.
- It should have features to enhance availiabilty.
- It must be economic.

One such reactor which promises to meet these criteria is the Modular High Temperature Gas-cooled Reactor (MHTGR or MGR). The MGR, as designed in both the US and Germany is a small (<350 MWth), helium-cooled, graphite-moderated reactor which incorporates a number of passive safety features.

Prominent among these features is a safety philosophy which relies on a mechanistic prediction of fission product release during design basis accidents. This thesis describes the design and development of an experimental facility which will aid in the development of these mechanistic predictions.

1.2. Particle fuels

Any discussion of MGR's must of necessity begin with their unique fuel form, for it is directly from the properties of this fuel that the the reactor's most significant features derive. The fuel for MGR's consists of microscopic particles of UO_2 or UCO, surrounded by layers of pyrolytic carbon and silicon carbide. The structure of one of these particles is shown in Figure 1.1. The kernel is a 90% dense, UO_2 or UCO sphere with a diameter of

500 μm. [S2] It is surrounded by a low density pyrocarbon "buffer" layer which provides expansion space for the fission gases and helps stop the recoiling fission products from reaching the SiC layer. Outside the buffer layer, a thin high-density pyrocarbon layer is deposited. This layer protects the kernel during the SiC deposition process and also serves as an additional barrier for fission gas release. The next layer is a SiC layer, which is the primary fission product retention boundary. The diffusion coefficients of most of the fission products in SiC at temperatures below 1800°C are negligible[1]. SiC also retains its structural strength at high temperatures, allowing particles of this design to reach burnups in excess of 25% FIMA. Outside the SiC layer, a second high-density pyrocarbon layer serves as a gaseous fission product boundary and protects the brittle surface of the SiC layer from stress-raising scratches.

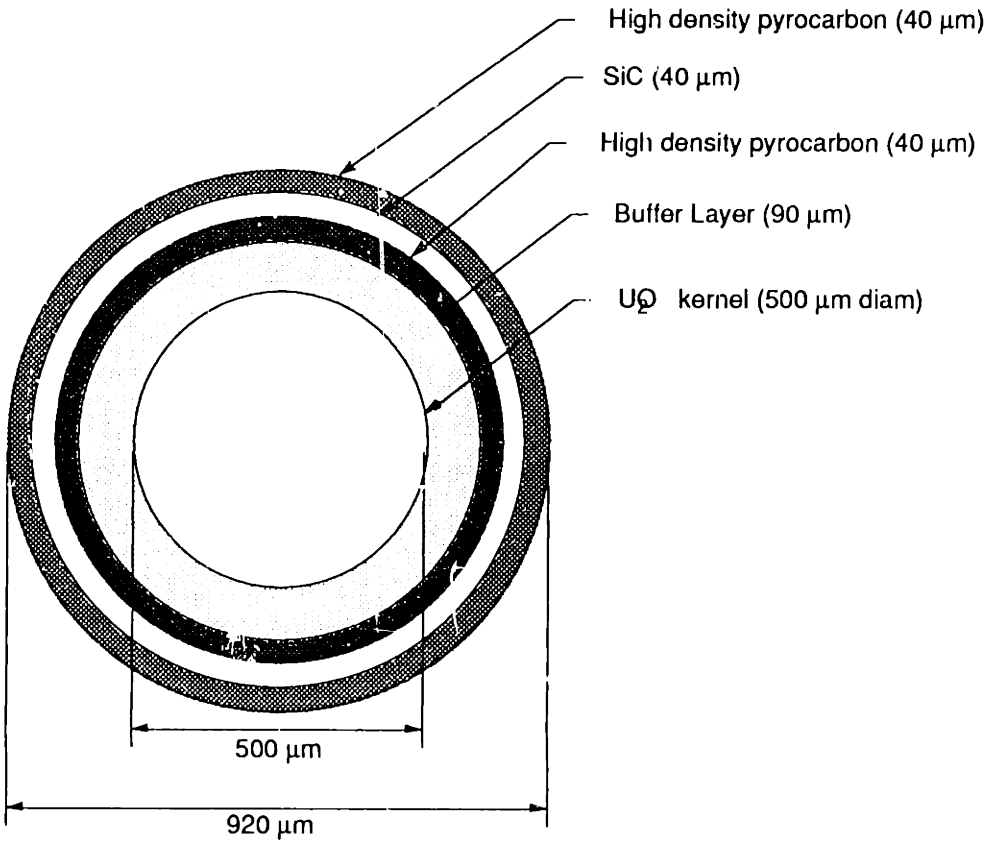

Figure 1.1
Coated fuel particle

These particles are mixed with a carbonaceous binder and formed into fuel elements. Two different designs have been produced. In Germany, the particles are mixed with the binder and encased in a 6 cm diameter spherical fuel element known as a *pebble*. There are about 16,000 particles per pebble. The pebbles are placed into a cylindrical graphite reflector to form the core. Helium flows through the pebble bed to cool the fuel elements.

[1] with the possible exception of silver

This arrangement allows on-line refueling by the regular removal of spent fuel pebbles from the bottom of the core and their replacement with new pebbles at the top of the core. Both once-through and multiple-pass fuel management schemes have been proposed.

The fuel and binder mixture may also be formed into fuel cylinders known as *compacts*. These compacts are inserted in holes in large hexagonal moderator blocks. The helium coolant flows through other holes in the moderator blocks, cooling the fuel and moderator. Two reactors of this type have been built in the United States. A third, modular reactor of this type has been proposed for combined electricity and tritium production for the U.S. DOE.

Extensive tests on particle fuel in both the U.S. and the FRG have demonstrated the ability of this fuel to retain fission products at temperatures up to 1600°C for 500 hr.[R1] For most designs, the maximum fuel temperatures during normal operation are less than 1000°C. The large difference between the fuel operating and failure temperatures, coupled with the thermal mass of the graphite moderator, makes HTGR's tolerant of minor power/cooling mismatches, and means that fuel failure temperatures are not reached for many hours after a loss-of coolant accident in large HTGR's. Both the Fort St. Vrain reactor in the U.S. and the Thorium Hochtemperature Reaktor (THTR) in Germany exploited this safety feature.

Perhaps more importantly, the high fuel failure temperature allows the design of a small HTGR, in which the decay heat is removed by thermal radiation and conduction from the sides of a reactor vessel. Reactors designed using these principles will not experience significant fuel failure during accidents. Because they need to transport the entire decay heat across the core radius by conduction and thermal radiation alone, these reactors are limited in maximum power, to perhaps 200 MWth for a pebble bed design and 450 MWth for a reactor with a prismatic core. These reactors have come to be known as *modular* gas-cooled reactors (MGR's). The "modular" refers to the concept of building up an power generating facility with a number of such reactor modules, for a total plant output in the 300-600 MWe range. The power output of these modules could be utilized in a number of ways--to power a conventional steam Rankine cycle, for process heat (desalination, coal gasification), or directly in a closed helium Brayton cycle. Two designs for modular gas reactors exist today, one developed by a consortium of German companies, and the other by the US Department of Energy and General Atomics.

1.3. German design

The German design, currently being marketed by Hochtemperaturreaktor GmbH (HTR GmbH) is loosely based on the AVR research reactor in Jülich, Germany. The AVR

reactor was built at the German state and Federal research laboratory Kernforschunganlage (KFA) Jülich in 1961. It operated very well until completion of the project in 1989. During this time it demonstrated the ability of HTR's to operate at a 950°C coolant outlet temperature. [E1] The AVR reactor is a 45 MWth, 15 MWe research reactor with a pebble bed core and a steam generator on top of the core in a single vessel. The HTR Modul design, as illustrated in Figure 1.2 is a side-by-side arrangement with the steam generator in an adjacent vessel. Cool helium from the steam generator is heated as it flows down through the reactor core. The hot helium flows though the inner coaxial pipe of the cross-duct, up through the steam generator and circulator, sweeps the outside of the steam generator, flows back through the cross-duct and sweeps the outside of the steel reactor vessel before flowing through the core. This flow path is designed to ensure that all pressure boundaries are near the lowest helium temperature. The helium temperature at core exit is 700°C. The Modul produces 200 MW of thermal power.

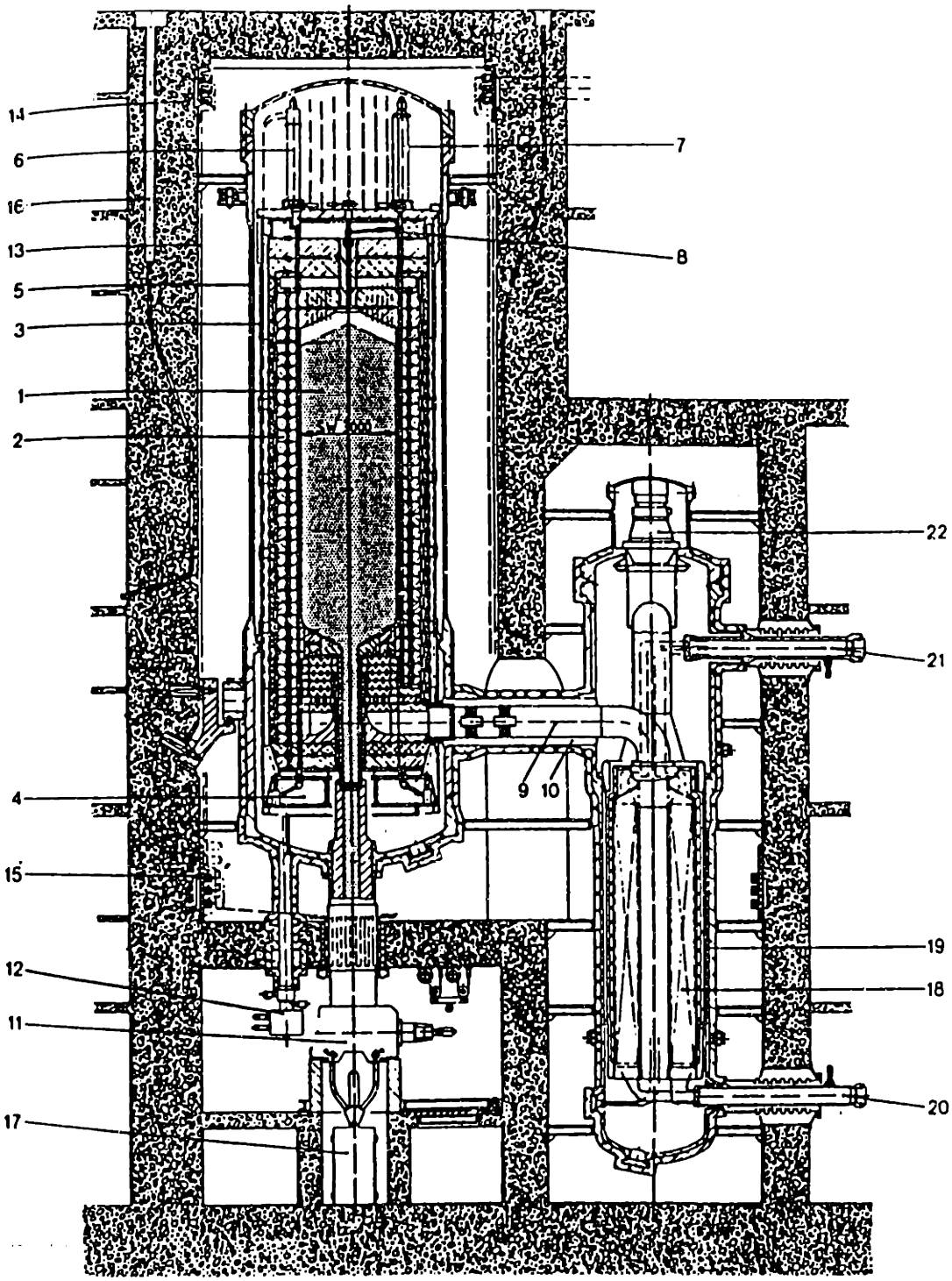

Figure 1.2
The HTR Modul

1.4. U.S. Design

The U.S. design utilizes primismatic fuel. The active core is an annular region, with a central unfueled moderator. Control rods penetrate the moderator just inside and outside of the fueled zone. The use of an annular core allows a higher power density by moving the power-producing region closer to the reactor vessel. The U.S. design is for a 350 MWth module. There is some interest in increasing the diameter of the vessel to allow for a power increase to 450 MWth. It is likely this will become the reference design if current feasibility studies have their expected results.

A group of slightly modified 350 MWth designs has been proposed for the U.S. DOE New Production Reactor (NPR) program. The NPR program is to develop reactors to replace the DOE's aging tritium production facilities. A consortium of companies including General Atomics has proposed to build MGR's as combined tritium and electricity production units. These reactors would represent the first true MGR's to be built.

1.5. Direct Brayton Cycle designs

Even from the earliest days of development of the gas-cooled reactor, nuclear engineers have been intrigued by the possibilities of utilizing the hot gas from the core in a nuclear-heated Brayton cycle. [D1, T1, H6, B1]. The potential for high temperature operation, with gas outlet temperatures at 800°C or above, makes the Brayton cycle attractive. The development of high quality TRISO coated particles in the 1970's and 1980's made *direct* Brayton cycle gas-cooled reactors practical. A number of designs for large (600 MWe or greater) direct Brayton cycle HTGR's were proposed in the 1970's. In Germany, a prototype conventionally heated helium turbomachine was built and operated for a short time . The combination of the Brayton cyle with large gas-cooled ractors in PCRV's was later abandoned as being too costly, too complex, and too expensive to maintain. Nonetheless, the direct Brayton cycle remains attractive for its potential simplicity, high efficiency and excellent load-following ability.

In the middle 1980's, engineers at the Massachusetts Institute of Technology began to investigate the concept of mating a MGR with a direct Brayton cycle power conversion system. The resulting design, first set forth in detail by Dr James Staudt [S8], is known as the MGR-GT (Modular Gas Reactor - Gas Turbine). In the MGR-GT would utilize the same side-by-side configuration as the MGR steam generating version, but would replace the steam generator with the turbomachinery, a gas-to-gas recuperator and a high-speed immersed motor-generator unit. The MGR-GT looks attractive while the large HTGR Brayton cycle reactors did not because of several differences and technological advances in the years which have elapsed between their design.

The first and most important of these is the reduction in total power of the unit. Connecting the turbomachinery to a 200 MWth reactor results in helium turbomachinery of a power rating where much of aircraft gas turbine technology is applicable. Secondly, the use of very high effectiveness, compact gas-to-gas recuperators yield a high cycle efficiency with a pressure ratio near 2. This reduction in optimum pressure ratio brings about a further reduction in the required number of stages, so the turbomachinery is exceptionally compact and efficient. Finally, advances in high-power solid state electronics allow the generator to operate above the synchronous speed by utilizing solid-state frequency conversion. This increase in rotational speed further reduces the required number of stages in the compressor and turbine, and shrinks the diameter of each of the stages.

All of these features have renewed interest in the direct cycle helium-cooled reactor. Variants of the design exist where the gas-circulation and power turbines are decoupled in a split-shaft arrangement. This configuration would allow the use of synchronous generators and the possibility of having the generator drive shaft penetrating the vessel. This would allow for easier maintainence on the generators and associated equipment. [L1, Y1, Y2] The MGR-GT promises to be a truly modular power plant, with the entire nuclear heat supply and power conversion in a single system, supplied as a unit from one manufacturer.

1.6. Safety of MHTGR's

The MHTGR derives its passive safety from a design which ensures that significant fuel failure will not occur, even during the worst-case credible accident. Thus the safety analysis of this reactor is based on, and proceeds from, an understanding of the physical processes involved in accident situations. This understanding begins with the analysis of heat transfer mechanisms inside the core and in the reactor vessel, which leads to predictions for the fuel temperatures as a function of space and time. These predictions are verified by experiments. [T2]

1.6.1. fuel failure

Predictions of the fission product release from the fuel during accidents are made from the calculated fuel temperatures. These predictions rely on fuel failure models such as those developed by Goodin and Nabielek [G2]. Their models are based on an extensive series of experiments by Dr Schenk at KFA.[S1,S2,S3, N2] His experimental facility includes a furnace where irradiated fuel pebbles may be heated to temperatures as high as 1800°C. Fission gas and volatile fission metal release from the heated sphere are monitored throughout the heating period. The results of this research have been reported in several articles and KFA technical reports[S2]. The primary result of their work has been to verify

the ability of intact fuel particles to retain fission products at temperatures up to 1600°C. Indeed, in their testing of modern, high-quality fuel manufactured for AVR, for particles with less than 10% FIMA, *not a single particle has been observed to fail when heated to 1600°C for up to 500 hours.* [R1] This observed failure fraction must be treated statistically to estimate the true population mean failure probability. Interatom has made this evaluation, and Ragoß, in a presentation at ORNL, gave these values:

Table 1.1
Fuel Failure Probabilities

"Free Uranium"[a]	$6x10^{-5}$ at 95% confidence
Core average incremental particle failure fraction at full design burn-up	$2x10^{-4}$ (10x 95% confidence level)
Incremental particle failure fraction at 1600°C	$5x10^{-4}$ (10x 95% confidence level)

[a]Includes both particle surface contamination and particles with defective coatings

Since the fission product release from *intact* particles during the normal operation may be neglected, the primary source of radioactive contamination in the plant during normal operation is due to defective particles in the fuel, and so-called "free uranium"–uranium present outside the SiC layer. Defective particles may be missing layers, or may have interconnected porosity in the SiC layer. Such defective particles and free uranium release fission products during normal operation. The primary fission products released are the gaseous fission products krypton and xenon, and the volatile fission metals such as iodine, cesium and strontium. A number of researchers have studied the release of these fission products during normal operation and their migration around the primary circuit. A summary of this work will be presented in the following chapter.

1.6.2. depressurization accident source term

The goal for the MHTGR program in the United States is to go far beyond the licensing requirements set by 10 CFR 100 and to develop a reactor system which would not require public evacuation or sheltering even during the worst-case credible accident. Some of these goals are illustrated in the following charts. Reactor designers are seeking to limit exposures to the public below the Environmental Protection Agency's (EPA) Protective Action Guidelines for Monitoring. As can be noted from Table 1.2 , this would require releases to be limited in some cases to less than 5% of the 10 CFR 100 limits[15]. In the words of one salesman: "During the worst-case credible accident, we want people to be able to sit at the fence and watch us cope." It is also intended that these goals be met *at the exclusion area boundary* without a pressure-retaining containment building. These goals may be translated into limits on fuel performance as follows.

Table 1.2
Limits on radionuclide releases during accidents

Criteria	Allowed Circulating Activity Ci (Kr^{88})
Normal Operating EAB Dose	14,000
Building Access	1,600
DBDA EAB Doses:	
10CFR100-CP Limits	20,000
PAG/E	5,000
PAG/M	1,000

Abbreviations: EAB-Exclusion Area Boundary, DBDA-Design Basis Depressurization Accident

By using models of fission product transport in the atmosphere and water outside the plant, the regulatory limits for exposure to the public may be translated into an equivalent source term. This modelling is very complex, and depends on the local weather patterns and population density around the plant. Nonetheless, conservative predictions may be made for some "standard" site. In GA document [F1] this "standard MHTGR site" is defined as having characteristics less favorable than 90% of US reactor sites. Once the maximum allowable release from the plant is calculated for each isotope of interest, the equivalent standard for fission product relase from the core may be determined.

To do this requires some knowledge of the distribution of the fission products in the reactor primary circuit and the mechanisms for their release. While this is a very complex issue, and indeed forms the subject of a good part of this thesis, some generalizations may be made in order to understand the controlling mechanisms. The two types of fission products released form the fuel during normal operation have very different behaviors in the primary circuit. The noble gases, being unreactive, circulate with the helium coolant. They are difficult to filter and may build up to concentrations of tens of Curies[E1]. During a depressurization accident, they would be released along with the helium from the primary circuit. It is expected that the fractional release of the noble gases circulating with the coolant will approach 100%.

The volatile fission products behave very differently. After escaping from the kernel, they may be held up in the matrix graphite, adsorbed on the surface of dust particles, be deposited on the reactor metallic components such as the steam generator or cross-duct, or may circulate as gaseous species. During a depressurization accident, all of the circulating activity and some fraction of the dust-borne and deposited activity may be released into the atomosphere.

The relative concentrations and biotoxicity of the noble gases and the volatile fission metals are such that the release of more than 5-10% of the deposited activity may dominate the radiation hazard to the public. This fact highlights the importance of an accurate

prediction of the fractional release of fission metals from the primary circuit during accidents. It is this potential for the deposited activity to dominate the risk from a depressurization accident that motivates this thesis research.

Once the limits on deposited and circulating activity are set, these limits may be translated into standards for fission product release from the fuel during normal and accident conditions. The limits on accident releases may be met by proper design of the fuel particle so as to provide ample margin against failure of standard particles during accidents, and proper control of the fraction of substandard particles. The limits on release from the fuel during normal operation are met by limiting the fraction of defective particles present in the core. Due to the very large number of particles in an HTGR core ($> 10^9$ particles for THTR), the total elimination of defective particles is a practical impossibility. Good quality control and quality assurance programs have been able to limit the fraction of defective particles to $<3x10^{-5}$ and the fraction of free uranium to $<3x10^{-5}$ in production coating batches. [N3] Assuring quality of this level is a challenge in production runs of the size required ($\sim 10^{10}$ particles/core). Already in Germany approximately 50% of the fuel cost may be attributed to the procedures required to assure adequate quality. While this cost may fall as better coating and sorting techniques are developed, it illustrates the high cost of incremental gains in fuel quality.

When the analysis of the accident source term is complete and the required fuel quality determined, it remains unclear whether the goal of meeting the EPA's protective action guides for monitoring can be met with currently achievable fuel quality. Dr. J.L. Maneke [M3] identified one of the key sources of uncertainty as the fraction of cesium, iodine, and strontium which would be released from the plant during a rapid depressurization accident. Better understanding of the mechanisms by which these isotopes are transported around the primary circuit and by which they might be released during an accident could lead to a more accurate prediction of the source term. Since the deposited activity is also a primary source of occupational radiation exposure, the accurate prediction of deposition profiles throughout the primary circuit might also lead to a reduction in radiation exposure to the plant staff. For both these reasons, accident and occupational radiation hazards, this thesis will address the transport of fission metals in a MHTGR, with primary emphasis on developing the experimental techniques and facilities to investigate deposition and reentrainment of iodine and cesium under a limited set of prototypical conditions.

Chapter 2

FISSION PRODUCT TRANSPORT IN HTGR'S

2.1 Fission Product Transport in HTGR's

Unlike water-cooled reactors, where much of the safety analysis centers on determining the probability that safety systems will operate when needed, the safety analysis of gas-cooled reactors focuses primarily on the transport of fission products in the fuel and coolant. Particularly in the MGR, where the design prevents large-scale fuel failure during accidents, and no high-pressure containment is provided, the prediction of fission product release from the fuel and transport around the primary system become the most important factors in determining the risk to the public. The problem of predicting the transport can be broken into two major sections–the first dealing with the behavior of fuel particles, and the second dealing with the transport of fission products around the primary loop once released from the fuel itself. On the fuel side, the major problems are to predict the failure rates and mechanisms for particles, to understand the solid state transport of fission products inside the kernel and matrix graphite, and to predict the rate of fission product release into the coolant.

On the coolant side, the major issues are to predict the rate of fission product transport around the system, the rate of deposition on reactor internals, dust, and power conversion equipment, and the fraction of the activity which can be desorbed or entrained during accidents. In this chapter, only the gas-phase transport will be considered; for a good discussion of the state of the art in fuel failure models see reference [N1].

2.2 Theory

2.2.1 Deposition

Once released from the fuel, fission products may either circulate with the coolant, be removed from the primary by the purification system, deposit on particulates, or be adsorbed on reactor surfaces. The noble gases circulate along with the helium and eventually are removed by the gas cleanup system. The volatile fission products, most notably cesium and iodine, deposit fairly rapidly on circulating dust and on reactor metallic

components. Deposition on the reactor walls has the beneficial effect of removing these fission products from the circulating activity (and hence reducing the expected release fraction), but also represents the primary source of occupational exposure.

The first stage in the deposition process is the transport of depositing species to the surface. For typical flow rates in MGR's, the flow is fully turbulent, so this transport rate is governed by the turbulent diffusivity. By using the analogy between heat and mass transfer, the rate of species transport to the near wall region can be calculated as the product of a mass transfer coefficient and a driving force for mass transfer. In the mass transfer case, the Nusselt and Prandtl numbers are replaced by their mass transfer counterparts: the Sherwood (Sh) number $gD/\rho\mathcal{D}$, and the Schmidt (Sc) number, $\nu/\mathcal{D}$, where g is the mass transfer coefficient kg/m^{2}s], D is the diameter of the flow passage, and $\mathcal{D}$ is the diffusion coefficient. One correlation used in General Atomics MULTI*PADLOC code is [H1]

$$Sh = 0.023\ Re^{.83}\ Sc^{.44} \qquad (2.1)$$

Inserting typical values for the flow parameters in a MGR, as shown in the following table, into equation 2.1 gives values for the mass transfer coefficient in the range of 1-2 kg/m^{2}s. Experiments in the LAMINAR loop were conducted at mass transfer coefficients of 1.2-1.8 kg/m^{2}s.

Table 2.1

Parameters for the evaluation of mass transfer coefficients

T	623 K	
P	60 bar	
v	10 m/s	
$\mathcal{D}$	2.59×10^{-5} m^2/s	diffusion coefficient of Cs in He [H1]
ρ	4.63 kg/m^3	density of helium
D	0.0243 m	diameter of flow passage
ν	7.2×10^{-6} m^2/s	kinematic viscosity of helium
Re	34000	
Sc	0.027	
Sh	27.3	
g	1.35 kg/m^{2}s	mass transfer coefficient

Once transported to the near-wall region, the fission products proceed toward the wall driven by diffusion across the near-stagnant layer immediately adjacent to the wall. In the lower temperature regions of the reactor, particularly in the steam generators, equilibrium between the gas and the surface is never reached, and the vapor pressure at the surface can be neglected. Under these conditions, the deposition rate is controlled by the mass transfer in the bulk flow.

Another important parameter is the *sticking probability*, the probability that a gas atom hitting the wall is adsorbed. The sticking probability approaches one for sufficiently low temperatures. In measurements at ORNL, the sticking probability for iodine on steel was estimated to be 1 at room temperature, falling to 1×10^{-3} at 400°C and 1×10^{-4} at 700°C.[O1] The sticking probability for cesium atoms on low alloy steel is near one for temperatures below ~600°C.[I1]

The single most important unknown in deposition models is the desorption coefficient. Unfortunately, very little data is available on the desorption coefficients at the very low surface concentrations of interest. In a 1984 GA study evaluating the ability of various models to predict measured plateout, differences of up to three orders of magnitude were found in predictions of plate-out using different desorption isotherms.[H3] This discrepancy was attributed to 1) the property data being generated at relatively high fission product partial pressures, then extrapolated by many orders of magnitude 2) the sorption isotherms were generated on materials other than those used in the experiments and 3) diffusion into the bulk material, considered important by German researchers, was not modelled.[I1]

The difficulty in predicting plateout distributions is not confined to this one report. As with many surface phenomena, plateout exhibits a strong dependency on surface finish and specimen preparation. For example, researchers have noted a significant difference in oxidation rates of Incoloy 800H and 316L stainless steel between electropolished and

mechanically polished specimens. [C1] Minor contaminants in the helium stream have profound effects on the structure and stability of surface oxide layers. All this coupled with the lack of instrumentation for measuring fission product partial pressures in the 10^{-12} atm range makes accurate measurements of sorption coefficients a tremendous experimental challenge.

Once deposited on the walls, the fission products may evaporate back into the gas stream, diffuse into the material, or be incorporated into growing oxide layer. The latter two of these possibilities both remove the fission products from direct contact with the coolant stream, reducing the probability that they will be released during an accident. The in-diffusion has been assigned considerable importance in the German literature as a mechanism for reducing the quantity of fission products available for release. The diffusion can be driven both by concentration gradients and also by thermal diffusion on surfaces with high heat fluxes.

As a final consideration, the effect of surface roughness must be included in the predictions of plate-out activity. Deposition models for use in predicting activity on reactor internals must of necessity use the geometric surface area in their calculations. However, the deposition is sensitive to surface variations on the scale of μm, so the true surface area as measured on this scale must be used. Ratios of true surface area to geometric surface area of 10 to 100 have been reported, although seldom is this parameter measured directly.

A number of codes have been written to predict the plateout distributions in operating reactors and test loops. Among theses are GA's MULTI-PADLOC code, KFA/IRB's PATRAS-S, and JAERI's PLAIN code. Of these, PATRAS includes more of the phenomena thought to control plateout, including transport through primary by both macroscopic bulk flow and microscopic flow perpendicular to surfaces. It considers both reversible and irreversible deposition processes. Reentrainment models include desorption and fission product evaporation, as well as shear stress lift-off. Oxide layer growth and the effect of dust on deposited activity are also modelled[I4]. Reference [I5] discusses PATRAS and the other codes.

2.2.2 Lift-off

While one can discuss the deposition of volatile fission products on walls in the absence of particulates, such is not the case with lift-off. In discussion of lift-off models, it must be kept in mind that the lift-off is inherently an aerosol phenomena, i.e. *it is physically impossible to blow adsorbed atoms off the surface*. This fact serves to separate lift-off from evaporation and desorption phenomena.

Since lift-off is an aerosol phenomenon, the starting point for an understanding of lift-off is an understanding of the aerosols present in gas-cooled reactors (conventionally referred to as "dust"). Composition of the dust in gas-cooled reactors varies with the reactor type and its operating history (water ingress, air leaks, etc). In the AVR reactor, the dust was primarily graphitic, formed by the abrasion of fuel elements and the side reflector graphite, along with metal oxides formed from corroded metal surfaces. FSV dust was largely metallic, probably due to the recurring water ingresses into the core. In the Pegase reactor at Caderache, the dust was largely composed of metallic species, along with some silicaeous dust.

A 1987 study by researchers at the Georgia Institute of Technology examined the mechanisms of dust formation in gas-cooled reactors. [S4] They concluded that the primary source of dust in the MGR would be the formation of unstable or poorly adherent oxide layers on steam generator materials. Previous studies of oxide formation under gas-cooled reactor conditions [C1,B2] indicate that oxide layers on 800H may undergo spallation at low strains. High silicon content was observed to enhance the spallation. They also concluded that the chromium content in 2.25 Cr – 1 Mo alloys is too low to form a uniform Cr_2O_3 scale in the low oxygen reactor environment. The iron oxides which do form on the surface of this material may not be stable. The analysis in the Georgia Tech report probably only applies directly to reactors with prismatic cores, particularly in their conclusion regarding the predominance of oxide dust. For pebble bed cores, graphitic dust is likely to play a larger role in the fission product transport.

Dust is an important contributor to fission product transport in gas-cooled reactors for a number of reasons. The small size of particulates in the reactor belies their enormous surface area: for 0.5 μm diameter graphite particles, the surface area per unit mass is ~2000 m^2/g. This fact, combined with their dispersion throughout the coolant volume, means the fission product deposition rate on particulates can be equal to or exceed the deposition rate onto reactor surfaces. Once deposited onto particles, fission products circulate around the reactor. Larger particles (>5 μm) settle quickly, reducing the gas-borne activity. Particles to small to filter (<1 μm) circulate along with the coolant. It is postulated that these particles provide a mechanism for long-range transport of activity around the circuit. Figure 2.1 from [E1] shows the clear correlation between cesium activity and dust concentration in AVR.

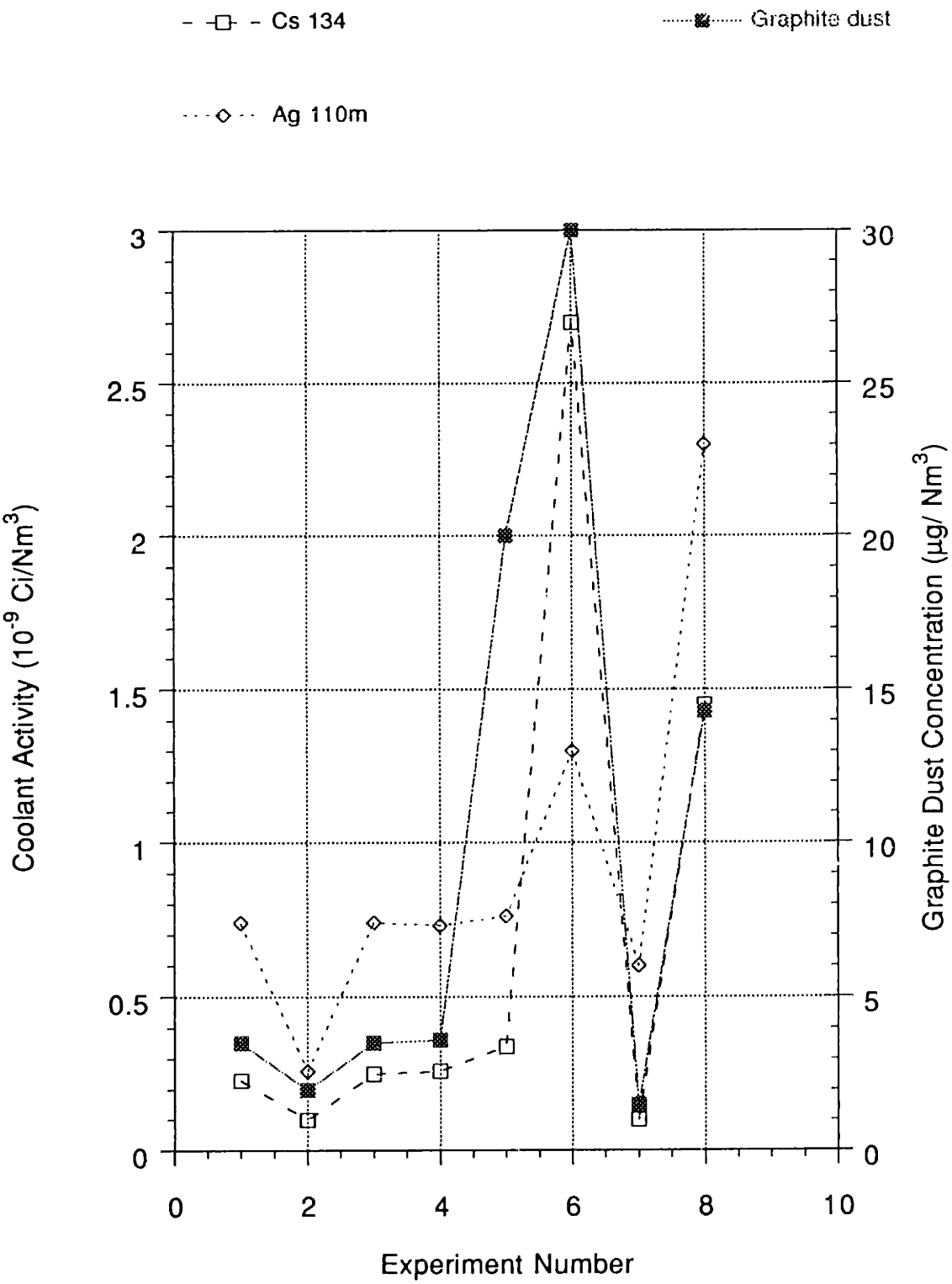

Figure 2.1

Correlation between dust and fission product concentration in AVR

A simple lift-off model developed at GA attempts to correlate the lift-off with the ratio of shear forces during the accident to the shear forces in normal operation.[H7] By using correlations for the wall shear in turbulent flow, the following relationship for the shear ratio as a function of the bulk flow conditions can be derived

$$\sigma = \left(\frac{\rho_A}{\rho_N}\right)^{0.75}\left(\frac{v_A}{v_N}\right)^{1.75}\left(\frac{\mu_A}{\mu_N}\right)^{0.25}$$

where

σ is the shear ratio,

v is the mean flow velocity,

μ is the gas viscosity,

and subscript '*A*' refers to the accident conditions and subscript '*N*' refers to normal operation.

The shear ratio may be adequate for use as a correlating parameter, but it does not address the basic physics of particle re-entrainment. To do this requires an understanding of the structure of the flow in the near-wall regions. Probably the most complete investigation into this structure reported in the literature was the work of Corino and Brodkey. [C7] These researchers investigated the structure of the wall region in turbulent flow using photographic techniques. Their flow visualization method involved seeding the flow with 0.6μm particles of magnesium oxide, so although it was not the goal of the study, significant insight into the behavior of particles in the near-wall region was developed as part of their study.

The description of the flow field developed by these researchers divides the flow into three regions, expressed in terms of the dimensionless distances from the wall. These distances and velocities of interest are

$$u^+ = \frac{u}{u_\tau} \text{ and } y^+ = \frac{y u_\tau}{\nu}$$

where y is the distance from the wall, and u_τ is the friction velocity given by

$$u_\tau = \sqrt{\frac{\tau_w}{\rho}}$$

and

ν is the kinematic viscosity,

τ_w is the wall shear stress, and

ρ is the fluid density.

The first region they identified is the viscous sublayer, extending from ($0 \le y^+ \le 5$). This layer is often inaccurately refered to as the laminar sublayer. While it is true that

mixing does not occur in this layer, the velocity components are by no means steady. Fluctuating velocity components of up to 50% of u_τ have been reported at $y^+ = 1.5$ [L3]. This variation results from the eddies in the generation region deforming the structure of the viscous sublayer, as shown schematically in Figure 2.2. Within the sublayer region, the fluid continually exhibits departures from rectilinear flow. These disturbances are in the form of small masses of fluid moving at some angle to the mean flow. Few of these masses escape the region, although Corino observed some with particularly large deviations escaping outward.

The next region of the flow is the generation region, extending from ($5 \leq y^+ \leq 70$). In this region most of the turbulence is generated. Within this region, the most important interaction was the "intermittent ejection of discrete fluid elements outward from the wall." These *ejections* or *bursts*, as they have been termed by other researchers, have been postulated to be important contributors to the lift-off phenomenon. The ejection process begins with the formation of a locally deaccelerated region near the wall. This region then forms an intense shear layer where its contacts the outer, more rapidly moving flow. The ejection event is initiated by a large-scale disturbance from the main flow, which causes the shear interface to break up and move rapidly outward almost perpendicular to the main flow. Individual ejections involve dimensions on the order of x^+ 20 to 40, and a θ^+ of perhaps half that. Following the ejection, the large-scale disturbance moves through the ejection region, restoring the normal velocity profile. These *sweeps* accelerate the flow in the wall region.

The final region is the core region, extending for ($y^+ > 70$). In this region, eddies created in the generation region grow in size. The turbulence in this region depends more strongly on upstream events than on the characteristics of the local wall region. This is because the turbulence takes time to diffuse through the wall layer, and the mean velocity in the core region is higher.

There are two major classes of lift-off models which have been proposed. The first is a force balance approach, where lift-off is presumed to occur when the lift forces on the particle exceed the adhesive forces. These models consider the dust as particles with some characteristic aerodynamic diameter. The shear ratio model is a member of this class of force balance models. Its primary assumption is that lift-off occurs when the shear forces exceed the adhesive forces and the particle is detached from the surface. There does exist a lift force on the particle due to the velocity gradient in the boundary layer. However, this lift force is likely to be significantly less than the drag force, so the shear ratio model does not account for the transport of the particles outside the boundary layer.

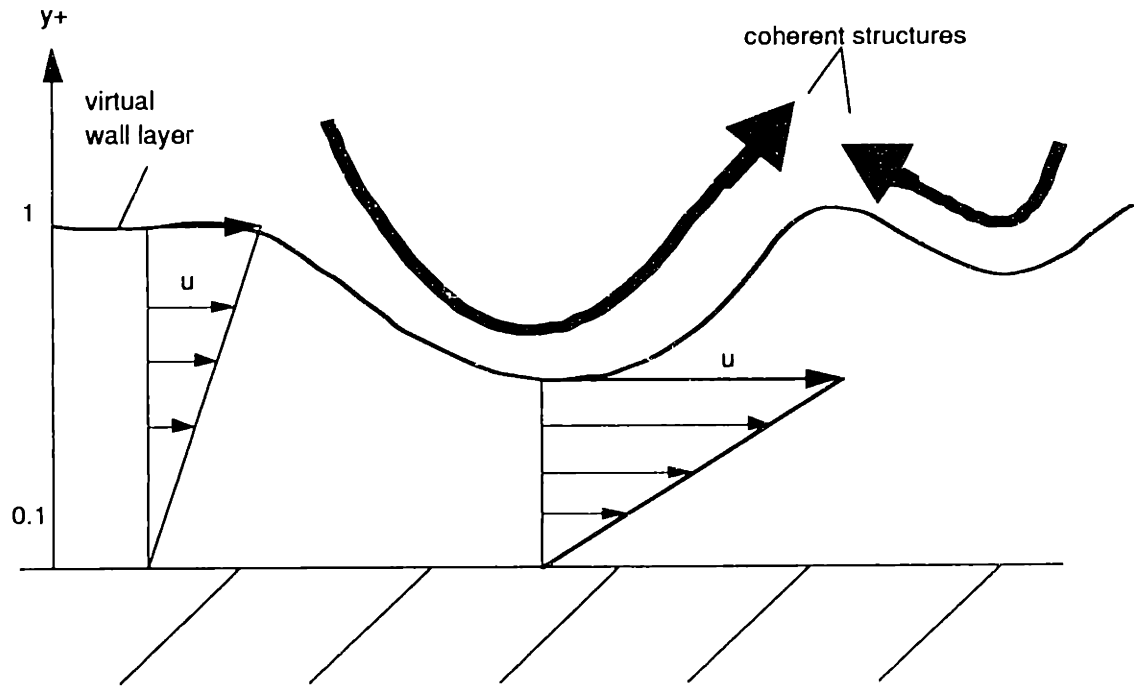

Figure 2.2

Effect of Coherent structures in the wall layers on the sublayer

An alternate version of the force balance approach was reported by Cleaver and Yates, based on Corino and Brodkey's observations [C3]. They propose that the turbulent bursts provide a mechanism for generating locally high values of lift forces on particles, and also increase the ratio of lift to drag forces. Based on the assumption that the adhesive forces (primarily van der Waals forces) are proportional to the particle diameter, they develop the following equation for the relationship between the rms value of the lift force and the adhesive force which will remove particles from the wall

$$\rho\nu^2\left(\frac{du_\tau}{\nu}\right)^3 > \beta d$$

where d is the particle diameter, and βd represents the adhesive force on the particle. This can be simplified to

$$\tau_{wall} d^{4/3} > \beta$$

so the lift-off of particles from the wall should be proportional to the mean wall shear stress. Their paper attempts to develop predictions for the adhesive force constant β and the initial resuspension rates. The results were not definitive, but a good qualitative agreement between the model and experiments was obtained.

Although the force balance models embody a certain degree of physical intuition in their description of the lift-off phenomena, they fail to predict certain experimental observations of lift-off. For a mono-dispersed (single diameter) deposit on smooth

surfaces, these models would predict almost instantaneous lift-off of the entire deposit once the critical value of wall shear or lift was obtained. Observations of lift-off indicate that suspension occurs gradually, and at velocities far lower than those predicted by the force balance equations[S4].

The energy balance approach begins with a qualitatively different description of the removal mechanism. This approach, developed by Reed, Reeks and Hall in 1985, is based on the view that the particles are elastically deformed by the adhesive forces holding them to the wall, as shown schematically in Figure 2.3 [R2]. In static equilibrium, there is a balance between the elastic (repulsive) force, and the adhesive (attractive) force. However, when immersed in a turbulent flow, the varying lift and drag forces on the particle cause it to oscillate around the static equilibrium position. In the absence of slip or rolling, the particles are constrained to move in a potential well produced by the fluctuating adhesive force as the contact area changes with time. According to their model, particles are released when they acquire sufficient energy to escape from this adhesive potential well.

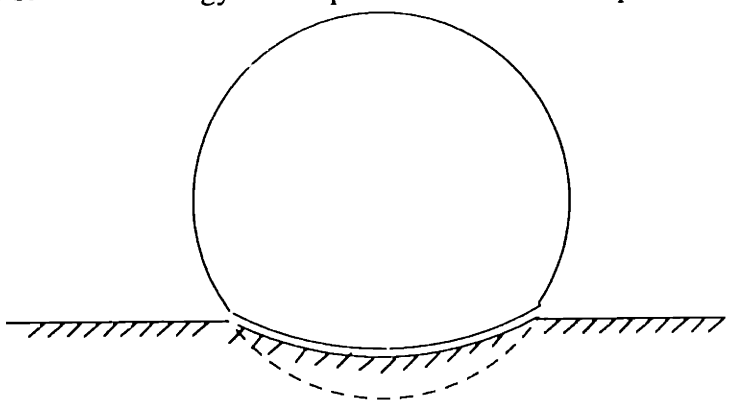

Figure 2.3

The contact of an elastic sphere with an elastic flat surface (exaggerated)

In the Reed model, particles are modelled as a stiff and lightly damped oscillator. They calculate the typical resonant frequency of this oscillator to be ~10^7 Hz for a 10 μm diameter spherical particle on a flat surface. The transfer of turbulent energy to the particle maintains it at some height in the potential well. By determining the force on the particle as a function of height from the surface, they determine a equation for the probability per unit time of particle release from the surface which has the same form as a chemical desorption process, ie.

$$p = A \exp\left(\frac{Q}{2\langle PE\rangle}\right)$$

where

p is the probability of particle release per unit time,

Q is the height of the surface potential well, and

$\langle PE \rangle$ is the average potential energy of the particles within the well.

They found that 10μm radius glass spheres in a turbulent air flow at 30 m/s in a smooth steel pipe had an average lifetime of a particle on the surface on the order of 0.1 sec when the rms lift force was as little as 10% of the adhesive force.[R2] This observation would be at odds with the force balance models which predict resuspension only when the rms lift force is greater than the adhesive force. In Reed and Reek's experimental studies, they divided the resuspension into two periods: an initial time in which a large fraction of the particles was resuspended, and a second phase where the fractional resuspension rate varied almost inversely with time.

Of the two classes of resuspension models, the energy balance approach appears to give the best correlation with experimental data. Fromentin, in his studies of particle resuspension from multi-layer deposits, used the energy balance approach with good results.[F2] His studies, intended to examine the resuspension of particles during a containment failure in a PWR, represents the state of the art in experimental measurements of resuspension rates. While dust deposits in MGR's are likely to have less than a single layer of particles on the surface, Fromentin's results identify two mechanisms other than simple resuspension which can result in the removal of particles from surfaces with multilayer deposits. The first of these is saltation, or, the removal of particles by impact with other particles. The second is denudation, which may be initiated by saltation, and results in the complete removal of particles over a large section of the surface (several square cm). These mechanisms, while not important over most of the reactor circuit, may play a role in moving heavy deposits in regions of low flow. For the various experimental conditions in his studies, Fromentin correlated the resuspension rate with a formula of the form

$$R = a\, t^{-b}$$

where the exponent b was typically 0.8-1.2, values not inconsistent with those found by Reed and Reeks.

2.3 Observation

2.3.1 plateout probes

The best data on fission product transport in actual helium cooled reactors comes from a series of experiments conducted at the AVR reactor just before and after the increase in average hot-gas outlet temperature to 950°C.[E1] After the increase in outlet temperature, the maximum fuel temperature was calculated to be 1040°C. This combination of high

mean temperature, coupled with a fairly significant spatial variation in the power profile, resulted in fuel operating conditions more severe than those envisioned for the MGR-GT and other modern designs.[N2]

Inactive gas impurities, tritium, gaseous fission products, graphite dust and solid fission products were all monitored throughout the programmed increase to higher outlet temperatures. The noble gas activity after the increase was 34 Ci (1.7×10^{-4} Ci/Nm^3) The dust concentration and solid fission product activity in the cold gas were estimated by periodically removing duct filters from the system. The short-lived isotopes showed a clear temperature dependence, with I^{131} increasing from 0.016×10^{-9} Ci/Nm^3 at 770°C to 1.7×10^{-9} Ci/Nm^3 at 950 °C. However, the long-lived isotopes depended on the concentration of graphite dust in the coolant gas more than the hot-gas temperature. The authors concluded that the cesium seemed to be transported on dust in the coolant gas. The concentration of fission products on the graphite was estimated from these experiments to be 6.7×10^{-5} Ci/(g graphite) for ^{134}Cs, 4.8×10^{-5} Ci(g graphite) for ^{137}Cs, and 16.1×10^{-5} Ci/(g graphite) for ^{110m}Ag.

2.3.2 VAMPYR I & II

VAMPYR I and II were essentially out-of pile helium loops utilizing the AVR reactor as a fission product source.[G3, S5] The loop sampled the helium coolant just above the pebble bed and below the steam generator. The sampled gas was led through a pipe, where the temperature varied from 850 to 400°C. These loops were used to measure the plateout of solid fission products from the hot gas of the AVR, and to estimate the fission product concentrations in the hot gas. Table 2.2 gives the measured values for the fission product concentrations

Table 2.2

Fission product concentrations in the AVR hot gas [E1]

	Concentrations in 10^{-9} Ci/Nm^3			
Average hot gas outlet temp	**770°C**	**825°C**	**850°C**	**950°C**
^{110m}Ag	0.9	2.4	3.5	12.9
^{111}Ag	0.09	19	70	1510
^{131}I	3.4	6.5	9.6	29.7
^{134}Cs	0.20	0.21	0.25	2.5
^{137}Cs	0.14	0.09	0.13	1.3

2.4 Experimental studies

2.4.1 GA loop

General Atomics built and operated a bench-top fission deposition and lift-off loop. The GA loop was a small loop contained entirely inside a 6 inch ID autoclave. Measurements were made of iodine cesium, and strontium plateout on $2\frac{1}{4}$ Cr–1 Mo steel. After the deposition phase, the loop section was cut into small pieces and subjected to a "blowdown" test, where high velocity gas was blown through the tube to simulate a rapid depressurization. The fraction of reentrained activity was measured and correlated with the "shear ratio". The important characteristics of this loop are given in Table 2.3 [H7]

Table 2.3

Comparison of Operating Conditions for GA Deposition Loop and 1160 MWe HTGR

Conditions	**Deposition Loop**	**1160 MWe HTGR**
He Pressure (atm)	23.8	49.3 (Peach Bottom = 23.8)
Reynolds No.	12,000	40,000 (steam generator)
He temperature (°C)	90-500	340-780
Surface temperature (°C)	50-500	220-780 (220-425 in Evap-Econ sections)
Surface material	Chromaloy	Chromaloy

The principal results of the GA program were to find a general decrease of the fission product activity on the walls with distance from the source in the isothermal section. A typical result from their study is shown in Figure 2.4. Increased deposition was observed at the 180° bend in the pipe near the top of the experiment. Cesium plateout activity

increased by almost two orders of magnitude in the colder section. Similar results were reported for iodine and cesium. For experiments where dust was introduced into the loop, the results are less clear. The same general trends were observed, but the scatter in the data is very large. Figure 2.5 shows the results from a run in which dust was added to the loop.

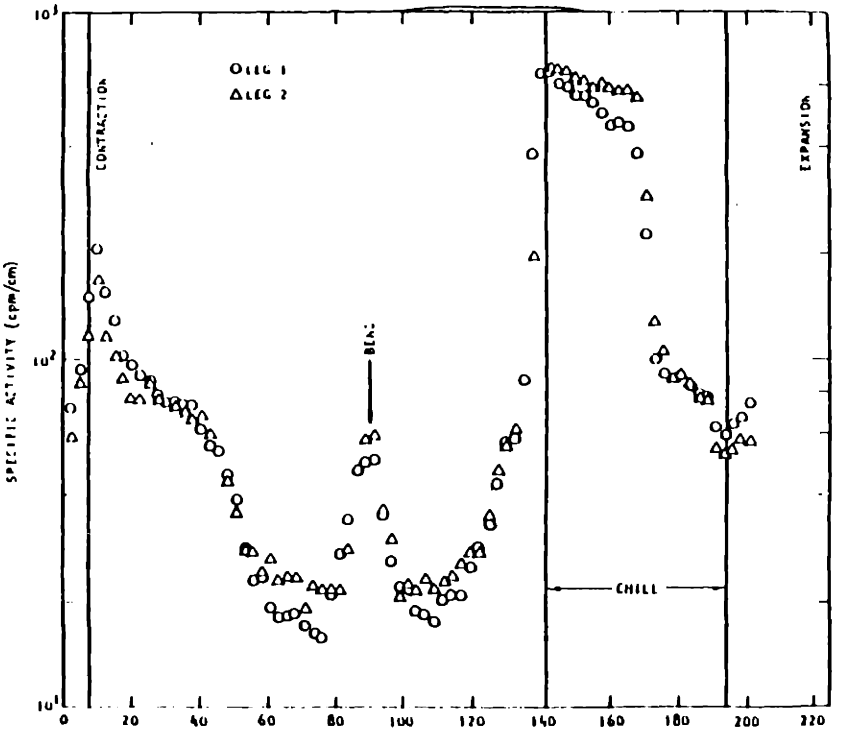

Figure 2.4
Cs Plateout Distribution in the GA Loop

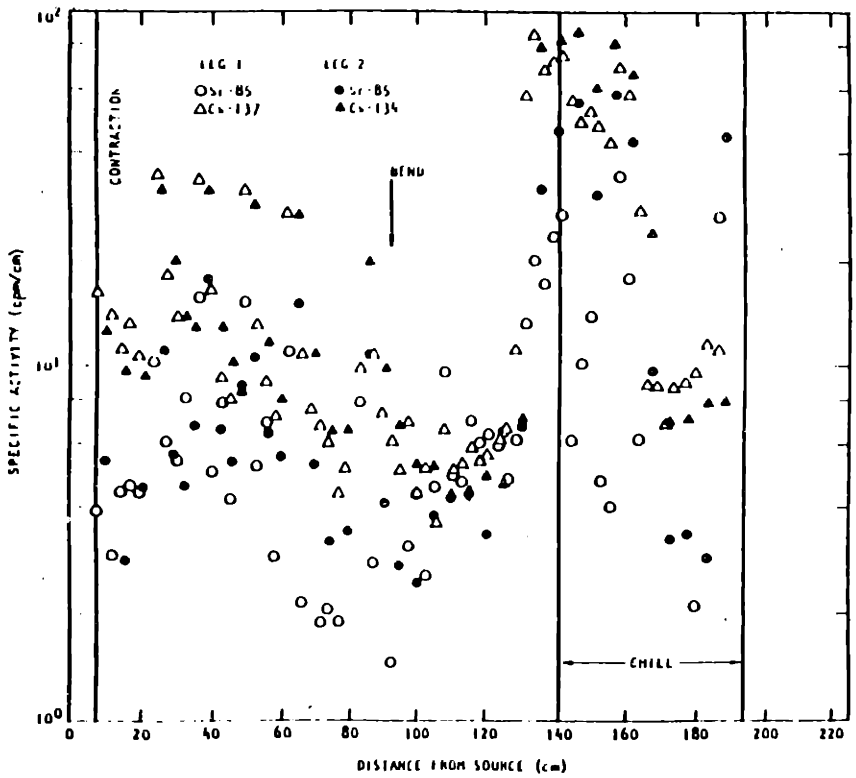

Figure 2.5

Cs Plateout Distribution in the GA Loop (Dust Added)

Lift-off experiments were performed with both air and helium. The results showed considerable scatter, with from <2% to more than 40% of the deposited activity blown off at a shear ratio of 7.5.

2.4.2 Comedie

The COMEDIE loop is an in-pile loop at the SILOE reactor in Grenoble, France. It was constructed in the early 1980's as part of a cooperative program between GA and the French nuclear commission (CEA) to develop HTGR's. The loop was mothballed after initial testing when the French government decided to withdraw from the HTGR development effort. It has been recently revived under US DOE funding to produce licensing data for the MHTGR.

The COMEDIE loop [B3] consists of an in-pile section where the fission products are generated and deposited, and an out of pile sections including the circulator and other supporting equipment. The in-pile section consists of a fueled region which serves both as

a gas heater and a fission product source. The fuel is HTGR particle fuel (BISO in the early tests, TRISO in the current ones), with a controlled addition of "designed-to-fail" particles. The "designed-to-fail" particles are either bare kernels, particles without a buffer layer, or particles with laser-drilled holes in the SiC layer. The fuel is placed in a full-scale model of a fraction of a HTGR prism. Above the fuel is a plateout section consisting of a counterflow heat exchanger. Also included in the plateout section is a fission product filter and a electrical heater to maintain the temperature of the gas.

The out-of-pile section includes the filters, another heat exchanger, an out-pile-test section for monitoring corrosion effects, a helium purification circuit, and a helium circulator. Some important parameters for this loop are shown in Table 2.4

Table 2.4
Characteristics of COMEDIE Loop

Maximum diameter in fueled section	70 mm
helium flow rate	16 to 45 g/s
fuel surface temperature	800 to 1100°C
plate-out section inlet gas temperature	600 to 835°C
out-of-pile test section temperature	600 to 850°C

2.4.3 LAMINAR

The LAMINAR[1] Loop was constructed at KFA, Jülich, Germany, by HRB GmBH. The loop consists of [R3]

- a 43 kW electrical heater
- a hot gas duct (insulated on the inside, water cooled on the outside)
- a sample tube (2.4 m long), with an outer 4-zone electrical heater (9.6 kW)
- gas cooler (water cooled tubular heat exchanger)
- Absolute filter (2 micropore (0.45 μm) filter blocks in series)
- circulator (2 stage, 100 m^3 (STP)/hr membrane compressor, 4 kW electrical)
- helium purification plant (CuO bed, 2 molecular sieve beds in series, 10 m^3 (STP)/hr He flow)
- Cesium source with temperature control, He-supply and outer gamma shielding.

The LAMINAR loop is the most modern of the out-of-pile loops discussed in the literature, and the DABLE project drew heavily upon its design. The loop was constructed

[1]The choice of names seems odd, since the loop operated in the turbulent regime.

primarily to investigate the deposition of cesium on superheater walls and to provide data for Inotakis's deposition models[I1,R3]. For the cesium tests the loop operated with the following typical values

Helium pressure	3 bar
Helium circuit inventory	80 g
Mass flow Rate	18 kg/hr
Reynolds Number	6000-7000
Mass Transfer Coefficient	20-30 cm/s
Cs Partial Pressure	10^{-12} to 10^{-11} bar
Wall temperature	600-900°C
Gas Temperature at the abs. filter	≤50 °C

A number of experiments were performed in the loop at various Cs partial pressures, for times of up to 50 days. Surface activity levels at the end of the experiment ranged from 0.7 to 20 nCi/cm^2. After the end of a deposition period, the sample tube was cut into 15 cm sections and the activity measured. In addition to these measurements, the test-section was monitored continuously with four fixed NaI detectors. After disassembly and counting, the sample sections were leached in demineralized water for 15-50 hours. The activity removed in this test was considered to be the adsorbed fraction, while the remaining activity was assumed to be bound inside the oxide layer or diffused into the bulk metal. After leaching, the specimens were sectioned and examined metallographically to determine the nature of the oxide layers.

The results were analyzed with the phenomenological plateout model of Iniotakis[I2] This model is represented by a mass balance in a microscopic gas phase layer adjacent to the surface with a thickness of the order of the mean free path of the gas atoms. The transport model includes transport from the fluid bulk through the boundary layer, desorption of the adsorbed species from the wall, adsorption to the surface, and absorption within the wall material. In addition, the following assumptions were made: the desorption coefficient does not depend on the adsorptive surface concentration, that the sticking probability is 1, and that the adsorption is non-activated. With these assumptions, the following equations were derived for Incoloy 800 at temperatures between 600 and 800 °C: desorption coefficient

$$\nu = 1\text{x}10^{11} \exp\left(\frac{-234\pm13 \text{ kJ/mole}}{RT}\right)$$

and the penetration coefficient 1-β

$$1-\beta = 1\text{x}10^{-5} \pm \left\{ \begin{array}{c} 1\text{x}10^{-5} \\ 9\text{x}10^{-6} \end{array} \right\}$$

Typical leach fractions measured in these tests were near 40%, indicating that a substantial fraction of the cesium deposited on surfaces under these conditions is bound in the oxide layers or diffuses into the bulk material. This fraction would not be available for release during accidents, unless the oxide layers were prone to spallation.

Although physical models for deposition and lift-off have been developed, they remain of limited usefulness due to the uncertainty in the data on which they are based. The models are semi-empirical at best, and the best fits between data and theory reported in the literature break down rapidly when applied to experiments conducted under only slightly different conditions. Further progress in the field waits for better characterized data on the effects of individual variables on deposition and lift-off. The DABLE loop, outlined in the next chapter, was designed with exactly these issues in mind, and should prove instrumental in generating the data the modellers need to progress.

Chapter 3

AN OVERVIEW OF THE DABLE LOOP DESIGN

3.1. DABLE System Overview

In 1986, students and faculty at MIT began to investigate the possibility of building a facility at MIT to investigate the deposition and lift-off phenomena in gas-cooled reactors. This work lead to the construction of the DABLE (Deposition And Liftoff/Blowdown Experiment) Loop.

3.1.1. History

The DABLE project began in Feburary of 1986 as part of the senior design project class at MIT. Six students were involved in this project. Two of them, Ed Love and the author, would later help the project evolve from a design project to an experimental facility. The class was taught by Professor Lawrence M. Lidsky. One of his students, J.L. Maneke, had identified in her thesis the uncertainty in liftoff as a major source of uncertainty in the source term. Prompted by this finding, Lidsky assigned as the class project the "design of a facility to measure the deposition of fission products on the walls of a helium cooled reactor and their lift-off in the case of depressurization accidents." The class report [E2] was later submitted to ORNL for review and possible funding. During the next year E. Love continued to improve the design and verified some of the key assumptions in the report, particularly in regard to detection efficiencies and the selection of isotopes.[L2] The construction of the loop was first funded in 1987.

3.1.2. Goals

Simple, inexpensive experiment

The goal of the DABLE project from the very beginning was to generate very well characterised data on deposition and lift-off phenomena in high temperature helium-cooled reactors. An auxiliary goal was to demonstrate that this type of fission product transport experiment could be done in a university setting at a significantly lower cost that was previously thought possible. Fission product transport experiments often seem to fall into the categories of either table-top sized models or full-scale, in-core experiments. The

former are often too small to investigate many of the phenomena of interest, and the latter require very large projects, long lead times and a commitment of significant long term funding. The original DABLE proposal called for something quite different than these extremes: a laboratory scale, out-of-core experiment to be built at MIT. DABLE promised to deliver fundamental insight into the fission product transport phenomena for a significantly lower investment than would be required for an in-core experiment. To be able to accomplish this required a combination of design and construction techniques which lead to a significantly simpler design. This design retained the key features which allow in-situ, real time measurement of deposition, while eliminating or simplifying the support equipment to the maximum extent possible. As will be shown later, this simplification of the support equipment leads to a number of benefits which reach far beyond their obvious impacts on the cost of the facility.

The project was conceived to have two distinct stages–an initial design and construction phase, where the equipment and techniques would be developed for circulating hot, high-pressure, high-purity helium under conditions typical of MGR heat exchangers, and a second experimental phase, where this facility would be used to generate data on and insight into the basic mechanisms of gas-phase fission product transport in MGR's. This thesis presents the summary of the first phase of that work, the design and construction of a facility for performing fission product transport experiments in a simulated MGR environment.

Philosophy

The design philosophy set forth in the original class report has been carried forward throughout the design and construction of the loop: DABLE was to seek the simplest possible solution to all design problems, emphasizing the use of in-house capability whenever possible. The loop was designed from the beginning to be modular in nature, reconfigurable and flexible. Whenever trade-offs between establishing prototypical conditions and ease of data interpretation were called for, the decision would be made in favor of simpler data interpretation. The over-reaching goal was to generate very well characterised data and an understanding of the key parameters which influence the deposition and lift-off phenomena.

This philosophy evolved from an analysis of previous experiments, where in an attempt to generate data of direct applicability to design and licensing, experimenters often failed to contribute to the basic understanding of the deposition and liftoff phenomena. These phenomena are so complex, and influenced by such an array of competing effects that prototypical experiments, while yielding important data for licensing, often failed to

provide the information need to predict fission product behavior in other systems. It was decided early in the design process that DABLE would not be able to compete with such large, expensive in-reactor experiments such as Comedie in France, and that no such attempt would be made. Instead, DABLE would attempt to focus on the generation of data which might be used as input to fission product transport codes.

This philosophy was reflected in the DOE fission product transport program in the late 1980's, where the two major programs were the DABLE experiment at MIT and the Comedie program. These investigations were supported by a number of bench-scale experiments at ORNL. The intent of this program was that Comedie would generate data to verify the design methods for deposition and liftoff, while MIT and the ORNL programs would attempt to gain a deeper understanding of the parameters controlling deposition and liftoff.

3.1.3. major systems

The DABLE loop, as many bench or laboratory-scale fission product transport experiments, is conceptually very simple. The facility consists of a ~ 8 m length of 25 mm diameter pipe with a helium circulator, heaters and a fission product source. Radioactive iodine is introduced at one end of the horizontal test section, and deposits on the walls, where it is measured by a set of movable gamma detectors. After achieving a steady state deposition profile, the circulator speed is increased and the change in the deposition profile is monitored. Alternately, the flow could be diverted through a filter train collecting the activity lifted off the walls. While conceptually a simple experiment, the actual implementation is a tremendous experimental challenge, particularly to do the experiment at pressure and temperatures approaching those of a MGR.

Of all the experiments previously discussed, the DABLE loop bears most similiarity to the LAMINAR loop. The loop itself consists of four major systems. These are a circulator, the piping, the heaters and the fission product source. In addition to these major systems, there are a number of auxilliary systems including the helium input and outlet trains, various safety systems, and a large hot cell and filtration system. In addition to the loop itself, there is a complete data acquisition and control system, including measurement and control of pressure, temperature, flow rate, gas purity and gamma activity. The following chapters will detail the design of each of these systems.

The loop is located in the Nuclear Reactor Laboratory building, rm NW13-255. This room, although very small, was chosen beacuse it is possible to almost completely isolate the room's air supply from the rest of the building, a feature which simplified the design of the safety systems for the loop.

The loop piping is in the form of a rectangle, 3.5 meters by 1.2 meters, placed close to the back wall of the room. Figure 3.1 shows a simplified loop elevation, with distances in meters. Shown schematically beneath the upper pipe is the aluminum channel supporting the gamma detector positioning system. Figure 3.2 shows a top view of the room, including the position of the data acquisition and control computer and the electronics rack housing the signal conditioning and control hardware. Figure 3.3 illustrates the layout of the loop inside the hot cell.

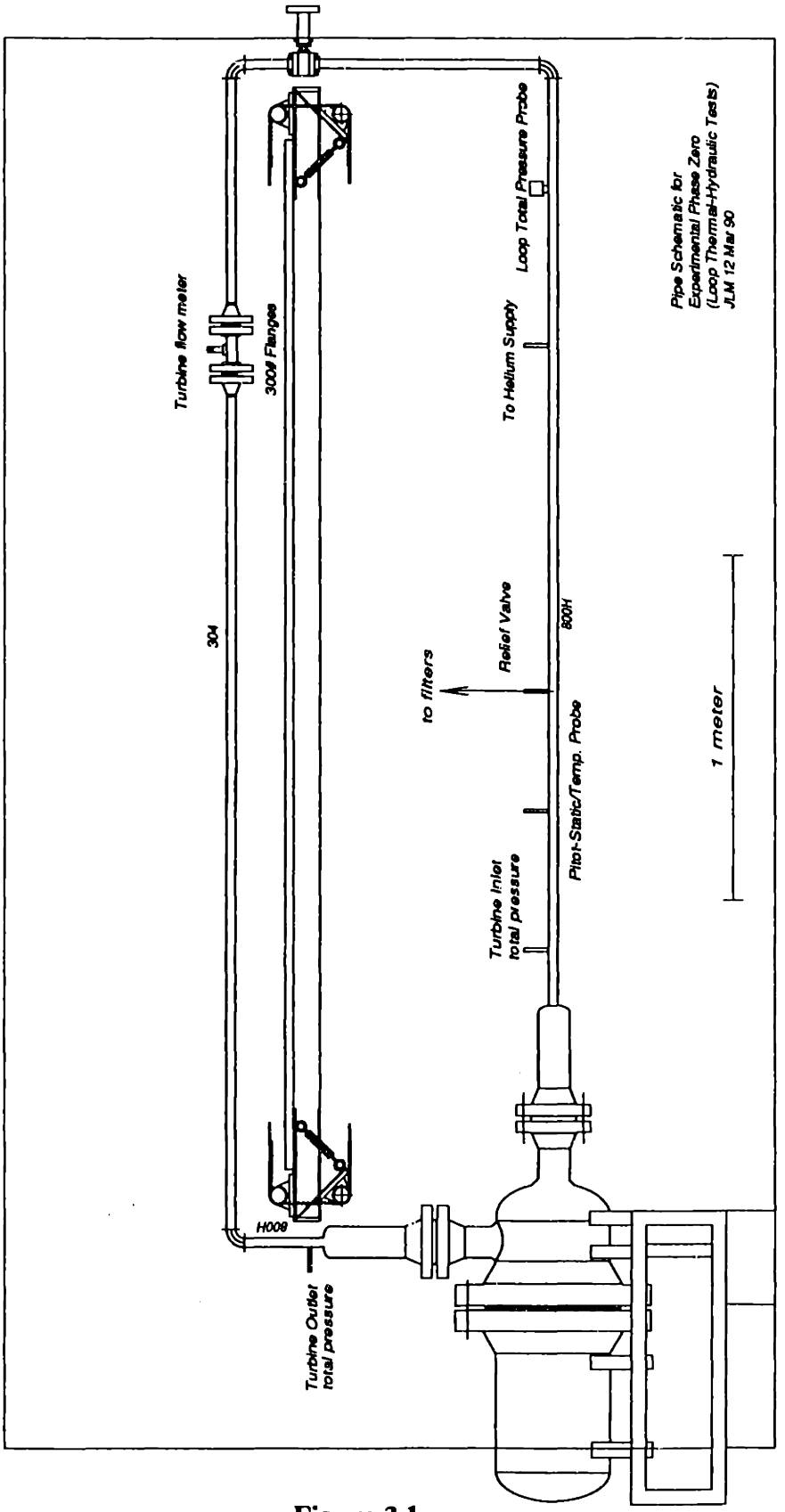

Figure 3.1
DABLE Loop Elevation (Schematic)

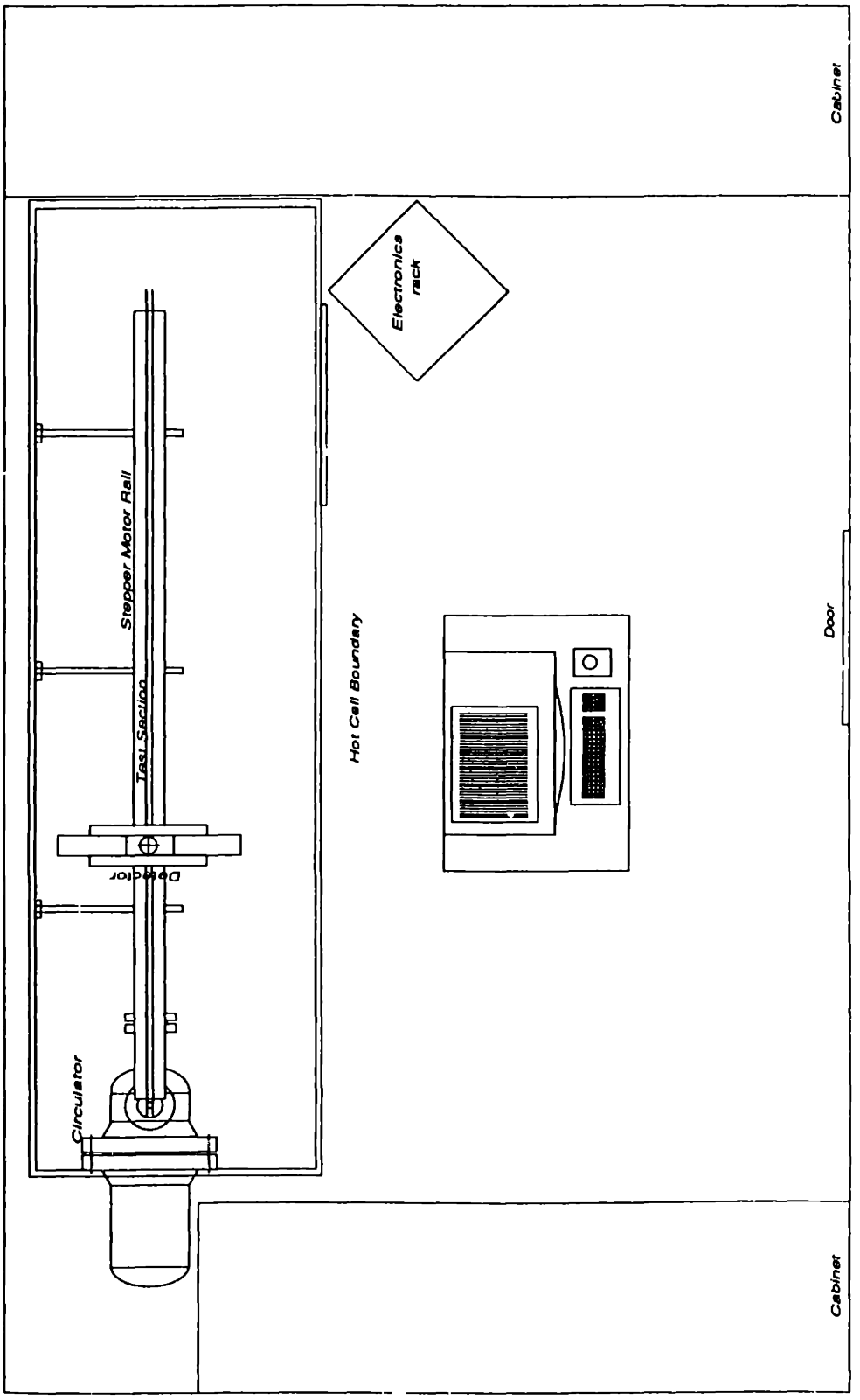

Figure 3.2
Top view of NW13-225

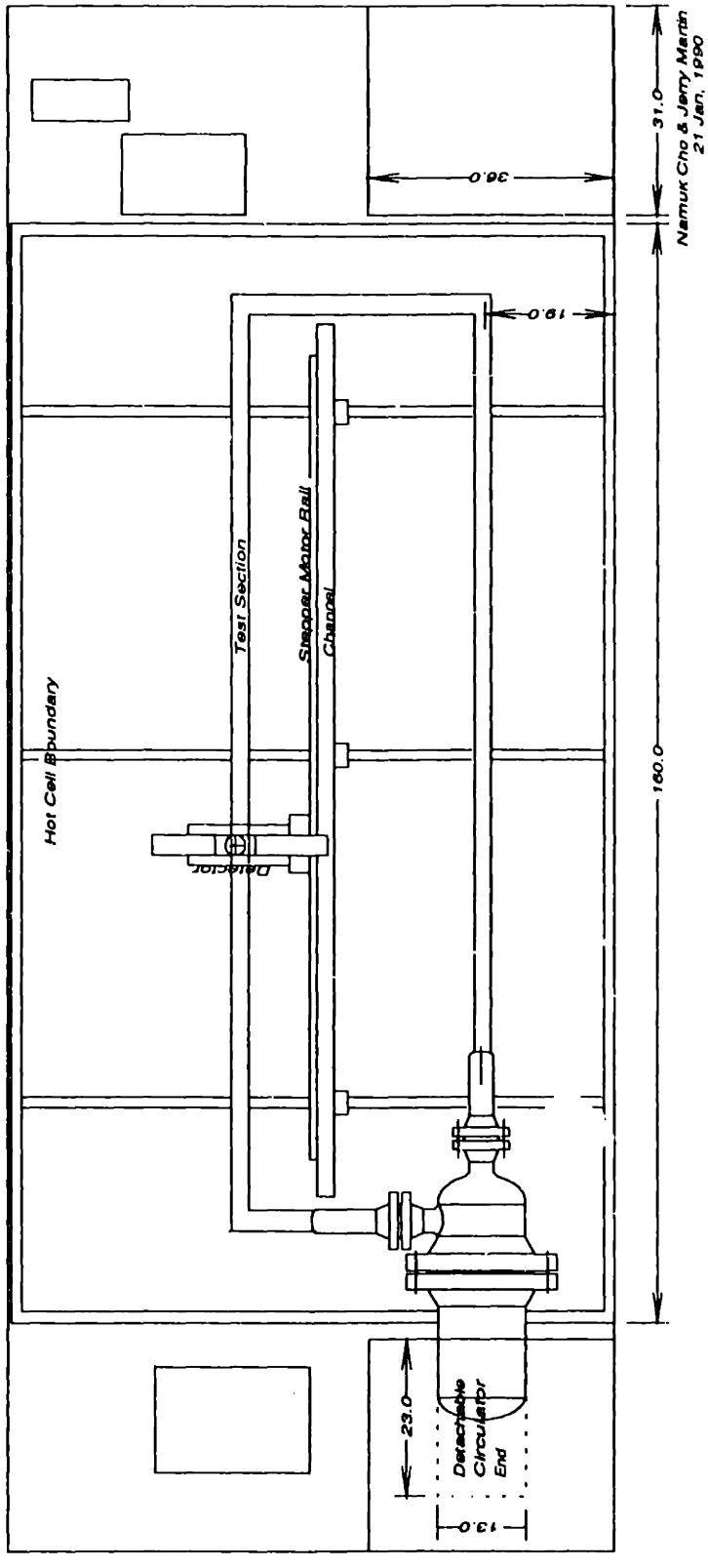

Figure 3.3
DABLE Loop elevation with hot cell

Chapter 4

SELECTION OF THE OPERATING ENVELOPE

One of the first tasks of the original design team was the selection of the loop's operating envelope. This selection would determine the physical size, cost and complexity of much of the following work, and was given much weight in the early stages of the design. The following sections are based on a method of analysis originally proposed by Elson, and further developed by the author.

4.1 Scaling Issues

Any attempt to model the flow through a MHTGR on a laboratory scale necessarily involves differences of several orders of magnitude in scale. The largest flow passages in a modular HTGR could be annuli of up to 1.5 meters in diameter in a coaxial cross-duct, or as small as 1.5 cm diameter in the passages of a steam generator. For the experimental model to be useful, it must be able to model the most important areas in this range of sizes. The model should be able to reproduce the physics of the phenomena involved, if not the actual geometry.

For the plateout phenomena, earlier experiments, theoretical predictions, and observations had all pointed to the importance of the surface temperature in determining the quantity of radioactive deposition. For this reason, and also because of the very large surface area of the steam generators in the steam cycle plant and the recuperators in the gas turbine plant, the steam generators/heat exchangers are the most important areas of the plant to model in a plateout experiment. This is serendipitous, since the flow passages there are among the smallest in the plant.

4.2 Issues of Geometric Similarity

The steam generators in the MGR are helical tube bundles with helium flow on the outside and water flowing on the inside in uphill boiling. This design proved sucessful in the Fort St Vrain HTGR. In the DABLE experiment, the helium flow will be axial flow on the inside of the tubes, instead of cross-flow on the outside of the tubes. The question then

arises whether or not the experimental results will be a valid basis for prediction the transport of fission products in the reactor.

To answer this question requires some model for the transport of gaseous fission products and aerosols around the reactor. While the models deposition and lift-off models of chapter 2 could be used for this purpose, their complexity tends to obscure the basic physics upon which I wish to focus. For the discussion at hand, the following simple model will serve to justify the modelling assumptions.

4.2.1 Importance of Boundary Layer Thickness

If we concentrate on the re-entrainment of previously deposited material, the forces available to remove particles adhering to the wall must arise solely from aerodynamic forces in the boundary layer. The boundary layer has characteristic dimensions which depend on the wall properties, the fluid properties, and the external flow field. It can be demonstrated that the forces on aerosols adhering to the wall should be relatively insensitive to the geometry of the surface. Consider the three-layer model [A2] for the boundary layer given by

$$\begin{aligned} 0 \le y^+ < 5: &\quad u^+ = y^+ \\ 5 \le y^+ < 30: &\quad u^+ = 5y^+ - 3.05 \\ 30 \le y^+: &\quad u^+ = 2.5y^+ + 5.5 \end{aligned}$$

where

$$u^+ = \frac{u}{u_\tau} \text{ and } y^+ = \frac{y u_\tau}{\nu}$$

u is the flow velocity, y is the distance from the wall, and u_τ is the friction velocity given by

$$u_\tau = \sqrt{\frac{\tau_w}{\rho}}$$

and

ν is the kinematic viscosity,

τ_w is the wall shear stress, and

ρ is the fluid density.

The wall shear may be related to the measured pressure drop using correlations such as the Moody chart. Doing this, and making a sample calculation for conditions typical of the DABLE loop, (500°C, 8 MPa, u_m = 10 m/s, $u_m \equiv$ mean flow velocity) one finds the laminar sublayer extends 83 μm from the surface. This dimension is large compared to the expected aerosol size in these reactors [G1], so the particles are likely to be buried deep

within the boundary layers. On this scale, the surface curvature matters little, and differences between internal and external flows are not large. The adverse pressure gradient on the downstream half of the cylinder will have an effect on the boundary layer, but in a fully turbulent flow, the effect of separation will be to reduce the turbulence intensity inside the separated layer. In the test loop, similar effects could be produced by placing barriers in the flow to cause separation.

In summary, the effect of surface curvature on the experiment should be small, since the most important effects occur within the laminar sub-layer, where the flow is essentially one-dimensional. The effect of pressure gradients and boundary layer separation on deposition and lift-off need to be investigated.

4.3 Flow Similiarity

In any model of a fluid system, the basic flow phenomena can be expressed as a function of a limited number of non-dimensional parameters. The choice of these parameters in simple cases is clear, while in the investigation of unknown or poorly understood phenomena, only experience and judgement serve to guide the researcher in the selection of scaling parameters. The investigation of the deposition and lift-off phenomena in the DABLE loop is typical of the later class, where the choice of similarity parameters is not immediately obvious.

4.3.1 Controlling Parameters for Deposition

Again, a detailed discussion of deposition models has been covered in a previous section, and will not be repeated here. However, for the purpose of establishing a defensible basis for the selection of the flow regime for the loop, the following discussion should prove useful. The simplest models of plateout phenomena assume the plateout of radioactive isotopes on the reactor wall is controlled by simple turbulent mass transfer. Invoking the Reynolds analogy between heat and mass transfer, the correlations used are similar to the familiar heat transfer correlations of the form $Nu = C\,Pr^{1/3}Re^{.8}$. In the mass transfer case, the Nusselt and Prandtl numbers are replaced by their mass transfer counterparts: the Sherwood (Sh) number $gD/\rho\mathcal{D}$, and the Schmidt (Sc) number, $\nu/\mathcal{D}$, where g is the mass transfer coefficent [kg/m^{2}s], D is the diameter of the flow passage, and $\mathcal{D}$ is the diffusion coefficient. One correlation used in General Atomics MULTI*PADLOC code is $Sh = 0.023\,Re^{.83}Sc^{.44}$. [H5]

With these parameters in mind, a reasonable scaling for the experimental facility may be derived based on keeping the Reynolds and Schmidt numbers the same in both the model and the actual plant. These dimensionless parameters are a function of temperature, flow velocity, tube diameter and pressure.

4.3.2 Controlling Parameters for Lift-off

Models for lift-off behavior are less well developed. Researchers at GA have attempted to correlate the results of their lift-off studies with the shear ratio (σ). The shear ratio is the ratio of the shear force on the wall during the blowdown phase and the shear force on the wall during normal operation,

$$\sigma = \frac{\tau_{w,\ blowdown}}{\tau_{w,\ normal}} .$$

Other researchers have suggested that the absolute value of τ_{wall} might be the controlling parameter. More complex models have been developed, but most imply a dependence on the flow parameters similar to that which would be derived based on assuming the wall shear is a controlling parameter.

4.4 Selection of Model Parameters

Given the above considerations, we now seek a set of model parameters (flow velocity, pressure, temperature, and passage diameter) which will allow accurate modelling of the physics of liftoff. The selection is further influenced by the need to make an experiment of reasonable size, cost and complexity. Note also that throughout the original design process, the assumption was made that the loop was to contain helium, rather than some other gas. This assumption, taken as obvious in essentially all the previous work in this field, bears some closer scrutiny.

4.4.1 Operating Envelope

To try to control the combinatorial explosion of modelling parameters, a few key assumptions were made early in the development of the operating envelope: the temperature of the gas stream would be kept the same in the model as in the plant, and the gas would be helium. The first constraint is based on the known tendency of fission products to deposit on the coldest walls of the loop. The second is, as mentioned previously, somewhat arbitrary, but certainly a reasonable and obvious constraint. With these two conditions, the viscosity and the quantity $\rho\mathcal{D}$ are equal in the plant and the model, which removes the Schmidt number from the analysis.

The operating envelope for the loop will be expressed in terms of the dimensionless ratios of the quantities in the model (the DABLE loop) and the plant (the MHTGR).

Flow Parameter	**Name**	**Ratio**
velocity	V*	V_m/V_p
diameter	D*	D_m/D_p
Reynolds number	Re*	Re_m/Re_p
wall shear	τ*	τ_m/τ_p
pressure	P*	P_m/P_p

The subscripts m and p refer to the model and the plant, respectively

These dimensionless parameters are used to make the plots which follow. For a given pressure ratio P*, the curve Re* = 1 can be drawn in the D*-V* plane. Similar curves can be drawn for τ* = 1. Figure 4.1 shows this family of curves Re* = 1 for $0.1 < P^* < 1.0$

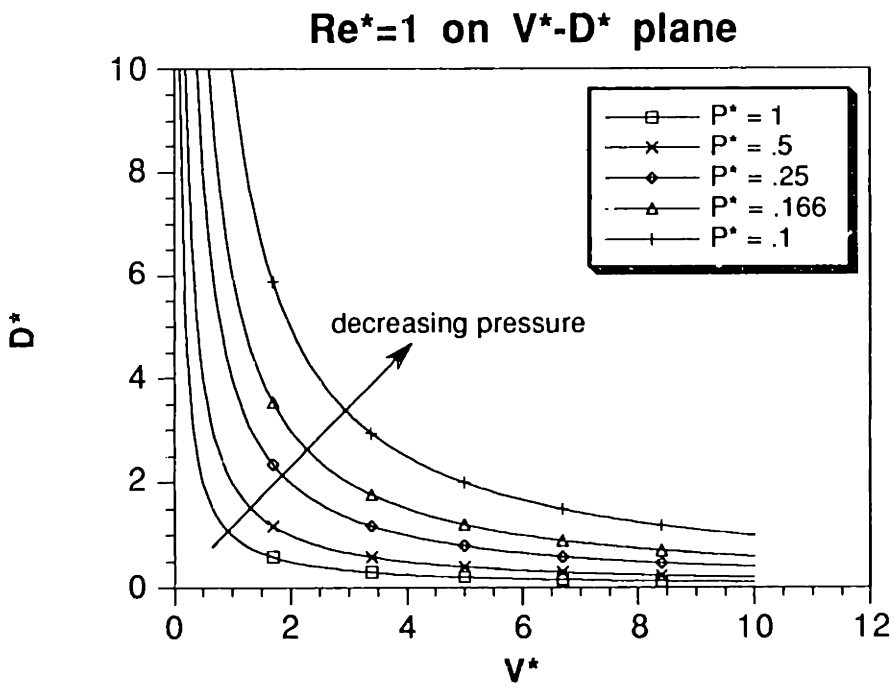

Figure 4.1 Re* = 1 at various pressure ratios P*

Clearly, for all but the smallest flow passages in the plant, the interesting area is the region $D^* \leq 1$, for it is only in this region the loop piping would be smaller than that of the MHTGR. Figure 4.2 shows an enlargement of the previous plot, with the wall shear stress curves added. One important fact emerges immediately from this plot: within the box $\{0<V^*<1, 0<D^*<1\}$ the curves Re*=1 and τ*=1 intersect only for P*>1 and V*=D*=P*=1, the trivial case of a full-scale, full pressure model. At other combinations

of flow rate and pipe size, the criteria of identical Reynolds number and wall shear stress may only be satisfied if the model pressure is greater than the MHTGR pressure.

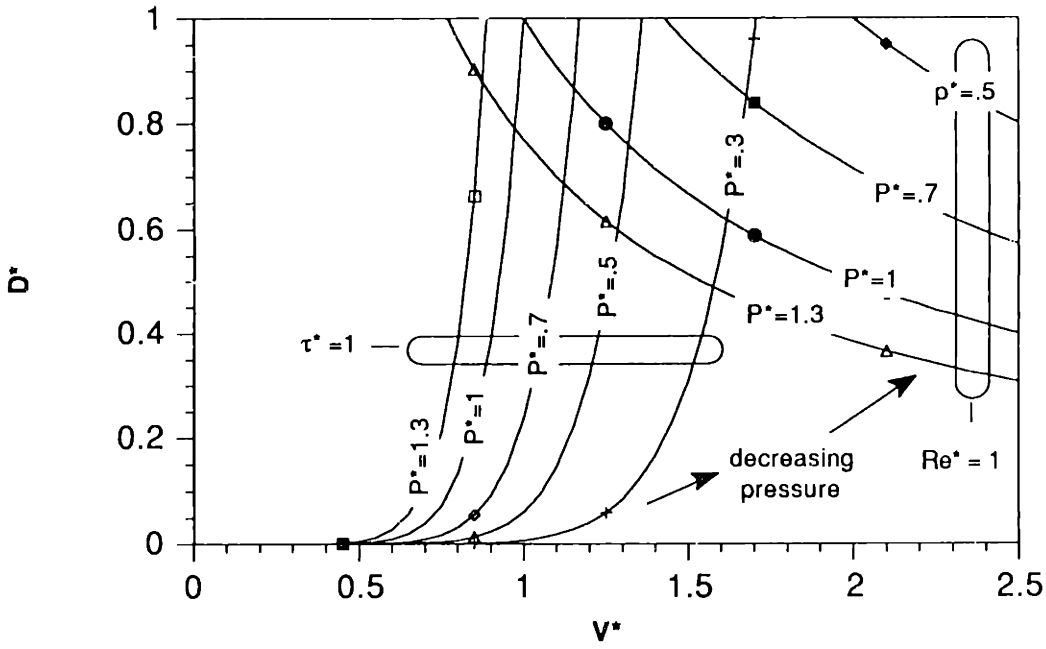

Figure 4.2 The curves Re*=1 and τ*=1 on the V*-D* plane

The decision was now made to relax the Reynolds number criteria, on the basis that extrapolation over a range of Reynolds numbers, *provided the flow remained turbulent,* would be more reliable than extrapolation over a range of less-well-understood wall shear phenomena. This final criterion led to the design area shown in Figure 4.3. Anywhere within this design area, all the following criteria are met:

1) Model pressure is less than 1.3 times the MHTGR operating pressure.
2) Flow is turbulent.
3) Model flow passages are smaller than the MHTGR flow passages
4) Model velocity is less than twice the MHTGR velocity

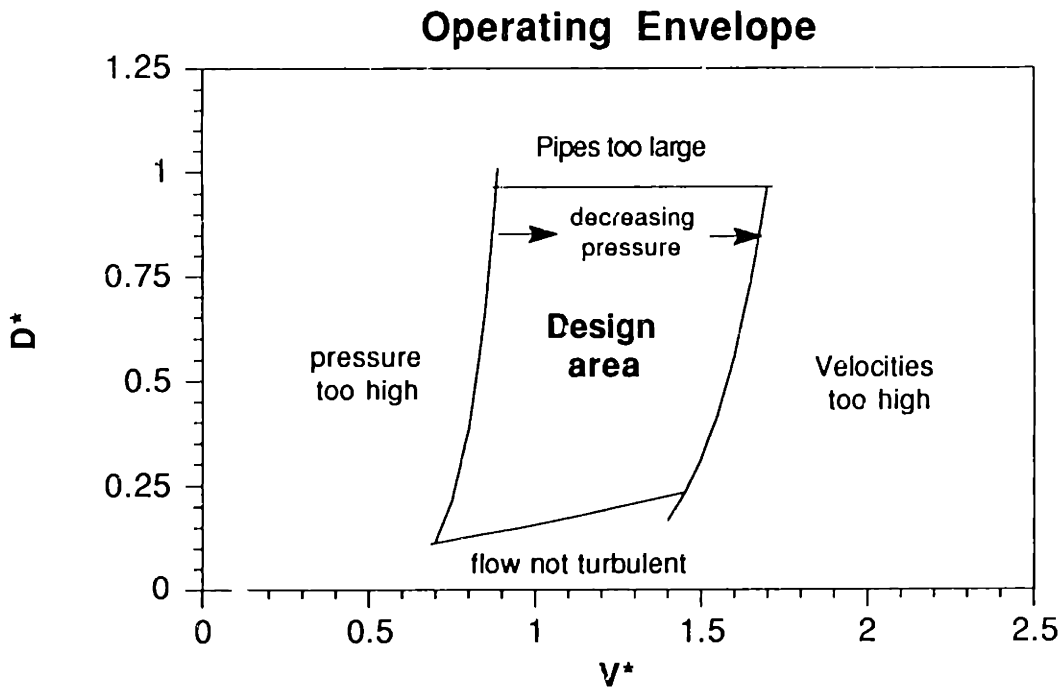

Figure 4.3 Operating Envelope

Tradeoffs within the envelope

Within this envelope several tradeoffs remain to be made. Decreasing the pressure has several advantages, the primary one being that the reduced pressure simplifies the construction of almost all the compents in the loop. A secondary benefit is the reduced pressure could allow the use of thinner-walled piping, reducing the gamma attenuation and the required source activity. With these benefits comes one major cost: the reduction in pressure requires an increased velocity to maintain the same shear stress at the wall.

Which of these trade-offs dominate depends on the exact problem one is trying to model. One goal of the DABLE experiment was to include in the experimental envelope conditions typical of a Brayton cycle MHTGR (MGR-GT). The MGR-GT operates at a higher maximum cycle pressure than the steam cycle version (8 MPa vs 6 MPa). For experiments modelling these high pressures, it is clearly advantageous to operate as far to the right (the low pressure side) of the envelope as possible.

On the other hand, for experiments investigating the lift-off of isotopes under steam-generator conditions, it is advantageous to operate at as high a pressure as possible in order to reduce the velocity required during the deposition phase, and leave the maximum headroom possible for achieving a high velocity and high shear ratio during the lift-off

phase. This statement assumes that the maximum circulator flow rate is rpm limited, not power limited. This assumption is likely to hold in loops with small pressure drops.

Chapter 5

DESIGN OF THE CIRCULATOR

5.1. A Scoping-Level Discussion of the Helium Circulator

In the course of early studies of possible configurations for the loop, the importance of the circulator was identified. In particular, the choice of room-temperature circulators was a major influence on the design of many other loops. With a room-temperature circulator, large heat exchangers are required on both sides of the circulator, one to heat and one to cool the gas. Even with the small cross-section flow paths utilized in laboratory scale experiments, the need to change the temperature by ~ 500°C or more twice during each complete circuit necessitates large heat exchangers and poses an additional pumping power penalty. While this penalty is small on an absolute scale, we will see that it begins to limit the choices for circulator designs.

The presence of the heat exchanger prior to the circulator imposes additional constraints on loop operation. If the test section is too short to plate out all of the radioisotope from the source, then a substantial fraction of the fission products will deposit on the colder walls of the heat exchanger. This means larger quantities of fission products are required, due to their deposition on colder (and largely un-instrumented) heat exchanger walls. Such additional and unwanted deposition complicates the design and operation of the facility.

For all these reasons, the DABLE project sought alternatives to room-temperature circulators. The design process which lead to the selection and development of a new circulator design will now be detailed.

The selection of the experiment's design area has been discussed previously. For the flow passages of greatest interest, conditions within the required envelope may be achieved at practical flow rates in a 2.5 cm (1" nominal) pipe, a readily available size which simplifies the attachment and measurement hardware. Fixing the pipe size yields a range for the Reynolds number and flow velocities from the graphs shown previously (Figures 4.2 and 4.3). Alternatively, if the lift-off is to be correlated with the shear ratio, the range in required velocities is related to the maximum required shear ratio by

$$\frac{V}{V_0} = \sigma^{1/1.75} \tag{5.1}$$

where σ is the maximum design shear ratio, and V_0 is the nominal test section velocity. These considerations lead one to volumetric flow rates $\dot{V}$ of between 0.00465 and 0.0186 m^3/s.

An additional constraint is imposed on the choice of circulator designs by the pressure drop in the system. This was the largest source of uncertainty in the initial design. While the pressure drop due to the flow in the test section is easily calculated, the parasitic pressure drops in the fittings are more difficult to predict. In addition, a final decision regarding the type and configuration of any filters in the system had not been determined when the circulator was designed. For this reason, a decision was made to set the circulator required pressure rise as the calculated pressure drop in the unobstructed system, but to consider larger flow velocities than were actually expected. This was perhaps a poor choice, and leads to a design point flow rate perhaps 10-20% higher than optimum.

The final parameters needed to begin the design process are the operating temperature, pressure and flow rate. There was no clear choice of the operating point for the circulator. On one hand, the circulator was designed to run primarily at a low flow rate, with increased flow only during short bursts. This mode of operation would seem to call for the design point to be set at the nominal deposition volumetric flow rate, temperature and pressure. Unfortunately, this would lead to very low efficiency during the blowdown phase, and a greatly oversized drive system. Therefore, the choice was made to set the design point flow rate as that corresponding to four times the nominal deposition flow rate. Since the shear ratio varies as the square of the velocity ratio, this gave more than adequate shear ratios. In almost all the accident scenarios, the shear ratio does not exceed 1.5 over large areas of the primary circuit. A design shear ratio of 16 for the unrestricted system yields significant room for investigation of lift-off phenomena over a wide range. The system as built was able to achieve flow rates in excess of 20 m/s, yielding shear ratios >4, without optimization of the circulator.

The choice of design point pressure and temperature primarily impact the choice of drive systems, since, to first approximation, the aerodynamic performance of the machine does not depend on system temperature and pressure for an ideal gas. The maximum temperatures expected in the system were in the range from 650 to 750°C, with pressures ranging from 4 to 8 MPa. For the same system pressure, lower temperatures lead to higher pumping power due to the increased helium density. High temperatures and high pressures begin to approach limits for loop components other than the circulator. Considering the

system-level issues, a design point of 500°C and 8 MPa was chosen as one which would strike a balance between thermal and aerodynamic loading on the drive system. Higher temperature operation of the circulator is possible, up to the limits imposed by heat transfer from the loop to the motor and to the creep limit of the impeller, however, some modification might have to be made on the loop piping, seals and heaters. This reasoning led to the following top-level design goals for the circulator.

Table 5.1

Design Goals: Conditions at Design Point	
Temperature	500°C
Pressure	8.0 MPa
volumetric flow rate	0.0186 m^3/s
rpm	20,000
pressure ratio	1.0048
pressure rise	38.5 kPa
polytropic efficiency	60%

The efficiency was estimated from similar designs and used to estimate the drive motor requirements. The volumetric flow rate corresponds to a 40 m/s flow through a 1" schedule 80 pipe. With these major parameters fixed, it was possible to begin a conceptual design of the circulator.

Both centrifugal and axial circulators have been used in gas-cooled nuclear reactors. The British Magnox and AGR CO_2 cooled reactors use centrifugal circulators, as did the Dragon HTGR. The Peach Bottom and Fort St. Vrain HTGR's both used single stage axial flow circulators. Both types of circulators were originally considered for the DABLE loop but the decision was made early in the program to use a centrifugal machine. The low specific speed of the design argues against the use of an axial machine. In addition, the low flow coefficient means the hub-to-tip ratio of the axial flow machine would be very small, leading to very high leakage losses. Finally, the blading for the axial flow machine would likely be much more difficult to machine than the centrifugal impeller. For all of these reasons, a circulator design based on a centrifugal impeller was adopted.

To begin the design, it is helpful to try to gain some feel for the sizes of the machinery and flows involved. The following discussion is based on the analyses presented in D. G. Wilson's text *The Design of High Efficiency Turbomachinery and Gas-Turbines* [W1].

From Euler's equation for energy transfer in turbomachines

$$\frac{\dot{W}}{\dot{m}} = (u_1 C_{\theta 1} - u_2 C_{\theta 2}), \tag{5.2}$$

where

C_θ is the tangential component of the velocity vector,

u is the rotor peripheral speed at the radius of the streamtube,

$\dot{W}$ is the power delivered or absorbed,
$\dot{m}$ is the mass flow rate, and the subscripts refer to inelet and outlet.

For a compressor operating on a gas, where changes in density with height may be neglected, and in the absence of external heat transfer to the machine, the first law applied to the machine at steady state conditions yields

$$\frac{\dot{W}}{\dot{m}} = (h_{01} - h_{02}) . \tag{5.3}$$

where h_0 is the total enthalpy of the fluid. Combining this result with Euler's equation gives a relationship between the rotor and fluid velocities entering and leaving the machine and the enthalpy change across the machine.

$$h_{01} - h_{02} = u_2 C_{\theta 2} - u_1 C_{\theta 1} . \tag{5.4}$$

or

$$\Delta_1^2 h_0 = \Delta_1^2 (u C_\theta) .$$

In the case of a centrifugal impeller with no inlet swirl, C_θ is zero, and this reduces to

$$\Delta_1^2 h_0 = u_2 C_{\theta 2} . \tag{5.5}$$

This simple relation will allow us to make a rough estimate of the size of the machine required.

The pressure ratio and Mach number of the proposed design are low enough that for a rough estimate, we may consider the helium to be incompressible. For a circulator with efficiency η, operating on an incompressible fluid, the following relation holds

$$\Delta h_0 = \frac{\Delta p}{\rho \eta} . \tag{5.6}$$

The pressure rise across the circulator can then be related to the impeller rotational speed by

$$\frac{\Delta p}{\rho} = \eta u_2 C_{\theta 2}$$

For a centrifugal compressor with highly swept-back blades, $C_{\theta 2}$ might be 50% of u_2. Considering a machine with an efficiency in the range of 50% gives

$$\frac{\Delta p}{\rho} = 0.25 u_2^2$$

or

$$u_2 = \sqrt{\frac{4\Delta p}{\rho}} .$$

Now, u is related to the circulator rotational speed by

$$u_2 = \frac{N\pi d_2}{60}. \tag{5.7}$$

where N is the rotational speed of the impeller in rpm. At 500°C and 8.0 MPa, helium has a density of 4.95 kg/m^3. The required pressure rise Δp is 38.5 kPa. This gives the relation

$$u_2 = \sqrt{\frac{4(38000)}{4.95}} = \frac{N\pi d_2}{60} = 175\ m/s.$$

We can select either N or d_2 to continue the analysis. Picking a rotor diameter of 125 mm gives a rotational speed N of approximately 27,000 rpm. Smaller rotors would require higher rpm and larger ones lower. Wilson defines a non-dimensional specific speed as

$$N_{s1} = \frac{2\pi N\sqrt{\dot{V}}}{60(\Delta h_0)^{3/4}}. \tag{5.8}$$

The specific speed for the hypothetical design listed above is approximately 0.32. The flow coefficient

$$\phi = \frac{C_{x1}}{u_2}, \tag{5.9}$$

for this machine would be about 0.15. From figure 5.20 in Wilson's text, the optimum specific speed under these conditions would be close to 0.45. [W1] This shows that a higher efficiency design could be achieved at a higher rpm, or using a slightly larger impeller. Lastly, the power requirements of the design is given by using (5.3) as

$$\dot{W} = \dot{m}\Delta h_0 = 0.092(15{,}350) = 1.4\ kW.$$

From this discussion it should be clear that a centrifugal compressor to meet the stated requirements will have an impeller approximately 125-150 mm diameter, rotating between 20,000 and 30,000 rpm, and absorbing 1.4 kW of power.

5.2. Detailed Aerodyamic Design of the Helium Circulator

With the basic sizes, flow rates, and power requirements of the design established, a detailed design for the helium circulator can be made. Throughout the design process, in keeping with the overall loop design philosophy, emphasis was placed on simplicity and ease of manufacture. A number of tradeoffs were made which had the effect of reducing the efficiency of the machine while increasing its simplicity and ease of assembly. This design freedom was available because of the relatively small size of the machine and the low power requirement. Even at 50% overall aerodynamic efficiency for the whole circulator, the power requirement of 1.4 kW could be easily supplied.

To begin the design process, a number of preliminary parameters had to be selected. These were chosen based informed guesses for the predicted performance, and were later revised based on further calculations. These parameters are shown below.

Table 5.2
Design Goals and Selected Blade Geometry
(Conditions at Design Point)

Temperature	T_{01}	500°C
Pressure	P_{01}	8.0 MPa
volumetric flow rate	$\dot{V}$	0.0186 m^3/s
rpm	N	20,000
polytropic efficiency (total-to-total)	η_{tt}	60%
pressure rise	Δp	to balance pressure losses
hub/shroud ratio at inlet		0.60
inlet flow angle		0.0°
blade angle at outlet	β_2	55°
absolute flow angle leaving rotor	α_2	80°
loop length		8.3 m
minor loss length		65 m

The blade angle at outlet was set to a large value to reduce the magnitude of the absolute outlet velocity. As the blade angle increases, a larger fraction of the pressure rise occurs in the impeller. This reduces the loading on the diffuser. The rotational speed was considered to be the maximum commercially available in a electric motor of conventional construction.[1]

Given these fixed parameters, the design procedure, described in detail below, is as follows: The required pressure rise was determined from an estimate of the flow losses in the loop. The required enthalpy rise was then determined. The shroud diameter at inlet was iterated to find the minimum relative velocity at the shroud. Next, the required impeller diameter was determined from the Eck correlation given in [W1].

$$\frac{C_{\theta 2ac}}{C_{\theta 2ih}} = \left[1 + \frac{2\cos\beta_2}{Z[1 - (d_{s1}/d_2)]} \right]. \tag{5.10}$$

Where Z is the number of blades. Finally, the blade height at exit was determined and the velocity triangles at inlet and outlet set.

5.2.1. Enthalpy rise

The enthalpy rise is given from the perfect gas law and the definition of efficiency as

[1]The validity of this assumption was later shown to be questionable. See section 5.3.3

$$\frac{T_{03}}{T_{01}} = \left(\frac{p_{03}}{P_{01}}\right)^{\left(R/C_p\eta\right)} \tag{5.11}$$

where

$T_{03}/T_{01} = 1.00475^{0.666} = 1.00316$

$\Delta T_{013} = 0.00316 \times 773 = 2\ 63\ °C$

$\Delta h_0 = 12891$ J/kg

5.2.2. *Specific speed*

The non-dimensional specific speed N_{s1} is given by equation 5.13 in [W1]

$$N_{s1} = \frac{2\pi N\sqrt{\dot{V}}}{60(\Delta h_0)^{3/4}}.$$

$N_{S1} = 2\pi(20000)\sqrt{0.0186}\ /\ (60\ (12891)^{3/4} = 0.24$

5.2.3. *Inlet Velocity*

We need to find the shroud diameter which minimizes the relative velocity at the shroud. By minimizing this value, we maximize the relative velocity ratio W_{s1}/W_2. This ratio must be kept above about 0.75 to avoid diffusion-induced separation in the blade passages. W_{s1} is the vector sum of the inlet velocity C_{x1} and the rotor velocity u_{s1} at the shroud. A large shroud diameter minimizes the inlet velocity, but maximizes u_{s1}. Conversely, a small shroud diameter minimizes u_{s1}, but maximizes C_{x1}. There must be a shroud diameter which minimizes the relative inlet velocity. Iterating to find this value yields

$d_{s1} = 34$ mm

$d_{hub} = 17$ mm

$u_{s1} = 35.6$ m/s

$C_{x1} = 27.3$ m/s

$W_{s1} = 44.8$ m/s

5.2.4. *Outlet velocity diagram*

We begin by guessing the outlet diameter as 125 mm. The ratio $C_{\theta 2th}/u_2$ is given by the outlet velocity diagram as

$$\frac{u_2}{C_{\theta 2th}} = 1 + \frac{\tan 55°}{\tan 80°}$$

This would be the ratio if the mean helium flow exited at the blade angle. We now use Eck's correlation to find the ratio of the actual to the theoretical tangential velocities, $C_{\theta 2ac}/C_{\theta 2th}$. This value, combined with the ratio given above, can be used to develop a

revised estimate of the diameter from Euler's equation (eqn 5.1). This revised value is used as a new estimate of the impeller diameter, and the process is repeated to convergence. The results of this procedure are:

d_2 = 129 mm

u_2 = 135 m/s

b_2 = 2.7 mm

C_{r2} = 16.8 m/s

$C_{\theta 2}$ = 96.76

C_2 = 96.8 m/s

α_{rel2} = 67°

yielding the velocity diagram shown in Figure 5.1.

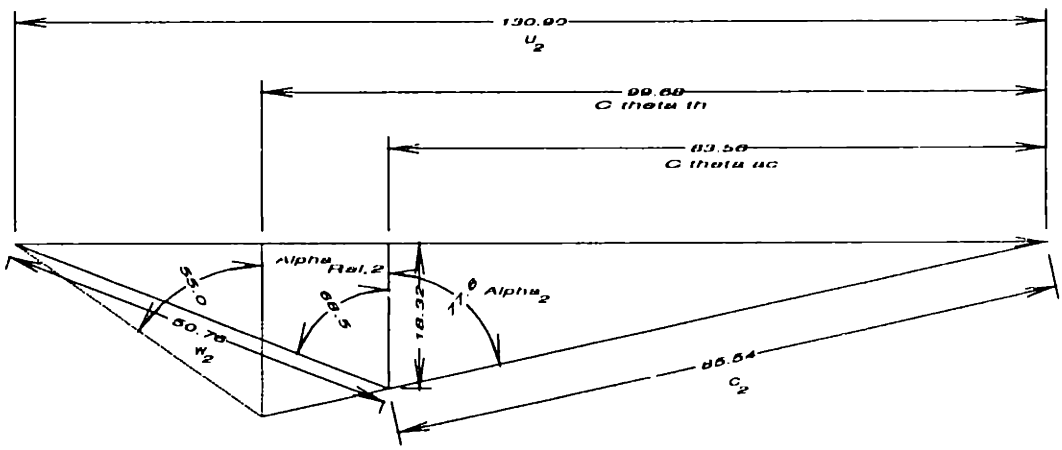

Figure 5.1 Outlet Velocity Diagram

5.2.5. Radial-diffuser stability

The flow from the impeller exits into a vaneless diffuser. A vaneless diffuser was chosen because of its ability to provide reasonable pressure recovery at off-design conditions. For the highly swirling flow given by the large α_2, the flow in the vaneless diffuser is prone to rotating stall. Wilson gives a correlation by Jansen for the maximum radius ratio at which the vaneless diffuser will be stable.[J1] These charts show for the conditions of interest, the maximum radius ratio should be below 1.25. Taking a

conservative approach because of the wide range of operating conditions, the radius ratio was kept below 1.15, for a diffuser outlet diameter of 150 mm.

5.2.6. Scroll

The vaneless diffuser will discharge into a scroll. The scroll aspect ratio was chosen to be approximately square at outlet and of a constant axial height for ease of manufacture. The scroll radius is defined by the equation

$$\frac{r}{r_3} = e^{\lambda\theta}. \tag{5.12}$$

where λ is given by the relation

$$\lambda = \frac{ln(r_4/r_3)}{2\pi}. \tag{5.13}$$

5.3. Mechanical Design of the Circulator

With the aerodynamic design of the circulator established, the mechanical design could be set. The emphasis was on ease of manufacture, since the original intention was to machine a prototype impeller from a solid aluminum disc and use the prototype to make a cast impeller from a high-temperature alloy. This course was later abandoned, but it did serve to define the design goals.

The mechanical design of the impeller was fairly straightforward. The impeller was designed to seat onto a conical shoulder on the shaft. The impeller is held against this shoulder by nut on the threaded shaft end. This provided a simple, self-centering attachment. The backside of the impeller incorporated a 1:20 taper to minimize the centrifugal stress and rotor mass. The analytical estimates for the hoop stress at the impeller hub with a 5.5 mm disc thickness were between 40 and 68 MPa, the higher value occuring at the front, untapered face of the impeller. An FEM model of the impeller disc was developed, and lead to a stress estimate of 70.1 MPa, the increased stress occurring primarily in the transition between the front face of the impeller and the hub. Both of these estimates are well below the 0.2% creep stress limits for Inconel 718 for temperatures up to 700°C. [W1] Relatively short, thick blades minimize the bending stress at the blade roots. Figure 5.2 shows the results of the FEM calculation for the stress in the impeller disc.

Due to the small inlet area and the thick blades, it was decided not to continue the blades all the way to the inlet, but rather to begin the blades at the 1/3 radius point. This means the impeller will be a pure radial flow machine. The rather abrupt transition from axial to radial flow increases the flow losses at the inlet, but greatly simplifies the impeller manufacture, since the resulting blades curve in only one plane.

The blade shapes are determined from the requirement that the flow enter the blade at zero incidence. The following figure shows the velocity triangles at a radius of 25 mm. These triangles require a blade angle of approximately 68° from radial.

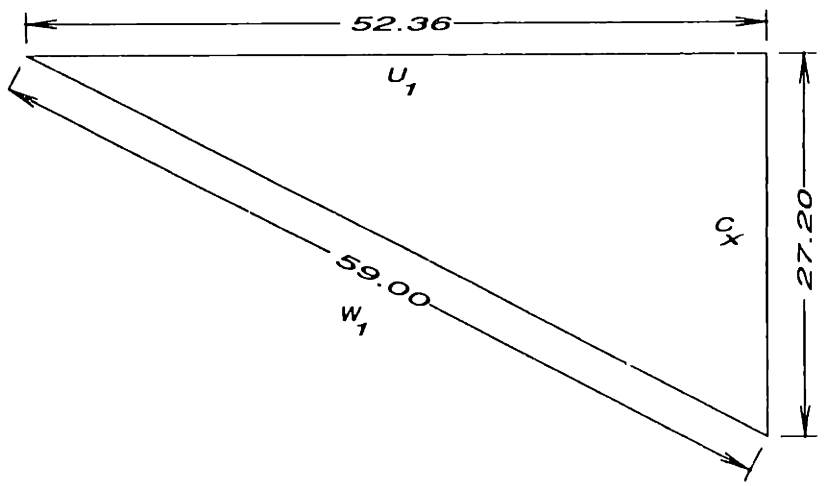

Figure 5.2
Velocity Triangles at Blade Inlet

The blades may take a number of shapes between the inlet and outlet, but for this relatively low efficiency design, it is hard to justify a profile more complex than a circular arc. The radius and center of this arc are chosen to give the desired flow angles at inlet and outlet.

The preceeding discussion incorporates a slightly more refined analysis than that used to design the actual impeller incorporated in the prototype DABLE circulator. Slightly different assumptions for mass flow rates and inlet areas were used in the original design. The design methodology used was identical, but the precise values differed by 5-10% from those presented above. The following series of tables and figures show the impeller as it was actually designed and built.

Table 5.3
Principle Dimensions and Operating Parameters of the DABLE Circulator

Temperature	T_{01}	500°C
Pressure	P_{01}	8.0 MPa
volumetric flow rate	$\dot{V}$	0.0186 m^3/s
rpm	N	20,000
polytropic efficiency (estimated total-to-total)	η_{tt}	60%
pressure rise	Δp	38 kPa
hub/shroud ratio at inlet		0.51
inlet flow angle		0.0°
blade angle at outlet	β_2	55°
absolute flow angle leaving rotor	α_2	77.8°
impeller diameter	d_2	125 mm
blade inner diameter		50 mm
blade height at inlet	b_1	5.62 mm
blade height at outlet	b_2	3.00 mm
shroud slope		4°
shroud diameter at inlet	d_{sh1}	29.15 mm
radial diffuser outlet diameter	d_3	150 mm
blade/shroud clearance		0.1–0.3 mm
blade tip radial clearance	$(d_3 - d_2)/2$	0.5 mm
shaft diameter at impeller		6.4 mm
impeller material		Inconel 718
axial velocity at inlet	c_x	27.2 m/s
rotor velocity at inlet	u_1	52.4 m/s
radial velocity at outlet	u_2	130.9 m/s
circum. velocity at outlet	$C_{\theta 2ac}$	83.6 m/s
abs. flow velocity at outlet	C_2	85.5 m/s
relative flow velocity at outlet	W_2	50.8 m/s

5.3.1. Pressure Vessel

Although an extremely low pressure-ratio machine, the circulator is required to operate at a high mean pressure and temperature. This requirement, combined with the extreme difficulty of sealing high-speed rotating shafts in helium, greatly limits the available options for the circulator housing and sealing system. At lower temperatures and rotational speeds, a canned rotor machine with permanent magnets might be considered, but the requirement of 20,000 rpm puts this out of reach of conventional technology. High-frequency synchronous drives with a canned rotor and impeller would give a very compact machine, but would likely require the impeller housing to be the primary pressure boundary while operating at the full loop temperature. While such a housing would not be impossible to make, it would likely have to be cast from a stainless alloy, and the development costs for a one-off prototype were considered excessive.

Tne solution to these problems used in the DABLE circulator was similar to that used in all modern gas-cooled reactors – a submerged motor pump. Since the high-pressure helium environment is compatible with properly designed electric motors, the drive system may be placed *inside* the pressure boundary, leaving only static seals at the vessel boundaries. With this choice of configuration made, the designer gains great freedom, particularly in the impeller housing design, which is no longer required to support the system pressure, but rather only the circulator pressure rise.

The pressure vessel for the DABLE circulator was built from 12" Schedule 80 piping, with 600 lb flanges connecting the two halves of the vessel. The vessel has two inlet/outlet nozzles, which are 3" Sched 160 pipes with drilled end caps. The main vessel is low-carbon steel, the nozzles are 316 SS. A photograph of the vessel as installed in the loop is shown in Figure 5.3, while the principle dimensions are given in Figure 5.4. The loop piping extends coaxially inside the inlet and outlet nozzles to connect to the circulator. The piping is welded to the nozzle ends; this weld is part of the primary pressure boundary for the vessel. These welds fix the vessel to the lower left-hand corner of the loop, as shown in Figure 5.5.

The vessel was designed in accordance with ASME standards. Meeting these standards while using off-the shelf components leads to a very large vessel, as can be seen in the pictures. Much of the mass is in the flange. A 300 lb flange yielded a marginally adeqaute design, so a 600 lb flange, the next commonly available size was selected. This leaves a substantial margin at an operating pressure of 8.0 MPa, since the flange is actually adequate for a 12 MPa design pressure. The vessel was hydrostatically tested by the manufacturer at 10 MPa. The calculations supporting the pressure vessel design are included as Appendix 1.

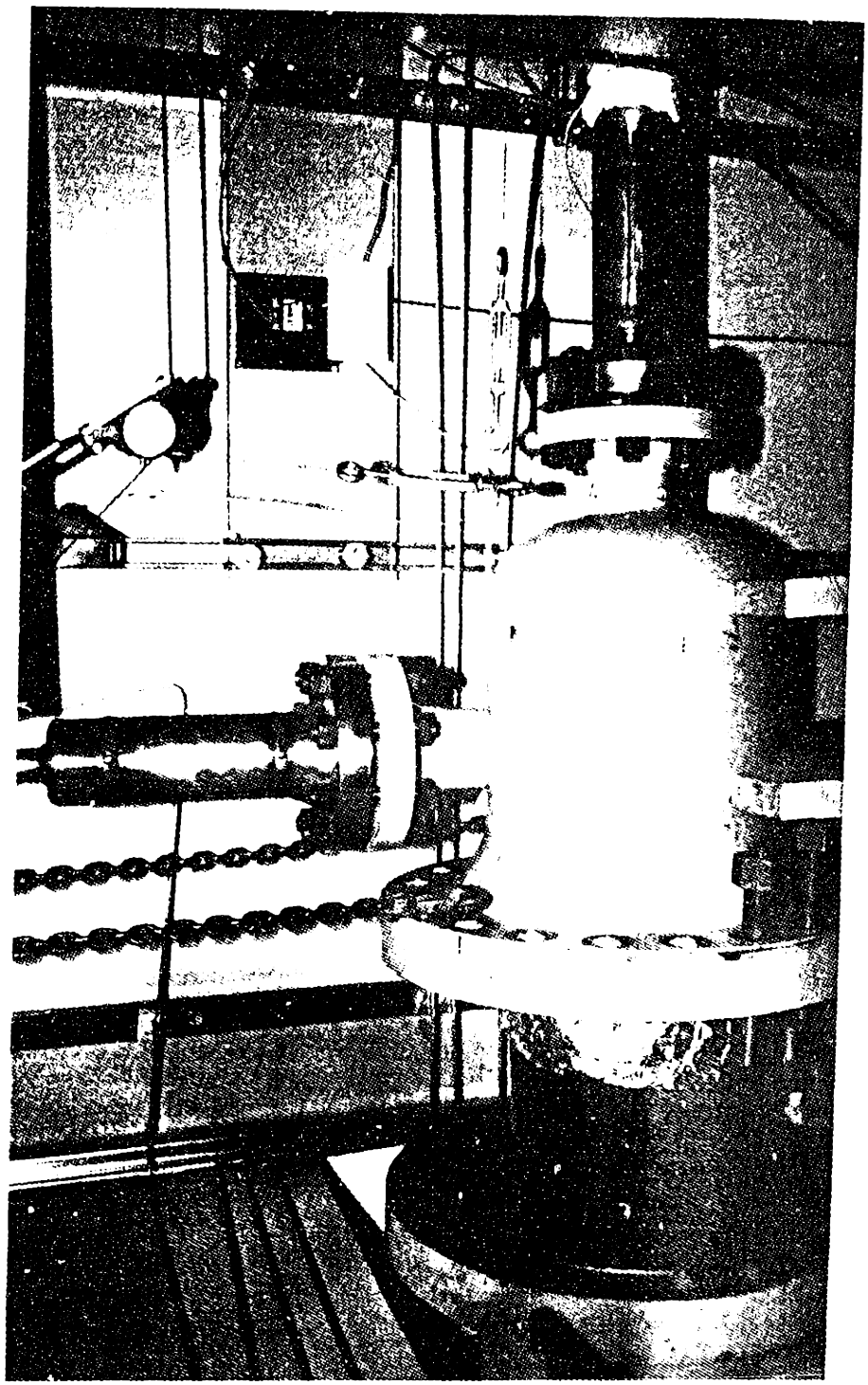

Figure 5.3
Pressure Vessel for Immersed Motor Circulator

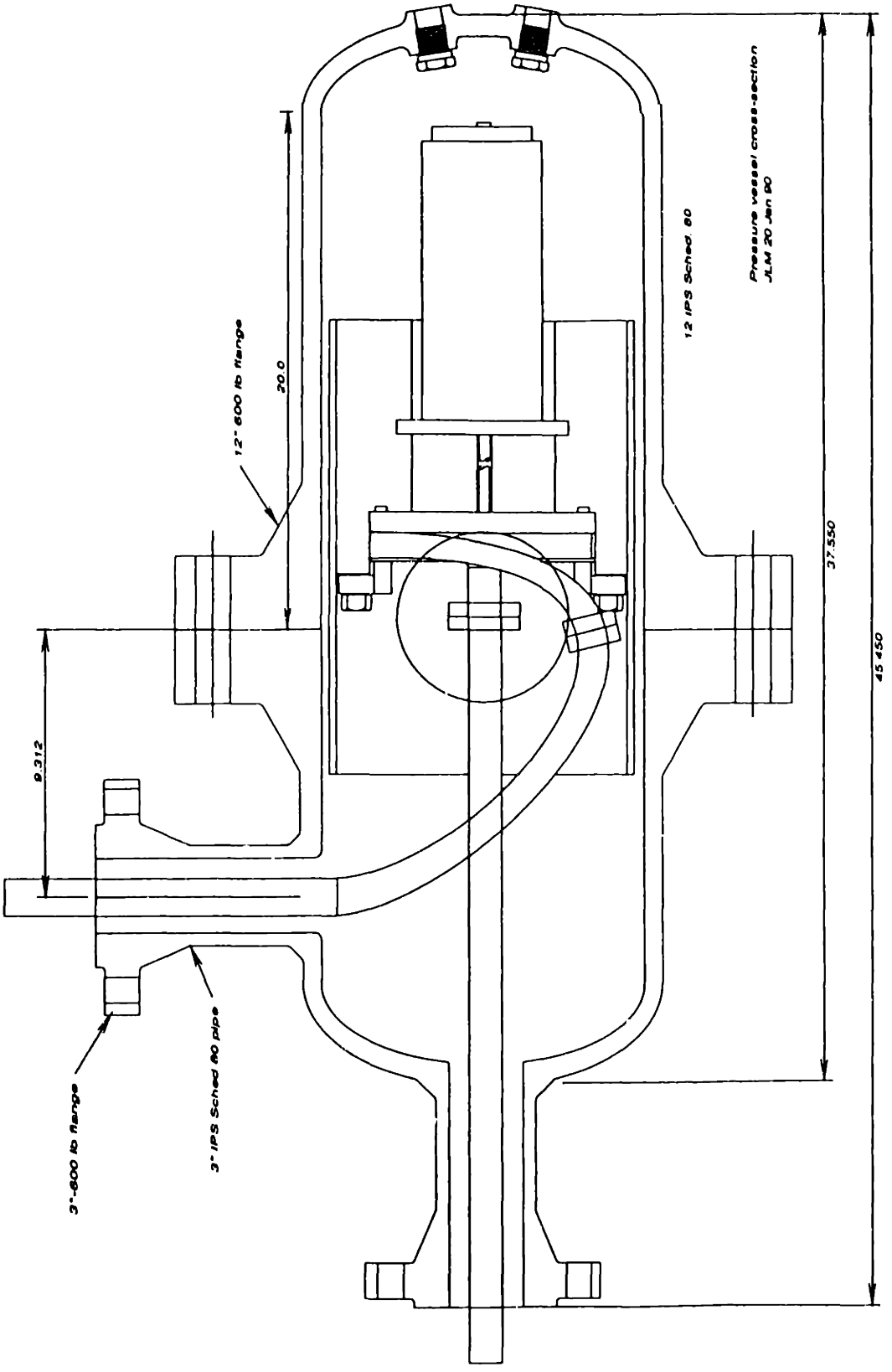

Figure 5.4
Pressure Vessel

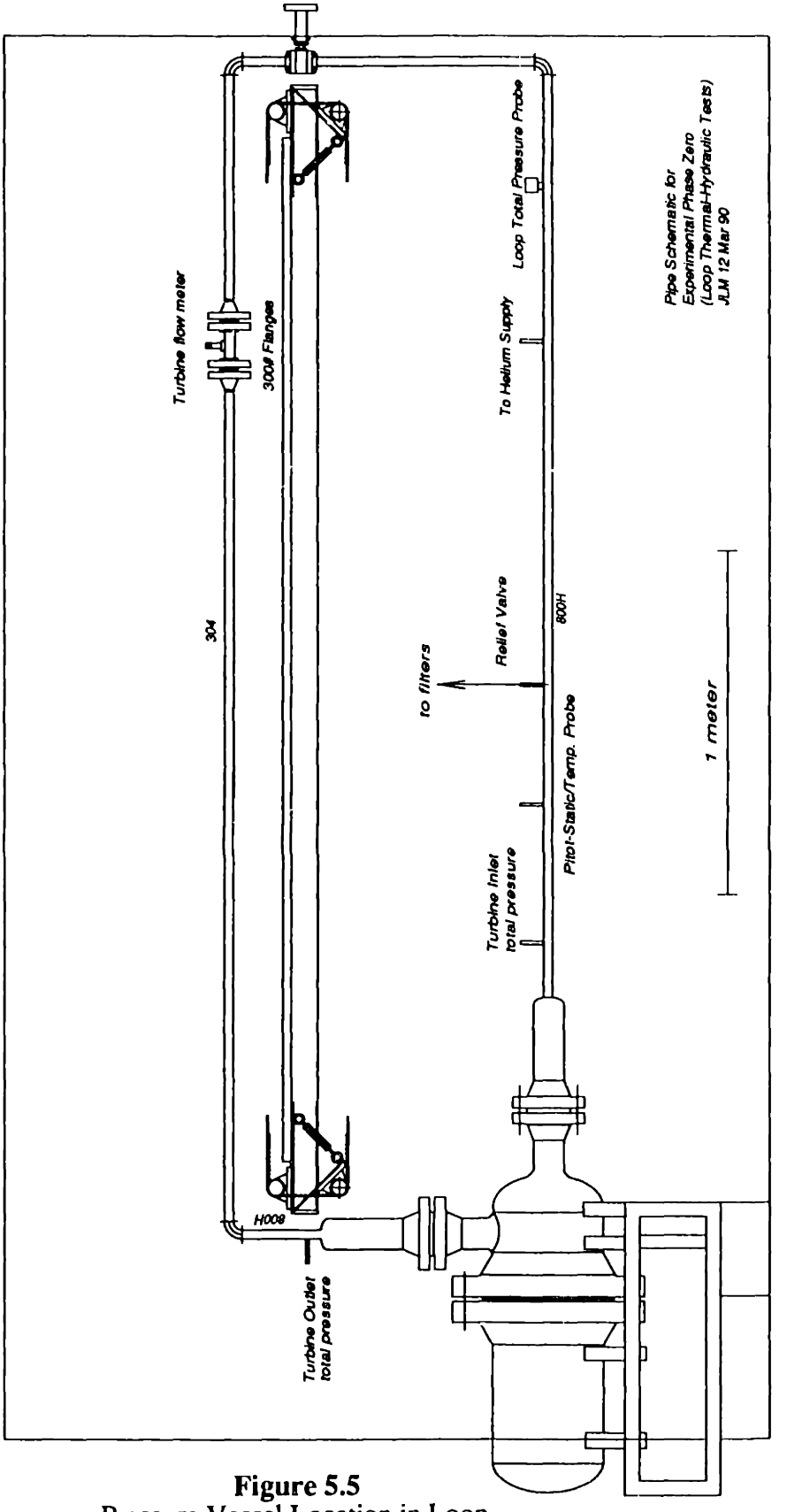

Figure 5.5
Pressure Vessel Location in Loop

The stainless steel nozzles provide a means for connecting the high-temperature piping to the carbon steel main vessel. Since the nozzles are small diameter, they can be economically fabricated from the more expensive material and do not require excessively thick walls. The space between the pipe and the nozzles is filled with silica-alumina insulation, so the heat transfer from the pipe to the nozzles is minimized. The nozzles then act primarily as fins, transferring the heat from the hot nozzle/pipe weld to the air.

If the radial heat conduction through the insulation is neglected in comparison to the axial heat transfer, and the temperature difference across nozzle wall thickness is neglected, then the nozzles may be analyzed as a one-dimensional fin problem. Writing an energy balance for a small slice of the nozzle dx long yields the following differential equation for the nozzle temperature:

$$kA\frac{d^2\theta}{dx^2} = hP\theta, \tag{5.14}$$

where

k is the thermal conductivity of the nozzle material

A is the cross-sectional area of the nozzle

h is the average heat transfer coefficient

P is the perimeter of the nozzle ($2\pi r_{nozzle}$)

θ $= T - T_\infty$

Or, in dimensionless terms

$$\frac{d^2\Theta}{d\xi^2} = (mL)^2\Theta, \tag{5.15}$$

where

Θ is the dimensionless temperature $\dfrac{T - T_\infty}{T_0 - T_\infty}$

mL $\equiv \sqrt{\bar{h}PL^2/kA}$

ξ $= x/L$

If we can neglect the heat transfer from the vessel end of the nozzle, the boundary conditions become

$$\Theta_{\xi=0} = 1 \quad and \quad \left.\frac{d\Theta}{d\xi}\right|_{\xi=1} = 0$$

with the solution

$$\Theta = \frac{\cosh mL(1-\xi)}{\cosh mL}. \tag{5.16}$$

The heat transfer from the nozzle is a result of both forced and natural convection. The forced convection is likely to dominate, with a flow of perhaps 1-2 m/s being provided by the hot cell exhaust fan past the vessel and nozzles. The natural convection alone will yield a heat transfer coefficient of at least 23 W/m^2°C for loop temperatures in excess of 350°C. Inserting the dimensions of the pipe and solving for the length where T is below 100°C gives a minimum nozzle length of 0.25 m. The actual required length will be slightly higher, due to heat transfer from the pipe to the nozzle through the insulation. For the as-built nozzles with a 0.30 m length, the temperature at the nozzle/vessel junction, using the assumptions given above was calculated to be 65 °C. A finite element model of the system found a the temperature at the nozzle/vessel junction to be 51 °C. The results of this calculation are shown in Figure 5.7

Both the main vessel flange and the two nozzle flanges were originally designed to utilize teflon-coated metallic O-ring seals. The seals received from the manufacturer seated too close to the flange inner edge, and were later replaced with elastomer rings. Since these seals are not exposed to the full loop temperature, they are adequate for use in experiments where the gas temperature is <350°C. For operations above this temperature, metallic O-rings will be used. The seals are supported radially in retainer plates. Two pins on the flange faces serve to center the retainer plates.

Thermal Management in the pressure vessel

Thermal management inside the pressure vessel presented an interesting design problem. There are two primary heat sources and regions within the vessel. In the "front" half of the vessel (the half containing the nozzles and connected to the loop), the hot helium supplies heat by conduction through the pipe and circulator housing to the helium inside the vessel. In the back half of the vessel, heat is supplied by conduction down the motor shaft and from the motor itself due to both windage and ohmic heating in the windings. The two regions of the vessel call for conflicting treatments of their thermal loads. In the front half of the vessel, the heat transfered from the gas to the vessel must be minimized, both to reduce the required heater power and variation in the gas temperature, and to maintain the vessel wall temperature within safe limits.

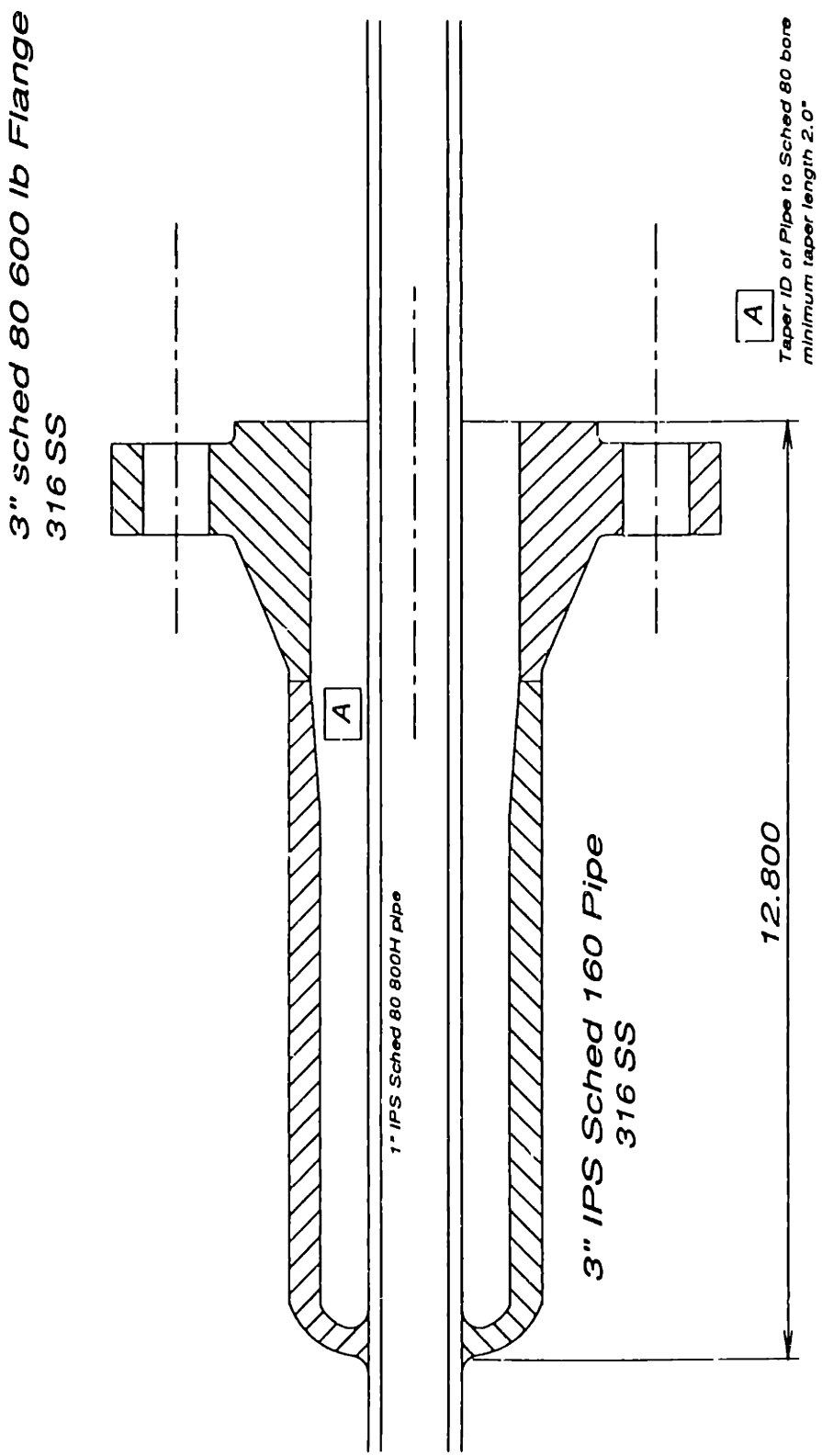

Figure 5.6
Cross-section of Nozzles

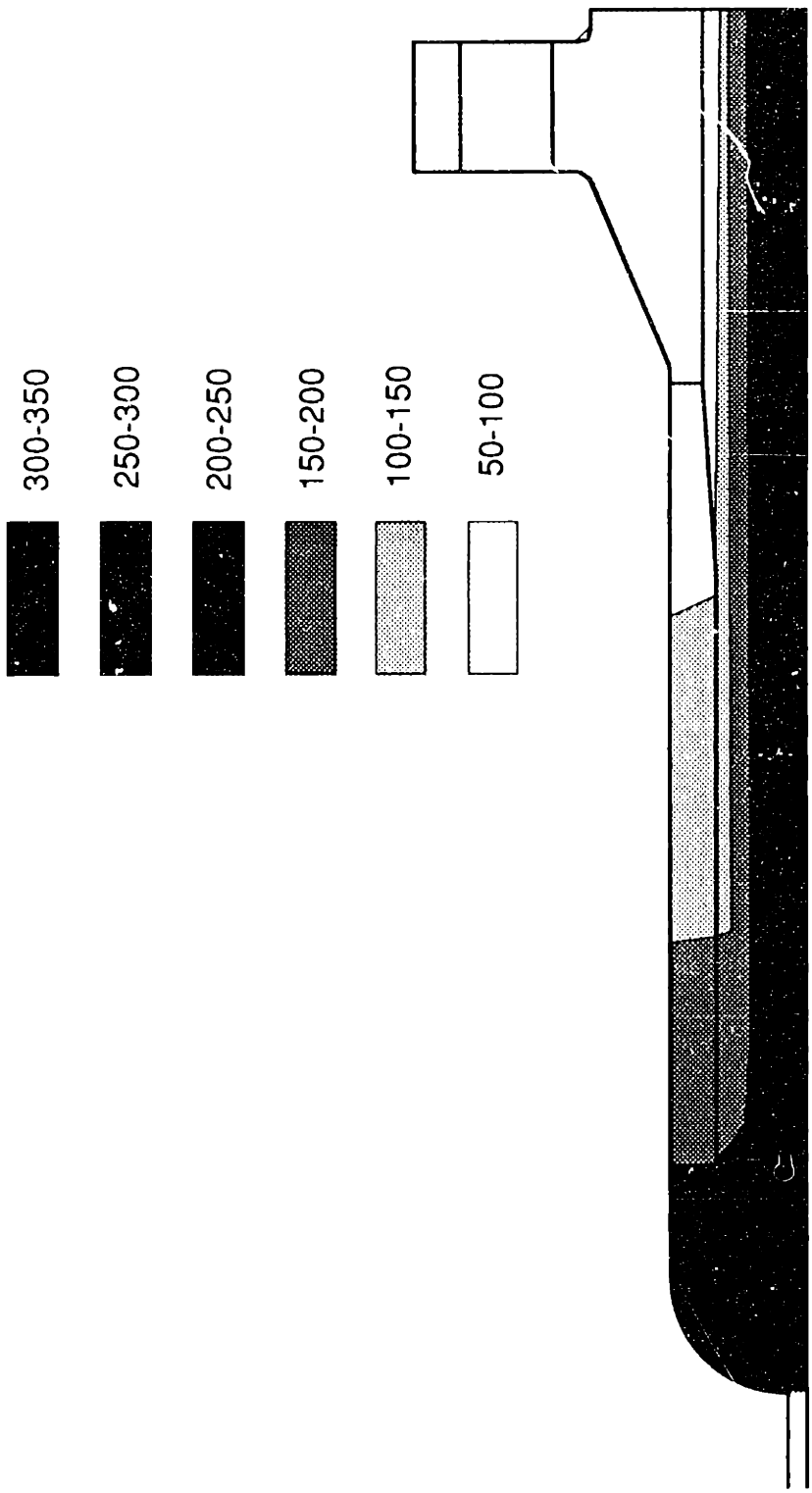

Figure 5.7
FEM Analysis of Heat Transfer in the Nozzles

In the back half of the vessel, behind the circulator housing, the opposite conditions prevail. In order to maintain the motor operating temperature at an acceptably low value, the heat transfer from the motor to the vessel walls and on to the ultimate heat sink in the atmosphere must be maximized. At full operating temperature and flow rate, nearly 300

watts of heat must be dumped to the atmosphere through the pressure vessel walls. Much of this heat load is due to the motor inefficiency, so the normal operating load is significantly less. The solution to these conflicting requirements was to fill the front half of the vessel with a fibrous silica-alumina insulation, while adopting measures to maximize heat transfer in the rear half of the vessel.

The main vessel is protected from the heat of the circulating helium by silica-alumina insulation. This insulation is shown schematically in Figure 5.8. The insulation fills the entire interior of the vessel from the nozzles back to a plane approximately half-way between the circulator housing and the motor face plate. The insulation reduces the heat loss from the loop and allows the use of a carbon steel main vessel. The average insulation thickness is more than 120 mm over most of the pipe length, dropping to 45 mm around the sides of the impeller housing. The thermal conductivity of the insulation used varies from 0.08 to 0.16 W/m°C in the temperature range from 20 to 700 °C. Assuming an average heat transfer coefficient of 40 $W/m^2°C$ at the vessel surface, the predicted vessel wall temperatures are in the range from 40 to 60 °C. These predictions are strong functions of the external heat transfer coefficient. Measured vessel temperatures near the back end of the vessel were approximately 30-40°C. The front half of the vessel remained below 30°C for all the experiments conducted thus far.

In the back half of the vessel, helium is circulated by the cooling fans on the motor, or by an auxiliary fan. The heat transfer coefficient is difficult to estimate, but measurements indicate a motor surface temperature of approximately 50°C when the inside vessel wall was at 30°C and the bulk helium temperature was 35°C.

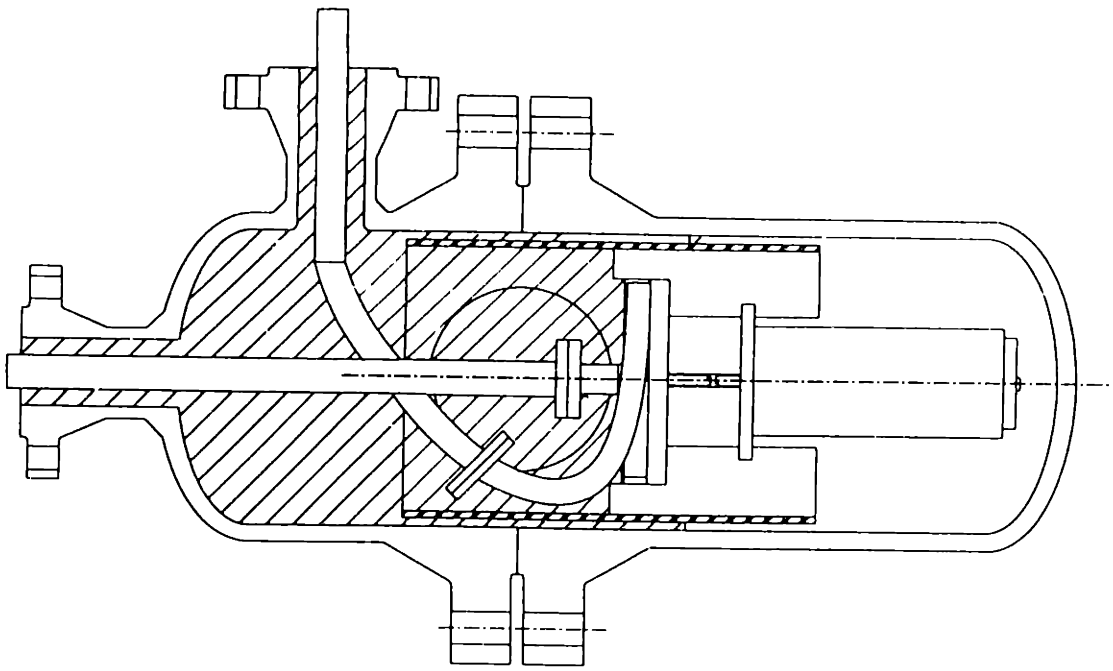

Figure 5.8
Pressure vessel internal insulation.

Pressure Vessel Supports

The front half of the pressure vessel is permanently attached to the loop by welds at the end of the nozzles. The back half may be separated from the front in order to gain access to the circulator internals. Doing this with a 300 kg pressure vessel was a major undertaking. In order to avoid any problems in assembling the vessel, a mobile support structure was developed for the pressure vessel. This structure placed the rear half of the vessel on a tracked cradle, allowing it to be slid away from the front half to expose the circulator. The cradle rides on steel wheels with ball bearings inside a steel track. this arrangement has proved a simple, and inexpensive solution to a vexing problem.

5.3.2. Circulator Housing and Motor Support Structure

The impeller housing and motor must be mounted in a fashion which will ensure their precise alignment. In order to facilitate this, and also to allow additional flexibility in testing the circulator, the circulator and motor are not mounted to the vessel, but rather to an independent supporting structure which was designated a "core barrel" for its resemblance to the core barrel in a PWR.

The core barrel consists of a 10" Sch. 5 pipe, (260 mm ID, 273 mm OD) 375 mm long, which slides into the main pressure vessel. Standoffs arranged at 120° intervals

around the pipe ends center the core barrel radially within the pressure vessel. Inside the core barrel, three ribs support a motor mounting plate and a form a resting space for the impeller housing. Three large access holes provide space for making up the inlet and outlet joints. The core barrel and its inner structure are shown in Figures 5.9 and 5.10.

The core barrel was assembled by welding the ribs and the motor mounting plate together, then welding the resulting structure into the core barrel. Afterward, the space for the circulator housing was bored out. This helped maintain the required colinearity and concentricity between the motor shaft and the impeller housing. Screws penetrating the three ribs provide a mechanism for final centering of the impeller housing. Hold downs on top of the impeller housing restrain it axially.

A major benefit of the core barrel arrangement is that it provides the capability of testing the assembled circulator outside of the pressure vessel. Since the design does not rely on the enclosing vessel for any critical alignment between parts, the circulator may be tested before inserting it into the vessel. This capability proved invaluable in the initial stages of the prototype development, when ease of access was paramount due to the need for frequent assembly and disassembly.

5.3.3. Drive System

Drive systems for laboratory scale, high-pressure and high-temperature compressors have been the source of difficulties for many researchers. Both the GA bench-top experiments and the Comedie loop experienced delays and setbacks due to drive failures [H7]. The DABLE circulator proved to be no exception. The need for small diameter impellers to keep the enclosing vessel diameter small, plus the preference for single-stage machines forces designers to rotational speeds beyond the range commonly available in commerical electric motors.

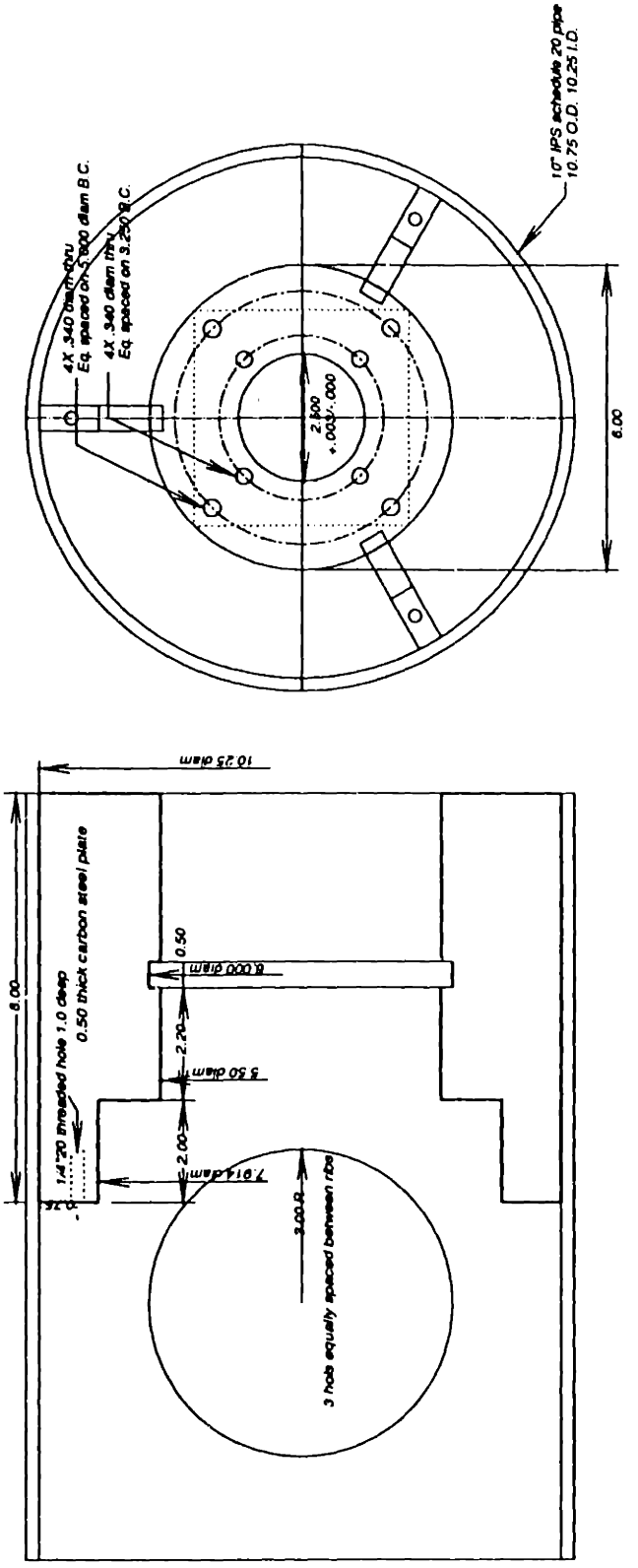

Figure 5.9
Circulator support structure-(core barrel)

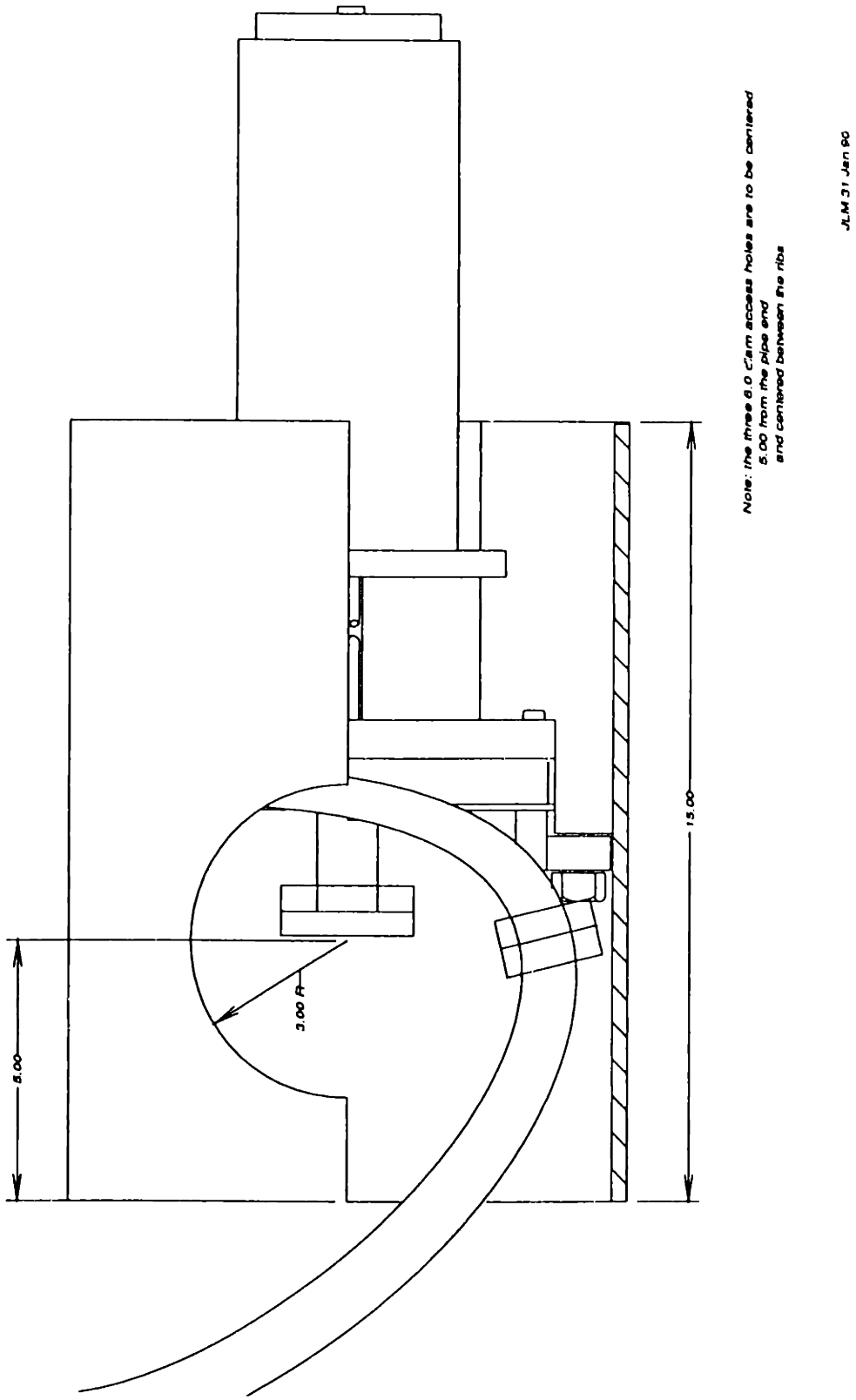

Figure 5.10
Core Barrel with circulator installed

As outlined in section 5.1, the circulator will require a drive of approximately 1.5 kW peak power, corresponding to 0.72 N-m @ 20,000 rpm. The power delivered to the gas stream is given by

$$\dot{W} = \Delta p \, \dot{V} \tag{5.17}$$

where

Δp is the pressure rise across the circulator, and

$\dot{V}$ is the volumetric flow rate [m^3/s]

The pressure rise is proportional to the square of the volumetric flow rate, while the flow rate is directly proportional to the motor speed. This means over the range of required flow rates, the power varies as the *cube* of the motor speed:

$$\dot{W} \propto rpm^3 \tag{5.18}$$

Most electric motors have power characteristics which vary more slowly than rpm^3, so a motor sized for the power requirements at the maximum rated speed will be adequate for use over the entire speed range.

For circulators of up to 1.5 kW, series-connected "universal" DC or AC brushed motors with speeds up to 30,000 rpm are cheap and widely available, but brush wear is a significant problem. In a dry helium environment, graphite brushes will bond directly to the copper commutators, leading to very high wear rates, so these motors are probably not suitable for continuous use without special brushes. High-speed induction motors using high-frequency converters are an option, but require sophisticated electronic drives, and possibly water cooling. High-speed motorized grinding spindles for use in machine tool applications have the advantage of both high speed and very stiff bearings, but proved to be too expensive for the DABLE application. These drives will be discussed in a later section. Brushless DC motors are capable of operation in the speed and power range required, but are generally custom-built, with attendant high prices. A final option is a high-speed switched reluctance motor, which has many of the features of the brushless DC motor. These drive options are summarized in Table 5.4.

Table 5.4
Comparison of electric motor technologies

Drive type	Principal Advantages	Principal Disadvantages	Cost
Universal	Very low cost, widely available	High brush wear, potential contamination from brushes, no active speed control	<$300
AC Induction	Simple structure, good speed control	Requires high-frequency drive	>$5000
DC Brushless	Closed loop control, compact	Requires sophisticated drive, temperature limits on Hall effect sensors	$2000-$5000
Switched Reluctance	Closed Loop control, simple structure, easy to cool	New technology, requires sophisticated drive and high-voltage electronics, switching noise can be a problem	$2000-$5000

The first motor used in the DABLE circulator was a switched reluctance motor from Pacific Scientific Co. The motor was the first commercial unit produced by Pacific Scientific to use their proprietary designs for a high-speed switched reluctance motor. Switched reluctance motors are commonly used in stepping motor applications, but the technology had only been recently developed to make high speed (>20,000 rpm) motors of this type. The drive electronics were produced by SemiFusion Corp of California. The SemiFusion electronics proved to work very well, utilizing a HP-IL command module which provided a transformer-isolated control system, and a simple command language.

The motor ran well outside of the pressure vessel, but problems developed when the power and control lines were fed through the pressure vessel. Switching noise from the drive circuits proved difficult to shield (the motor uses 5 Amp currents with a rise time of 50 ns), and there was a rather short limit placed on the maximum cable length. All of these problems were eventually overcome, and the motor would have continued to be used were it not for the difficulty of securing repairs and spare parts. Shortly after selling the motor to MIT, Pacific Scientific dropped the motor from its product line, and the developers left the company. After loosing a significant amount of time attempting to get the motor repaired, the drive was abandoned. Switched reluctance motors might be a near-ideal drive system for small helium circulators, but without a company actively supporting the technology, we consider them too risky.

After the decision to abandon the switched reluctance motors, our attention focused mainly on high-speed brushless DC motors. These motors use lower voltages and are more compact than the switched reluctance type, but were also more expensive. The final circulator design will utilize a slotless DC motor from Electric Indicator company. This drive had not yet been installed at the time of this writing.

Between the failure of the switched reluctance drive and the completion of the brushless DC drive, a simple universal DC motor was purchased to continue the circulator development and testing. This motor was originally part of a commercially available woodworker's router, a Cole Parker Model 690. It proved adequate for testing, and indeed, almost all the circulator performance data shown in this thesis was taken using this drive. The drive had one primary disadvantage–there was no closed-loop control system available, so experiments requiring accurate control of the motor rpm were not practical. Also, as expected, brush wear rates were very high, and the expected lifetime of the brushes was less than fifteen hours of continuous operation at 10,000 rpm.

5.3.4. Bearing System

In the original design for the circulator, it was intended to cantilever the impeller off of the motor shaft, relying on the motor bearings for both axially and radially restraint. This was potentially possible due the low mass and aerodynamic loading on the impeller. Neglecting the mass of the shaft with respect to the impeller mass, the first vibrational frequency for a uniform diameter shaft is given by

$$\omega_n = \sqrt{\frac{3E\pi d^4}{64\,L^3 m}} \qquad 5.19$$

where

- ω_n is the natural frequency of vibration,
- E is the Young's modulus of the shaft material,
- d is the shaft diameter,
- L is the shaft length, and
- m is the impeller mass

The first shaft used in the circulator was a uniform 9.5 mm ∅ shaft, 100 long. The impeller mass is ~0.2 kg. The first resonant frequency for this shaft is at 10,500 rpm.

It is possible to run the circulator at speeds beyond the first harmonic frequency, as long as the amplitude of the vibration can be limited during the run through resonance. During initial testing of the motor/impeller system, insufficient restraint was provided, and the shaft failed catastrophically when the impeller contacted the core barrel ribs. This failure forced a redesign of the shaft and bearing systems in order to achieve greater shaft stiffness and better restraint at near-resonance conditions.

Two different bearing designs were used in the testing of the circulator. The first was a simple journal bearing made of silver-impregnated graphite. This bearing acted mainly as a catcher bearing–its primary purpose being to restrain large amplitude oscillations during the run through resonant speeds. While the bearing did accomplish this goal satisfactorily,

the large clearance allowed for shaft oscillations, and the occasional impact of the shaft on the bearing walls made for noisy operation. For continued testing, the silver/graphite sleeve bearing was replaced by a needle bearing. The needle bearing allowed stable operation at speeds up to 21,000 rpm, but limited the maximum circulator operating temperature to less than 260 °C when using an aluminum hydroxide lubricant.

None of these bearing designs were truly satisfactory, and the bearings remain a continued source of problems for the circulator. In a later section, an alternate shaft and bearing design will be presented which should avoid many of the problems associated with the current implementation.

Chapter 6

OTHER LOOP SUBSYSTEMS

6.1. Temperature Measurement and Control

6.1.1. System Description

Temperatures in the DABLE loop are measured using type K thermocouples. Thermocouples are provided at intervals along the pipe to measure the pipe wall temperature, and penetrating the pipe wall to measure the gas temperature. The location of each thermocouple is shown in Table 6.1. The output of each thermocouple is directed to either a heater section controller, the data acquisition board, or to a temperature display. In addition to the probes on the loop itself, thermocouples penetrate the circulator pressure vessel to monitor the drive motor temperature.

6.1.2. Thermocouple Locations

Table 6.1
Thermocouple Locations and Connections

Thermocouple #	location	connected to
	lower leg	
	(distances from nozzle)	
1	100 mm	data acq.
2	300 mm	heater controller
3	300 mm	display
4	500 mm	data acq.
5	750 mm	data acq.
6	1000 mm	heater controller
7	1400 mm	display
8	1400 mm	data acq.
9	1700 mm	data acq.
10	1900 mm	heater controller
11	2150 mm	display
12	2150 mm	data acq.
13	2540 mm	display
	test section	
	(distances from upper left)	
14	150 mm	data acq.
15	450 mm	heater controller
16	450 mm	display
17	750 mm	data acq.

18	900 mm	data acq.
19	1350 mm	heater controller
20	1350 mm	display
21	1500 mm	data acq.
22	1650 mm	data acq.
23	1900 mm	heater controller
24	1900 mm	display
25	2000 mm	data acq.
26	2650 mm	data acq.
27	2850 mm	heater controller
28	2850 mm	display
29	3150 mm	data acq.
30		

6.1.3. Wall and Gas Temperature Comparison

The thermocouples for measuring the wall temperature are bare-wire 20 ga., type K thermocouples with an quoted accuracy of ± 2.2 °C up to 277°C, and 0.75% at temperatures to 982°C. They are threaded through ceramic insulators and fit through holes in the pipe insulation. In the first tests of the heaters, the thermocouples were spot-welded to the surface of the pipe, but a combination of differential thermal expansion and fatigue from vibration of the connectors caused the thermocouples to fail at temperatures between 300 and 600 °C. Several alternate methods of attachment were tried, but the most effective seemed to be inserting the ceramic insulator into a tightly-fitting hole in the pipe insulation and keeping it pressed against the pipe wall with a wire wrapped around the insulation. This system is illustrated in Figure 6.1.

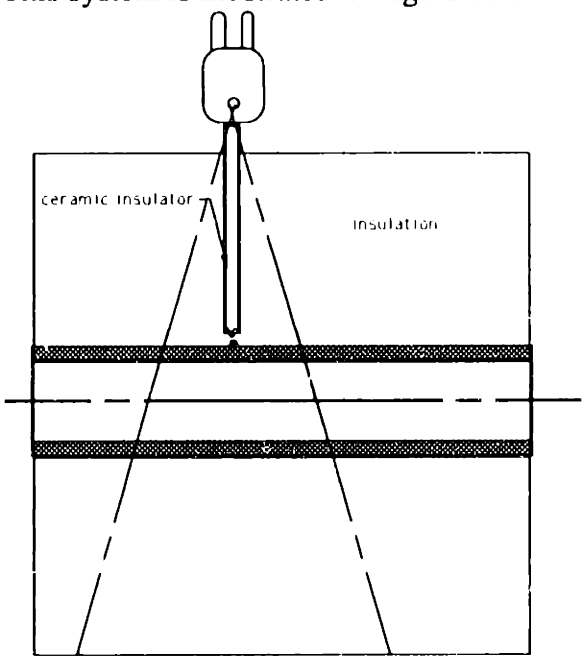

Figure 6.1
Thermocouple attachment to pipe wall.

Gas temperatures in the loop are measured by two sheathed thermocouples, the first inserted near the entrance to the test section, and the second near the circulator inlet. The second is part if the pitot-static temperature probe, so we can be sure of having the correct local stagnation temperature when velocities are calculated from the pitot-static probe pressures.

Except in experiments where large variations in temperatures along the test section are imposed, the wall temperature measurements should be very close to the gas temperatures, since the heat transfer coefficient from the gas to the walls is high.

6.1.4. Signal Processing

Two signal processing systems were utilized in the course of the development of the facility. Due to the potential hazard to the data acquisition system posed by the presence of high (>30 volt) voltages near the thermocouples, some method of signal isolation was deemed necessary to protect the data acquisition electronics and the computer controller. This signal isolation proved to be expensive due to the relatively high per-channel cost of the necessary isolation amplifiers. In an attempt to reduce the cost of assembling the earliest test configurations, the signal train illustrated in Figure 6.2 was conceived and implemented.

This system has the advantage of placing the multiplexers behind the 4-to-1 multiplexer, reducing the required number of amplifiers by a factor of four. It has two principal disadvantages: it places the multiplexer at risk, and reduces the bandwidth of the signal channel. The multiplexer is on an unisolated line, a risk which might be tolerable considering the low cost of this unit. More importantly, this arrangement resulted in a drastic reduction in the bandwidth. This reduction is due to the extremely low bandwidth of the Analog Devices 5B37 thermocouple isolation amplifiers, which have a -3 dB falloff at 4 Hz. The effect is less important for thermocouples reading closely spaced temperatures, but for wide thermocouple-to-thermocouple variations, the maximum scan speed which produced acceptable accuracy was only 0.25 Hz. Sixteen-thermocouple scans with five readings per thermocouple took 320 seconds, perhaps adequate for monitoring of steady state temperatures, but insufficient for transients. For this reason, the arrangement of Figure 6.3 was adopted, with increased cost and complexity as the price for larger bandwidth.

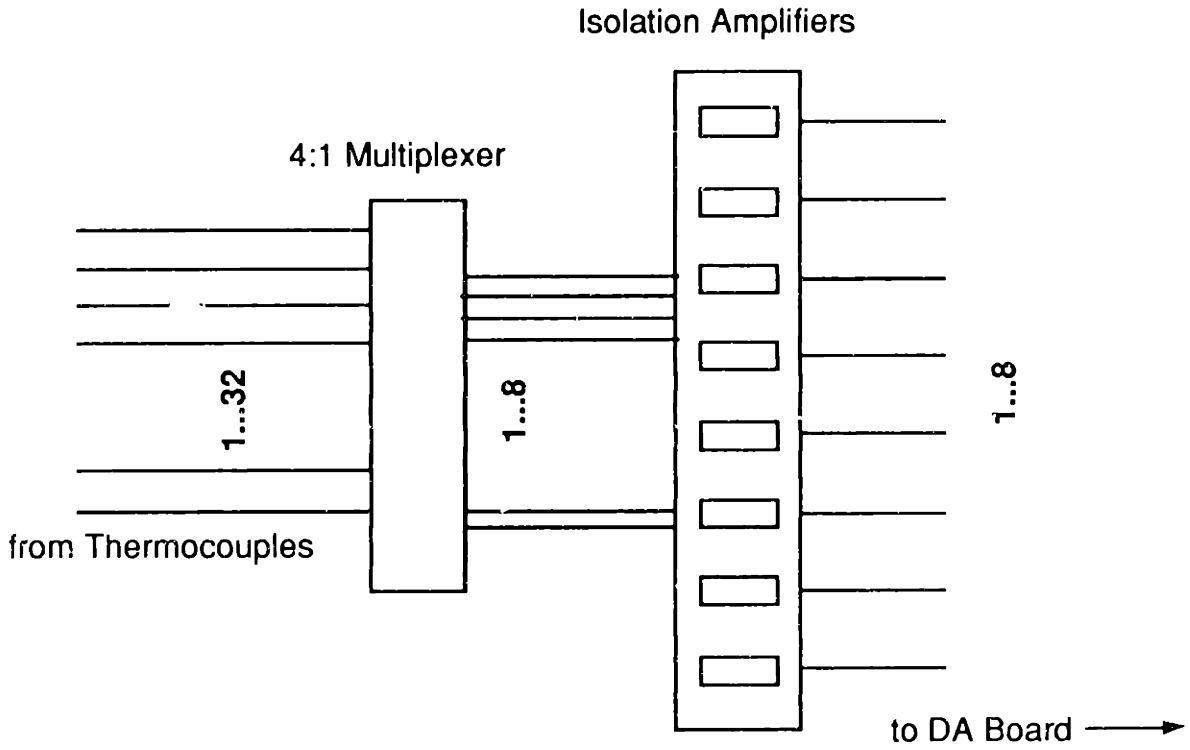

Figure 6.2.
Signal Processing
with Multiplexer Before Isolation Amplifiers

6.1.5. Accuracy

The isolation amplifiers provide a 0 to +5 V signal over the temperature range from -100 to 1350 °C. They also provide cold junction compensation, with and accuracy of 0.25 °C The signals are digitized by a 12-bit A/D converter, yielding a 1.77 °C resolution in the digitized value. The final expected accuracy is approximately ±3 °C for temperatures near 500°C.

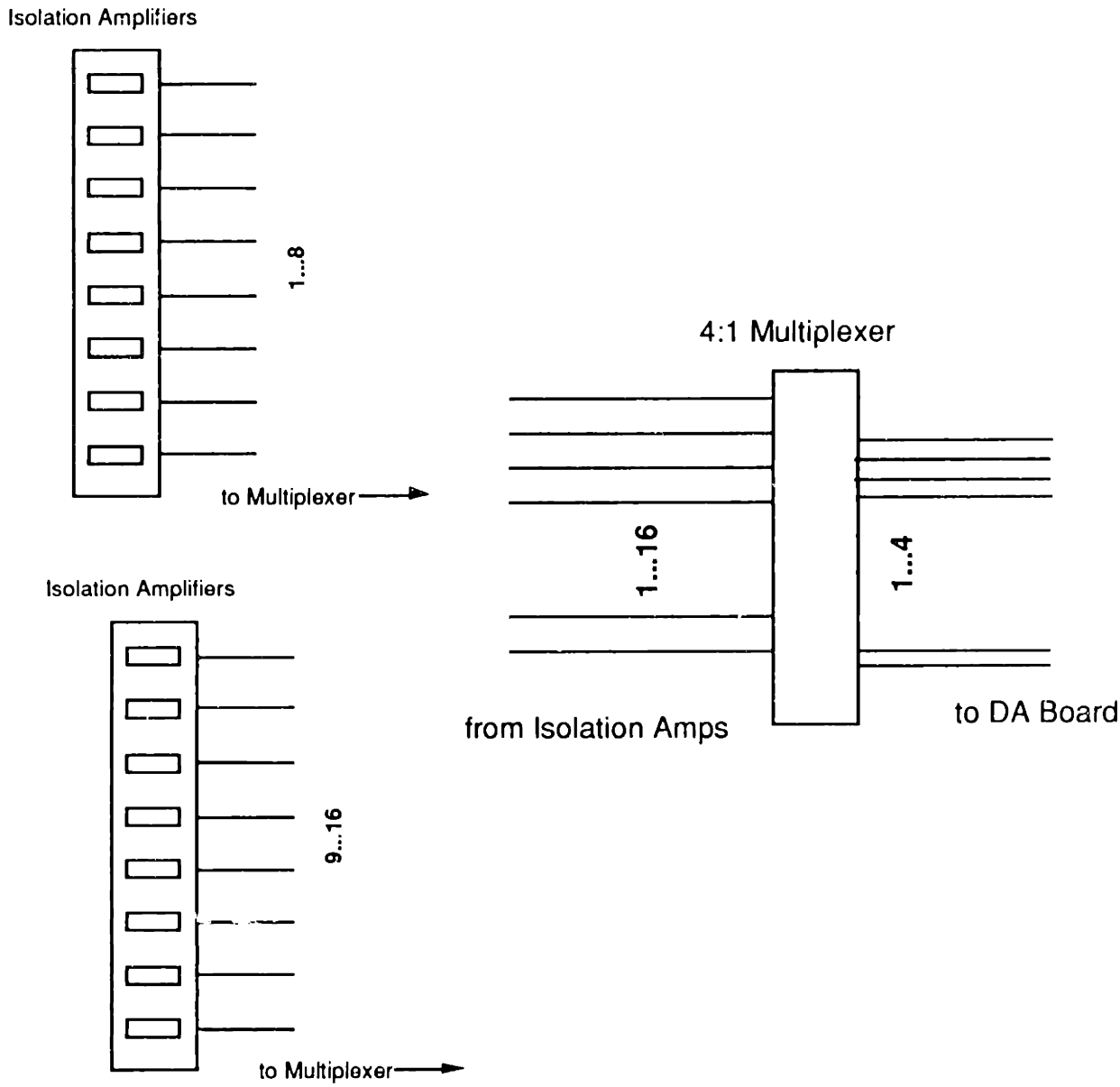

Figure 6.3.
Signal Processing
with Multiplexer after Isolation Amplifiers

6.2. Gas Purity Measurement and Control

6.2.1. Gaseous Impurities in HTGR Coolants

In the absence of dust, the nature of the fission product deposition in HTGR's is controlled primarily by the trace contaminants in the gas stream. Therefore, for both operating plants and research facilities, the monitoring and control of gaseous contaminants is a key issue. The configuration of the loop at the time of this writing

includes provisions for only the monitoring of gaseous contamination; control systems will be implemented in a later stage of the project.

The primary contaminants expected in the MGR are shown in Table 6.2. [H4]

Table 6.2
Gaseous contaminants in MGR primary coolant

Species	Design Value
0_2	-- ppm
N_2	-- ppm
CO_2	20 ppm
CO	50 ppm
H_2O	20 ppm
H_2	100 ppm

The surface chemistry, and particularly the formation and stability of oxide coatings on metallic surfaces, will be controlled by the oxidation potential of the coolant. The oxidation potential is set by the CO/CO_2 ratio and the H_2/H_2O ratio. Nitrogen is present primarily from air trapped in the system prior to filling with helium, as is water. CO and CO_2 are products of the reaction of oxygen with the graphite in the core. The design values for hydrogen, water, carbon monoxide and carbon dioxide are consistent with equilibrium of the reaction

$$H_2 + CO_2 \Leftrightarrow CO + H_2O$$

at a temperature of 641 °C. Their values at other temperatures can be found from the standard free energy change for the reaction[ref]

$$\Delta G^{\circ}_T = 3.76\text{x}10^4 - 3.54\text{x}10^1\ T \text{ (Joules)}$$

which yields for the ratios of the gases

$$\frac{\left(P_{CO}/P_{CO_2}\right)}{\left(P_{H_2}/P_{H_2O}\right)} = \exp\left(\frac{-4.52\text{x}10^3}{T} + 4.25\right)$$

6.2.2. Gaseous Impurity Measurement in the DABLE Loop

The DABLE loop is investigating the practicality of monitoring the gas composition with a quadrupole residual gas analysis unit (RGA). A quadrupole RGA is a mass spectrometer which operates in the high vacuum pressure range. It works by ionizing gas molecules during impacts with a heated filament, then sorting them with magnetic and electrical fields. The output of this device is a plot of current (due to the ions travelling between two electrodes) vs the mass to charge ratio of the ion. For example, argon will yield peaks at 40 ($_{40}Ar^+$), 38 ($_{38}Ar^+$), 20 ($_{40}Ar^{++}$), and 19 ($_{38}Ar^{++}$). A typical scan of air is shown in Figure 6.4.

An RGA unit consists of a high-vacuum pump, a backing pump, a heated filament, the analyzer head, a electrometer and amplifier, and the control electronics. The system used in with the DABLE loop is a Dycor™ RGA, with a Balzers 50 L/min turbopump as the high vacuum side and a Leibold rotary vane pump as a backing pump. The vacuum system sits inside the hot cell, while the driving electronics are rack mounted outside the cell. The unit is autoranging over fifteen orders of magnitude in electrometer current, with a usable range of six orders of magnitude in a single scan. In Figure 6.4, the CO_2^{++} peak represents 10 ppm of the total signal. In addition to the CRT included in the controlling electronics, the RGA may be controlled through a RS-232 port and an external computer. Custom software was developed as part of this project to retrieve and automatically analyze the data from the gas analyzer.

Since the RGA is a vacuum range instrument, a pressure reduction system is required before it may be connected to an atmospheric or higher pressure sampling chamber. For connecting to the DABLE loop, a two-stage pressure reduction system was used. The first stage used a standard adjustable pressure controller. This all-stainless unit (Tescom model 44-2200) allowed a controlled outlet pressure of 0 to 30 kPa gage to be maintained while the loop operated at 3 to 8 MPa. The second stage of pressure reduction was accomplished by inserting a capillary tube between the pressure reducing valve and the RGA vacuum system. The capillary is a 1 meter length of fused quartz with an internal diameter of 50 μm. The capillary operates in laminar flow over almost all of its length, minimizing the effect of differential pumping on the sampling.

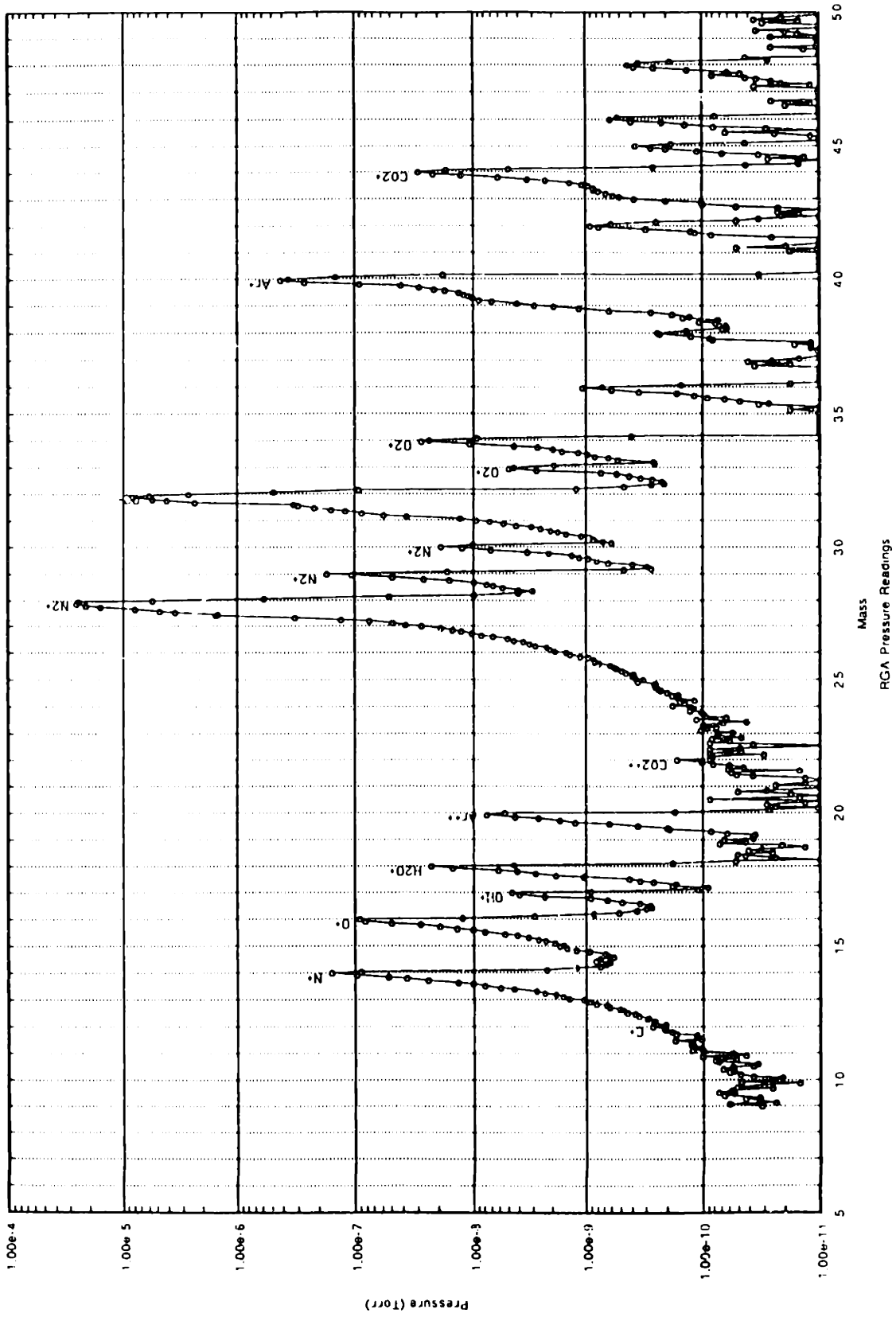

Figure 6.4
RGA Scan of room air

The RGA has not yet been fully calibrated with the entire pressure reduction system, so all data from it should be considered qualitative. The unit will be calibrated by introducing a gas of known composition into a sampling chamber connected to the pressure reduction system. This known sample will be used to adjust the peak heights over the range of the instrument. Preliminary calibrations using air were used to adjust the instrument before taking the scans shown in the next figures. Figure 6.5 is a scan of the residual gas in the vacuum chamber itself, with the sampling valve connected to the capillary closed. This background spectrum is dominated by water adsorbed on the surfaces of the vacuum chamber, and decreases slowly over time. It could be reduced to lower levels by vacuum baking. This spectrum is subtracted from the spectrums obtained by sampling the loop, shown in Figure 6.6. This scan shows the primary gaseous contaminants in the loop to be H_2O, N, and Ar. One problem with the use of the RGA is the presence of overlapping peaks, among them two important peaks, the N_2^+ at 28 and the CO^+ at 28. To some extent, the peaks may be discriminated by their isotopic splitting and by the double ionization peak of the nitrogen, but this becomes decreasingly accurate at low partial pressures. Because of these and other problems, it is doubtful that the current analysis method will yield results to better than 100 ppm without futher calibration with the gases of specific interest, and an accounting for differential pumping. As can be seem from Table 6.2, this detection level is insufficient for quantitative analysis of the gaseous impurities in the helium stream. Nonetheless, the technique shows promise, and with proper calibration and analysis software, could be used for quantitative measurements on all the gases of interest, with the exception of hydrogen, which suffers both from the noise present at the extreme low end of the instrument's measuring range and pumping difficulties. There are a number of instruments, however, which could be used to monitor the hydrogen level, should that be deemed necessary. It is likely however, that the hydrogen content in the loop will simply be maintained as low as practical.

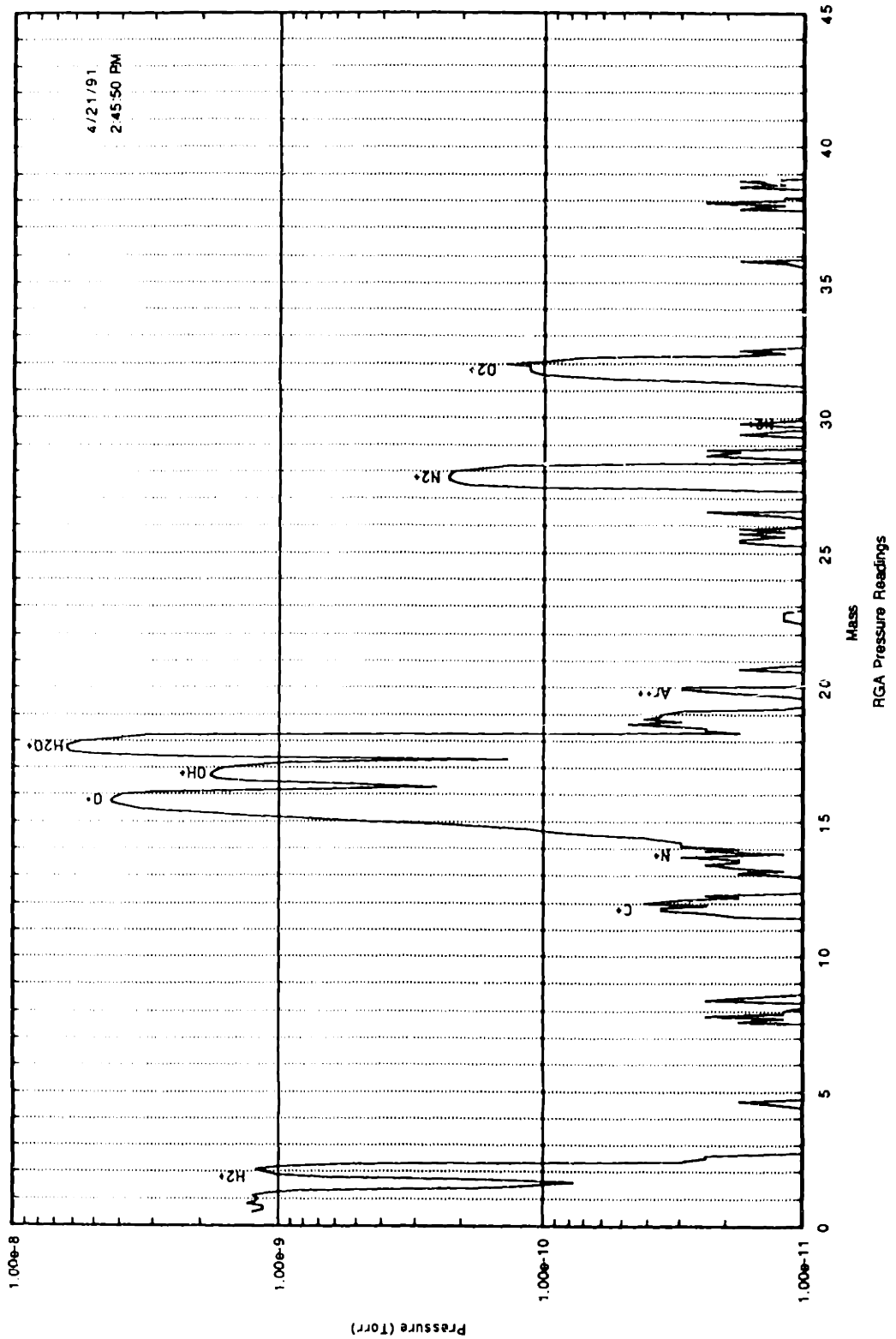

Figure 6.5
RGA Scan of Vacuum System Background

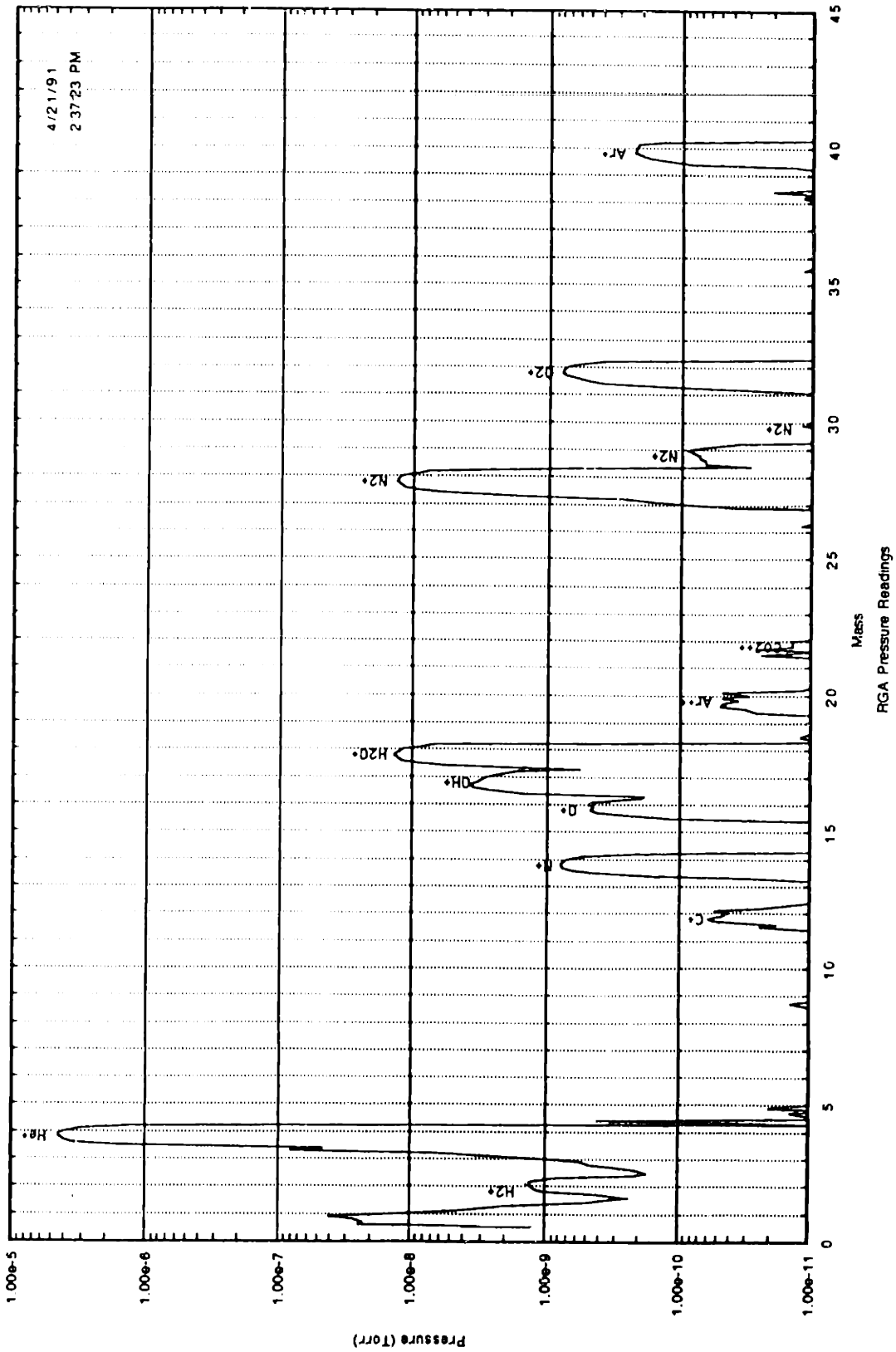

Figure 6.6
RGA Scan of Loop Atmosphere with Background Subtracted

6.2.3. Gaseous Impurity Control in the DABLE Loop

From experiences in other, similar loops [ref] and from preliminary measurements in the DABLE loop, it has been determined that the primary species of interest for a gas purity control system will be H_2O. H_2O can be removed from high temperature helium by absorption on activated charcoal beds. The H_2/H_2O ratio is a key element in determining the formation and stability of oxide films on the test section walls. The current plan for H_2/H_2O control in the loop is to divert some fraction of the gas flow through heated copper oxide beds followed by activated charcoal absorbers and molecular sieves. This is the same system used in the LAMINAR loop[Röllig]. The cleanup system would likely be connected directly between the circulator inlet and outlet. One potential problem is the high pressure drop which is associated with such a cleanup system. Since the circulator provides such a limited pressure rise, any parasitic losses, such as those incurred in the cleanup loop, could have a significant impact on the maximum flow velocities available.

There is an alternative, however. Since the required flow rates through the cleanup system are small, and there is no need for extremely high temperatures, the cleanup loop could be provided with its own compressor and heater. By cooling the gas to near room temperature before compression, a diaphragm compressor could be used, followed by the cleanup systems and a gas heater. For bypass flow on the order of 5 to 10% of the main loop flow, such a system could be compact and relatively inexpensive. Further design of the system will have to wait for measurements of the gaseous impurities in the loop.

6.3. Flow Rate Measurement and Control

Among the key measurements to be made in this facility is the effect of bulk flow parameters (Reynolds number, wall shear stress, etc.) on the deposition and liftoff of radioisotopes. For this reason, the accurate measurement of helium flow rate is paramount to the understanding of the flow phenomena under study. Several methods are envisioned for the measurement of flow rates in the loop; of these two have been implemented and a third is under development.

The two methods which have been implemented in the first phase of the project are a turbine flow meter and a pitot tube system. The turbine flow meter is a Hoffer model H01X1-15. It works by passing the flow through a propeller. Under the conditions in which the unit is linear, a known volume of gas passes through the device with each turn of the propeller. By sensing the rotational frequency, a direct measurement of the volumetric flow rate is obtained. This type of device has a number of advantages: good linearity over a wide flow range, direct measurement of the volumetric flow rate, and

good resolution. Its limitations are: a high starting torque, which limits the accuracy at low flow rates or low pressures, a temperature limit below the required loop operating temperature, and a poorly documented effect of gas density. For these reasons, the turbine flow meter is primarily applicable to flow measurements in the range of 10 to 40 m/s at temperatures between 0 and 250 °C and for gas densities in excess of 3 kg/m^3 (corresponding to 3.3 MPa at 250°C). It was used to calibrate and verify the output of the pitot tube.

The pitot tube is a Northern Controls model PAC-T-18-C/A-KL tube with a 3.175 mm Ø probe. The pitot tube is located in the lower leg of the loop, just in front of the circulator inlet nozzle. The probe measures total and static pressures and also includes a type K thermocouple to measure the gas temperature. The high and low pressure output of the tube are connected via 6.35 mm tubes to a Viatran Model 123 differential pressure gage. This gage allows the measurement of differential pressures of less than 4.8 kPa on top of the ~ 6 MPa system pressure. With a resolution of approximately 0.25% full scale, this means that the pitot tube can accurately measure flows with velocities greater than 4.6 m/s. Together, the pitot tube and the turbine flow meter provide good coverage of the flow range from 5 to 35 m/s.

Another potential flow measurement method, mainly applicable to the lower flow rate range, is to infer the flow rate from the circulator rpm. Over a practical range of pressures and flow rates, the circulator flow rate is a linear function of the circulator rpm, as can be seen from Figure 6.7. The slope of this curve is, of course, a function of the flow resistance of the loop, but this can be measured with the pitot tube at higher flow rates. Then, with this calibration, the flow rate can be inferred with good accuracy from the circulator rpm alone. By using this technique, the minimum measurable flow rate can be extended down to 2 m/s. In chapter 7, these observations will be further quantified with experimental data.

6.4. Iodine Source

The iodine source will be connected to the loop in phase 1 of the experimental program (iodine deposition tests). The source has been designed in a cooperative effort with researchers at the Oak Ridge National Laboratory. Several design options were investigated by ORNL before the final version was developed. We are now confident that the source could be implemented with minimal difficulty.

The original plan for a iodine source for the loop was to use a closed graphite tube with iodine inside. The tube would be heated and the iodine would diffuse through the porous tube walls. This design had several disadvantages. The two most important of

these were the lack of data on such sources and the high vapor pressure of elemental iodine at room temperature. During discussions with engineers at ORNL, several design goals were identified for any radioisotope source to be used in the project. The following table lists the features of an ideal radioisotope source

Features of an ideal radioisotope source

- low vapor pressure at room temp
- easy to manufacture
- simple to control
- has a predictable, reproducible output
- does not use exotic materials
- contaminated parts easily replaceable
- capable of high pressure operation
- source strength does not vary with time (except for decay)

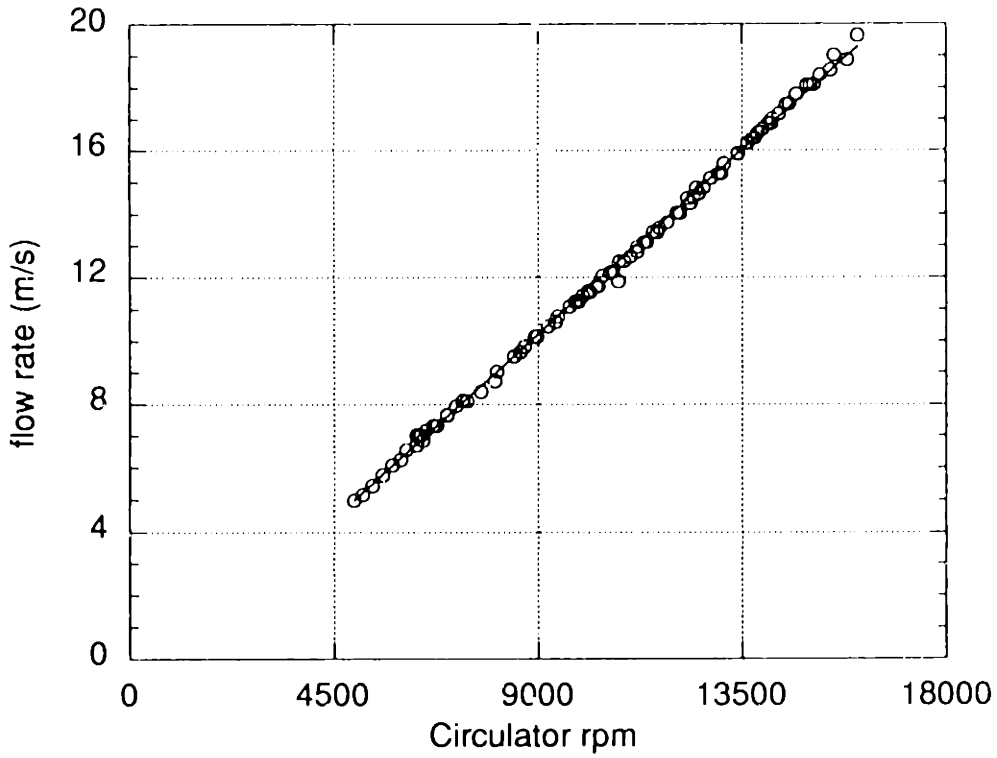

Figure 6.7
Flow Velocity vs Circulator rpm

Against this standard, we evaluated a number of different iodine sources. The first source considered was a palladium iodine source. This source was used in iodine deposition experiments performed in 1989 by scientists at ORNL.[M7][C4] The source consisted of a palladium wire, approximately 50 mm x 0.5 mm diameter, onto which had

been deposited iodine. The source was made by passing a flow of helium over a solution of NaI in HNO_3, with sodium sulfite used as a catalyst to oxidize the iodine to elemental iodine. The helium flow containing the iodine and NaOH passed through a quartz tube (to react the NaOH), and then over a palladium wire heated to 200°C. The iodine not deposited on the wire was caught in a room-temperature charcoal trap.

The palladium source had the advantage of being relatively easy to handle once created, with a nearly negligible vapor pressure at room temperature, and a wire form which was easily manipulated remotely. The production procedure was relatively straightforward, but even so, was more complex than we were comfortable with, particularly because of the presence of elemental iodine vapor during the preparation. The source was ultimately abandoned when difficulties arose in scaling it to the necessary ~ 10 mCi level predicted to be needed by the DABLE loop.

ORNL then tried several minor modifications of this source, including desorption sources where the iodine was deposited on the source material at relatively low temperatures (~200°C), then desorbed at a higher temperature (~ 500°C) to form the source. Experiments were made using both T-22 (2-1/4 Cr 1 Mo steel), and Inconel 800H.[M8] Another source design using NaOH solution adsorbed on a quartz frit was investigated, but abandoned because too many organic iodides were formed.

The final version of the source was developed in the summer of 1990 and tested at ORNL.[M2] The source consists of a small boat formed from 2.25 Cr - 1Mo sheet, filled with fine steel wool. The iodine, in a NaOH solution, is pipetted directly onto the steel wool. The system is then dried, heated to 300°C to drive off any organic iodides, then cooled. The remaining iodine can be removed upon heating to >400°C. The vapor pressure of this source vs temperature is shown in Figure 6.8

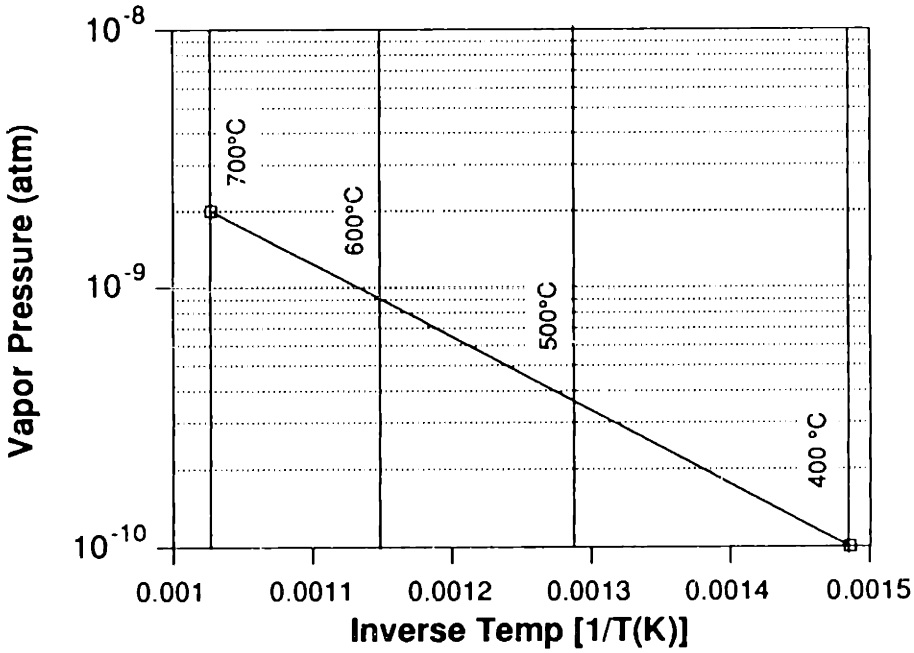

Figure 6.8
Vapor Pressure of Iodine above Iron

ORNL has used this source only for systems operating near atmospheric pressure. However, adaption for higher pressure use should be straighforward. A schematic of the proposed high pressure source is shown in Figure 6.9. The high pressure modifications consist primarily of enclosing the cource inside a high-temperature, high pressure autoclave, and providing the valving necessary to allow isolation of the source from the loop. The present design utilizes an Autoclave Engineers autoclave, capable of operation at 700 °C and 8 MPa. The autoclave will be fitted with a seamless stainless steel liner to facilitate decontamination. The source will be provided with a fixed NaI detector to estimate the rate of iodine loss from the autoclave.

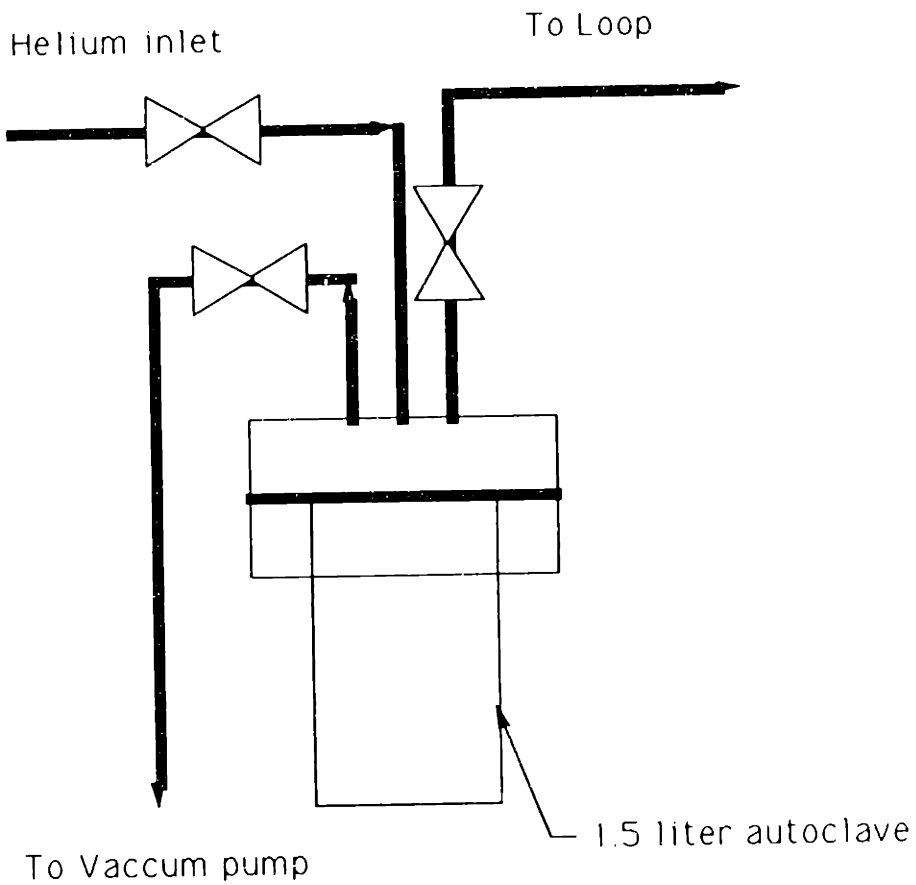

Figure 6.9
High Pressure Iodine Source (schematic)

6.5. Gamma Detection

The gamma detection systems will also be connected at the beginning of the next phase of the test program. The detector system will include three subsystems: the detector array consisting of NaI crystals, photomultiplier tubes, preamplifiers and a collimator; a mechanical positioning system; and the detector electronics. Of these, the first two have been engineered and tested during the scope of this work; the third will be implemented in a later stage of the project.

The radioactive isotopes used in the DABLE loop act primarily as tracers–there is no physical reason for the selection of radioactive isotopes over their stable counterparts save the ease of detection of very small quantities of the isotopes. For operational and safety reasons it is desirable to maintain the activity of the loop to the lowest practical level. This level is primarily determined by the efficiency of the detector system. More sophisticated and efficient detector systems reduce the total activity required, but are unfortunately, more expensive. The design problem then become achieving the maximum detector efficiency at a fixed cost.

6.5.1. Optimization of the detector geometry

The detector design must meet two opposing objectives–it must provide the maximum possible efficiency, and it must provide good axial resolution. The design space is defined by the need to provide an count rate high enough for good statistics while maintaining sufficient axial resolution to discern changes in deposition due to changes in the flow direction or wall temperature. For simplicity in the optimization of the detector geometry, consider a detector composed of a single cylindrical detector surrounding the pipe On each side of the detector is a collimator which serves to limit the field of view of the detector. Figure 6.10 gives the important dimensions of the proposed detector design. The three important dimensions for the analysis are the inner radius r_1, the shield inner radius r_s, and the axial length $2a$; the crystal outer radius can be considered sufficiently larger than r_1 that essentially all gammas striking the crystal are detected. This assumption holds for nearly all the isotopes of interest.

For a simple scoping model, consider the gamma source to be a line source aligned with the axis of the detector. The actual source is a uniform cylindrical source with radius r_0. This geometry will be incorporated into the final model, however, its treatment at this stage introduces unnecessary mathematical complexity. The two models give the same results when the ratio $\frac{r_1}{r_0}$ is large.

For the line source, consider the probability that a gamma emitted isotropically from a point located at distance x along the source will be intercepted by a detector with axial length $2a$, located at the origin. Plotting this probability as a function of distance from the detector center point gives the geometric efficiency or view factor of the detector for sources at various distances. This plot can then be used to define the limits between which some fraction, say 50%, of the detected gammas originate. These limits define the detector spatial resolution.

In the DABLE experiment we determined that an axial resolution on the order of 50 mm was appropriate. The choice of this figure was somewhat arbitrary, but is motivated by the size scale of the test section piping (28 mm Ø), and the resolution quoted in other experiments, such as the GA blowdown experiments, where the piping was cut into 2 inch (50.8 mm) lengths. A 50 mm resolution gives approximately 60 points over the length of the test section.

To determine the detector geometry necessary for a 50 mm axial resolution, consider the three regions of the x-axis shown in Figure 6.10. In region I, no gammas emitted reach the detector. In region II, only those gamma rays emitted into the solid angle bounded on one side by the inner edge of the left collimator and on the other side by the

right detector edge are detected. In region III, only those rays emitted into the solid angle subtended by the crystal are detected. The boundaries between the three regions are given in Table 6.3

Table 6.3
Regions in the detector model

Region	extent	defining equation
I	$\lvert x \rvert > \alpha$	$\alpha = \frac{2ar_s}{r_1 - r_s} + a$
II	$a < \lvert x \rvert < \alpha$	
III	$\lvert x \rvert < a$	

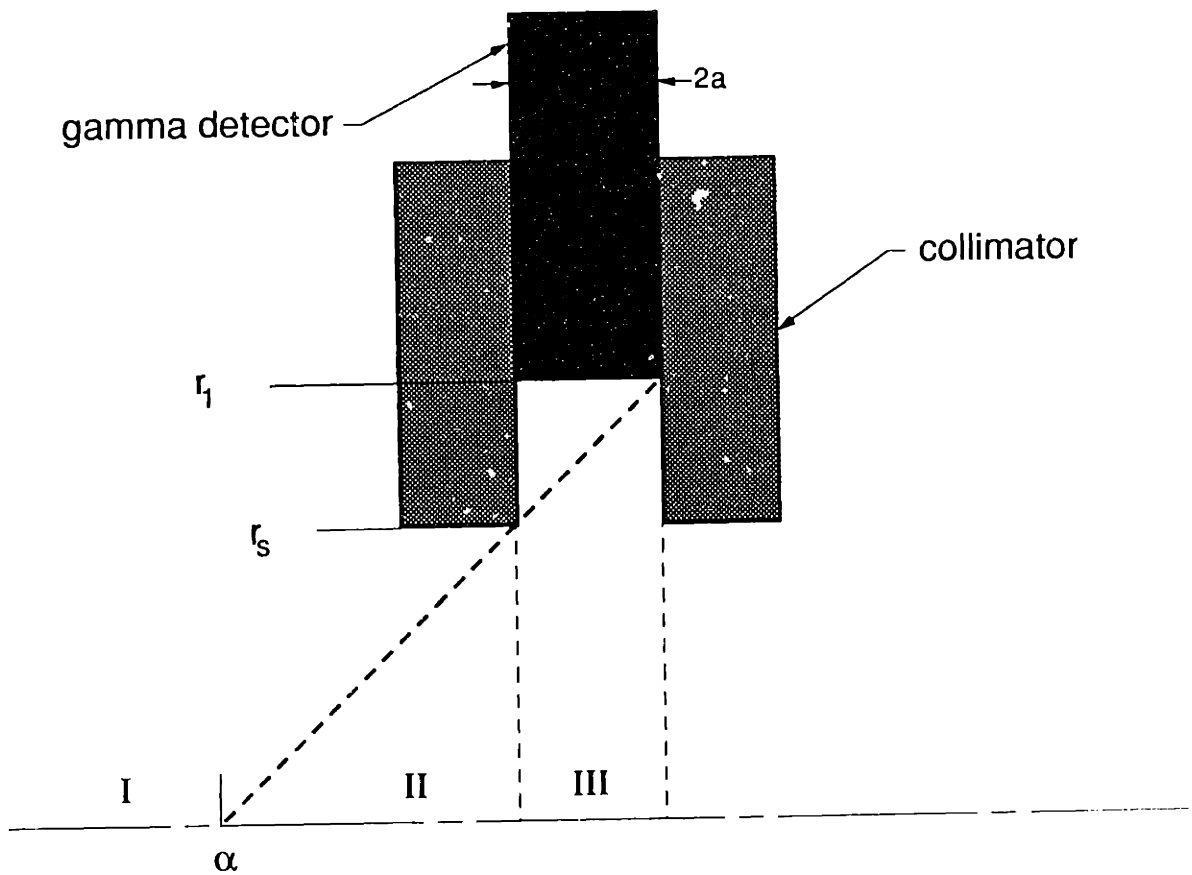

Figure 6.10
Detector Model

Inside each of these regions, the probability of a gamma ray impinging on the detector is simply the ratio of the solid angle between the angular limits θ_1 and θ_2 and the solid angle in an entire sphere (4π steradians). For a typical point in region II, labeled "A" in Figure 6.11, the two angles are given as

$$\theta_1 = \tan^{-1}\left(\frac{r_s}{x\text{-}a}\right) \text{ and}$$
$$\theta_2 = \tan^{-1}\left(\frac{r_1}{x+a}\right)$$

for a typical point in region III, labeled "B" in Figure 6.12, the two angles are given by

$$\theta_1 = \tan^{-1}\left(\frac{x}{r_1}\right) \text{ and}$$
$$\theta_2 = \tan^{-1}\left(\frac{x+a}{r_1}\right)$$

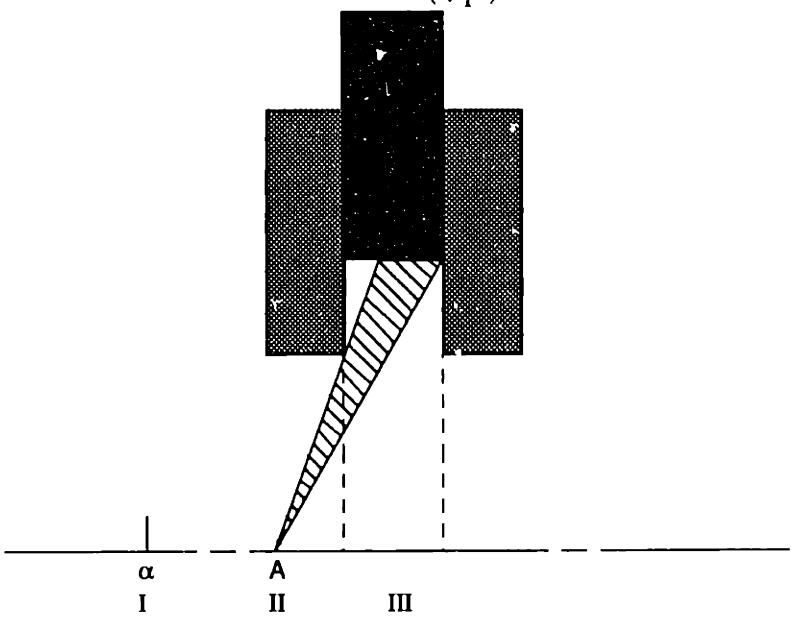

Figure 6.11
Solid angle for a source in region II

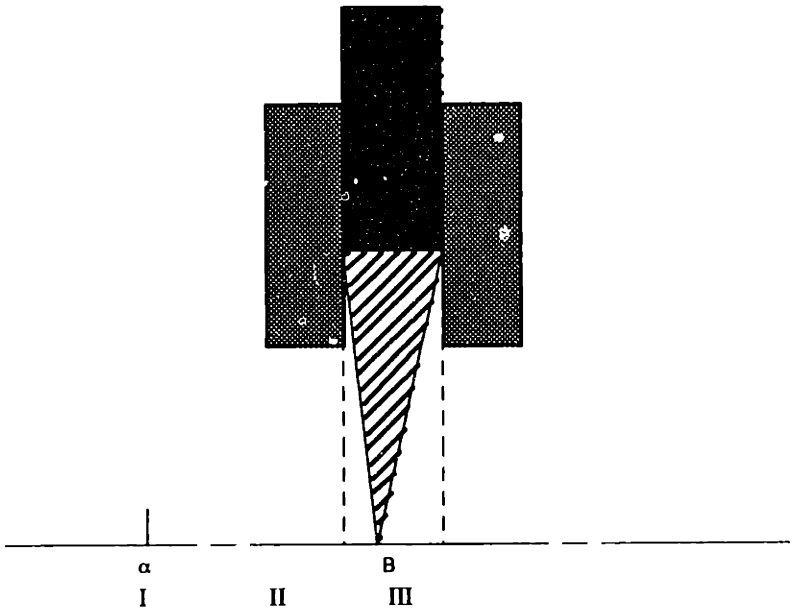

Figure 6.12
Solid angle for a source in region III

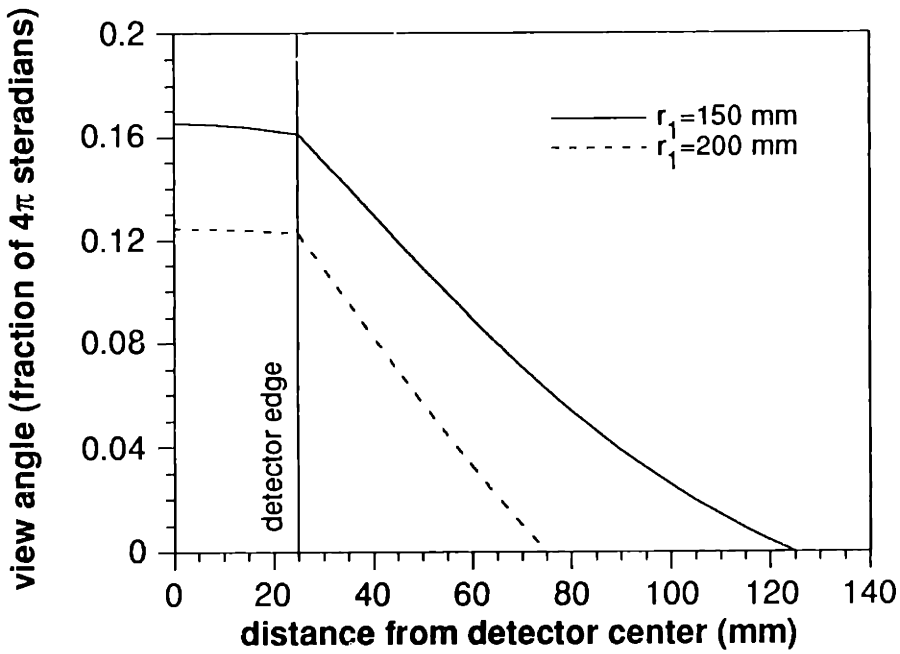

Figure 6.13
View factor for sources on the detector axis vs distance from detector center

Figure 6.13 gives numerical values for the view factor from a point on the axis of the detector as a function of distance from the detector center. These calculations were made for a detector with a collimator inner radius r_s = 100 mm and detector width $2a$ = 50 mm. Two curves are shown; the solid one is for a detector at 150 mm from the source, the other for a detector at 200 mm. For sources in region III (directly underneath the

detector), the sensitivity of the detector is relatively independent of the position of the source. In region II, (outside the detector), the sensitivity of the detector falls off nearly linearly to zero at some characteristic dimension α (given by equation in Table 6.3) away from the detector center.

The figure also illustrates the tradeoffs in positioning the detector. For a fixed collimator inner radius, the overall efficiency of the detector drops as the crystals are moved away from the pipe, while the spatial resolution of the system improves.

To this point in the discussion, the detector geometry has been assumed to be a complete cylinder surrounding the pipe. This was the original design suggested by the 22.033 class. Bhavya Lal, of the MIT Nuclear Engineering department investigated the feasibility of this detector design, and determined that while possible, it was not an economically viable solution. The decision was then made to replace the cylindrical, one-piece NaI crystal with several 2" individual cylindrical detectors arranged radially around the pipe. The discussions of the view factor given in the previous paragraphs still hold, with the addition of a factor relating the area of the individual crystals to the area of the single crystals. For N crystals of radius a, positioned at radius r_1 from the pipe centerline, this factor is

$$f = \frac{\pi a^2 N}{2\pi r_1 a}$$

For the example given in Figure 6.10, with the detectors at 150 mm from the pipe centerline, the maximum view factor is ~0.16. For four detectors, f = 0.33, yielding a maximum view factor of 0.056. This means no more than 5.6% of the gammas emmitted from the pipe strike the detector. Only a fraction of those will be detected.

6.5.2. Selection of the isotopes

E. Love investigated the selection of isotopes for the DABLE project [L2]. He determined the most promising isotopes to be used as tracers in the experiment to be $^{110m}_{47}Ag$, $^{126}_{53}I$, $^{131}_{53}I$,and $^{134}_{55}Cs$. The decay characteristics of these isotopes are shown in

Table 6.4

Table 6.4
Isotopes considered for use in deposition experiments

Isotope	$T_{1/2}$	Decay Mode	Gamma Energies (MeV)
$^{110m}_{47}Ag$	253 d	β^-, IT	.658, .83
$^{126}_{53}I$	13 d	β^+, EC, β^-	.39, .67
$^{131}_{53}I$	8.07 d	β^-	.364
$^{134}_{55}Cs$	2.05 y	β^-	.662

In addition to selecting isotopes, Love also verified some key assumptions of the original design, among them assumptions regarding the efficiency of the NaI detectors proposed. His studies, combined with the present work, suggest that the detection system will show an absolute efficiency in the range of 0.1 – 1%.

6.5.3. Prediction of detector system performance

Considering typical surface activities measured in in-pile and out-of-pile experiments to be in the range of 10 nCi/cm^2 ($\approx 4 \times 10^6$ Bq/m^2), we can estimate the time required to acquire, say, 1000 counts at a given axial position along the test section. The total counts acquired in a given time is given as

$$C = \eta_{abs} \sigma A t$$

where

C	total counts
η_{abs}	absolute detection efficiency
σ	surface activity [Bq/m^2]
A	area viewed by detector [m^2]

and η_{abs} is given by

$$\eta_{abs} = f_{geom} f_{atten} \eta_{detect}$$

where f_{geom} is the average value of the geometric view factor over the viewing area, and f_{atten} accounts for the attenuation of gammas as they pass through the pipe walls and the insulation. For the detector as designed, the absolute detection efficiency is approximately 0.2%. Performing the calculations for a 4 MBq/m^2 source density, and a 0.2 m wide viewing area yields a count rate of 127 counts/sec, or approximately 8 seconds per measurement point needed to give 1000 counts. With 60 measurement points along the test section, a full scan of the test section would require 8 minutes. This is a reasonable value, considering the expected test duration of a few hundred hours. Slower scans give better counting statistics and spatial resolution of the deposition profile, faster ones will better resolve the time history of the deposition process.

In the current design, the detector radial distance is variable, and will be optimized in a later phase of the project. The allowed limits yield a resolution (defined as that area containing 50% of the detected counts) of approximately 80 mm width. This is a slightly lower resolution than the design goal, primarily because of thermal limitations on the detectors and the trade-off with adequate absolute efficiency.

The resolution could be enhanced in practice by proper post-processing of the data. Consider the following analysis, borrowed from the language of digital signal processing. Sample the detector response function at (say) 10 mm intervals and call this sampled respose function r_k. Then if we move the detector along the track in intervals of 10 mm, the output at each point j along its travel is given by

$$(r * s)_j = \sum_{k=-M/2+1}^{M/2} s_{j-k} r_k$$

where

s is the true count rate as a function of position (the source), and

M is the width of the detector response function.

This is simply the definition of the discrete convolution of the functions s_j and r_k. A more familiar analogy may be from image processing where s would be the image, r the "blurring filter", and $(r*s)_j$ the blurred image. At this point, we make use of the discrete convolution theorem[P2]:

> *If a signal s_j is periodic with period N, so that it is completely determined by the N values $s_0,...s_n$, then its discrete convolution with a response function of finite duration N is a member of the discrete Fourier transform pair*

$$\sum_{k=-M/2+1}^{M/2} s_{j-k} r_k \Leftrightarrow S_n R_n$$

here S_n and R_n denote the discrete Fourier transforms of the signal and response functions. Now, the problem of determining the true source function s_j becomes simple to solve. We begin by taking the discrete Fourier transforms of the sampled data (the convolution of the source and the response), and the response function. Dividing the two gives the transform of the source data. Inverting the transform gives the source data itself. As long as the response function is narrower than the source, for *continuous* source and response functions in the absence of noise, this process will recover the original data exactly, regardless of the dtector width. In practical use, the accuracy is limited by the noise and the accuracy to which the response function is represented. Nonetheless, this

method promises to significantly increase the potential spatial resolution of the detector system.

6.5.4. Detector Mechanical Systems

The detector array, consisting of the two collimators and the four NaI crystals, is mounted on a linear bearing system positioned just under the test section. The linear bearing system consists of two 10 mm dia. polished steel rods mounted parallel to each other on 20mm centers. The rails are supported by a 130 mm wide aluminum channel, 3 meters long. On the rails rides a 100 x 100 mm aluminum cart with two linear bearings, these bearings contain recirculating balls which provide a low friction sliding motion along the rails. The collimators are mounted on top of this cart by screws extending into threaded inserts inside the lead. The cart is driven up and down the track with a timing belt and stepper motor. The stepper motor is mounted just below the right end of the channel. The timing belt passes over toothed pulleys mounted in journal bearings at each end of the channel, and is tensioned by a third pulley on a hinged plate. The stepper motor is a Compumotor model PK2. capable of 400 steps/revolution. With the 50 mm diameter pulley used on the motor, this translates into 0.4 mm/step. Hysteresis in the timing belt drive was measured to be 1.5 mm, so the system should be capable of positioning the detectors with an absolute accuracy of less than 1.9 mm, and a relative accuracy displacement accuracy for points in than same direction of motion of ±0.2 mm. These accuracies are far better than required by the spatial resolution of the gamma detectors.

The NaI detector crystals are mounted between two lead collimators. The collimators are lead discs, 100 mm ID and 250 mm OD, 50 mm thick. The collimators are split along a diameter to allow them to be placed around the test section. Mounted to one disk are four PVC pipe sections, extending radially outward from the ID of the disc. The NaI gamma detectors slide into these tubes and are held by set screws in the tube walls.

6.6. Safety

The DABLE facility presents a number of safety hazards which must be dealt with in the design. The system includes a hot, high pressure suffocating gas with radioactive contaminants. High voltage and high temperatures are present in the heaters. The primary hazard to be dealt with is the possibility of release of radioactive isotopes from the loop exposing the loop operators or the public. The isotopes of interest to the DABLE loop are by no means innocuous; indeed, we are interested in their behavior because they represent the most biologically hazardous of the potential releases during an accident. This lays a particular burden on the the safety systems in the loop.

Nonetheless, an adequate level of safety can be maintained through proper design and operation.

The DABLE loop is completely enclosed in a large lexan and particle-board box, which is conventionally refered to as the "hot-cell", although a more accurate term would be a chemical hood. The hot-cell has five openings, three of which are normally closed. The other two form the inlet and outlet for a continuous air purge through the cell. One of the two normally open ports surrounds the pressure vessel. The back of the pressure vessel and its cradle project through the left wall of the cell. This opening is the normal air inlet to the cell. Air flowing through this opening serves a dual purpose–it both purges the cell of any radioactive compounds present in the cell atmosphere, and helps remove heat from the back of the vessel. The air is drawn through the cell by a roof mounted exhaust fan. The fan is connected to the top of the cell by a short rectangular duct, approximately 300x200 mm in cross section. Inside the duct, particulate and charcoal filters serve to control the release of radioactive particles from the system. Discussions with the MIT Industrial Hygiene and Environmental Health Services indicate that this system should be able the safely absorb a complete release of the approximately 10 mCi of iodine present in the loop at a given time. The filters will be periodically counted to determine the rate of iodine release from the system.

The three other openings in the cell are a personnel access door on the right side of the front wall of the cell, a air inlet at the top of the cell, and a overpressurization relief door on the top of the cell. The personnel access door is a square door, approximate 1 meter on a side, affixed to the outside of the cell by eight thumbscrews. The door seals against a closed-pore weatherstripping, making a leak-tight seal. The air inlet on the top of the cell could be used to provide an alternate inlet for the cell air. A fan mounted inside the room draws air from the roof and forces it into the cell through this inlet. This inlet is not currently in use. The finally normally closed opening in the cell is a pressure relief for the cell as a whole. In the event of a catastophic failure of the loop piping, this simple hinged vent would open if the cell pressure exceeded the 175 Pa design pressure of the cell.

In addition to the radiation hazards, there are the normal hazards associated with the operation of any high-temperature, high-pressure system. Overpressure protection for the loop is provided by an adjustable relief valve. This valve vents through a 6.25 mm diameter line directly to the exhaust stack, minimizing contamination of the cell itself. The heater sizing is such that even with all the heaters in operation, the loop cannot reach temperatures high enough to fail the piping. The pressure vessel has been proof tested to 10.5 MPa, well beyond the maximum expected loop operating pressure.

Perhaps the most likely hazard during normal operation of the loop is to develop hot spots underneath one of the heater wires and fail the insulation. A failure of this type would connect the entire loop, including the pressure vessel, to the hot side of the electrical system. Due to the high currents present in the heaters during normal operation, it may not be possible to protect against this failure with conventional circuit breakers. For this reason, all the heaters on the loop are protected by ground fault interrupters. In the initial stages of the heater testing these interrupters proved their worth when errors in installation allowed heater power leads to contact the pipe.

In addition to maintaining safety for the personnel and public, the loop will incorporate a number of active safety systems designed to protect the facility and data integrity. Among these will be active heater shutdowns on local over temperature conditions, and controlled data acquisition system shutdowns on power failures. The data acquisition and control computer will be operate from a uninterruptible power supply capable of providing power for approximately five minutes after a power failure. If power is not restored after three minutes of the interruption, a controlled shutdown sequence will be initiated.

6.7. Data Acquisition and Control Software

Essentially all the data acquisition and control of the loop operation passes through the computerized control system. As part of the development of each system in the loop, software was written to integrate the system into an overall loop model.

The data acquisition and control computer for the DABLE loop is a Apple Macintosh II computer with a 68020 processor running at 16 MHz and a 68881 floating point coprocessor. Mass storage is on a 105 Megabyte hard disk, with additional storage and back-up on 45 Meg removable hard disk cartridges. Data is acquired from any of three sources: a multi-purpose data acquisition card, a GPIB interface card, or a via RS-232/RS-422 ports. The general purpose data acquisition card is a National Instruments NB-MIO-16L-25. The card provides 16 single-ended analog input lines with bipolar or unipolar input ranges of 5 or 10 volts at 12 bit resolution. In addition to the analog inputs there are two analog outputs, three counter/timer channels and a four bit wide digital I/O port. The 16 analog inputs are expanded to 64 by a AMUX-64 multiplexer board, also by National Instruments. The GPIB card is a National Instruments model NB-GPIB, providing an IEEE-488 standard port . The RS232/RS422 ports are provided by a Creative Solutions Hurdler HQS quad port serial board.

Software for data acquisition and control was written in Think™ C 4.0. Think C 4.0 is a object-oriented C, a subset of the C++ language. The choice of this programming

environment was motivated by several factors–it is a well established and robust compiler, it turn-around time is very fast, and it has an exceptional source-level debugger. But most importantly, it includes several megabytes of classes implementing the complete Macintosh user interface. This class library provided a solid building ground for the loop controller.

The choice of an object-oriented language had additional benefits. By implementing each of the loop subsystems as a separate object, a close mapping between the physical loop and the program structure. Instead of physical components connected by wires and pipes, the controller has objects connected by message-passing. Take for example the circulator motor drive. The drive has state (speed, acceleration parameters, etc stored in its memory), and responds to various command sequences, such as "accelerate to 15,000 rpm" or "stop". In the controller, an object is created corresponding to the motor driver, with the same local state parameters and the ability to send and receive messages from other parts of the program or the drive itself. This close mapping of physical devices to programming abstractions facilitates the design and maintenance of the program. The message-passing programming style also insulates changes in the internal implementation of the object from the rest of the program. For example, a complete swap of the motor and drive unit necessitated changes only to the implementation of the driver object–the messages by which it communicated with the rest of the program remained the same.

Two programs are used to control the loop. The first is the main loop controller, which integrates measurement and control of temperature, pressure, flow rate and circulator rpm. The second is the controller for the gas analyzer, which both controls the RGA, acquires scans and performs analysis of the scans to determine the partial pressure of each of the gas impurities. Each of these incorporates a graphical interface which simplifies the operation of the instruments and clarifies the important data trends.

Figure 6.14 shows some parts of the graphical interface.

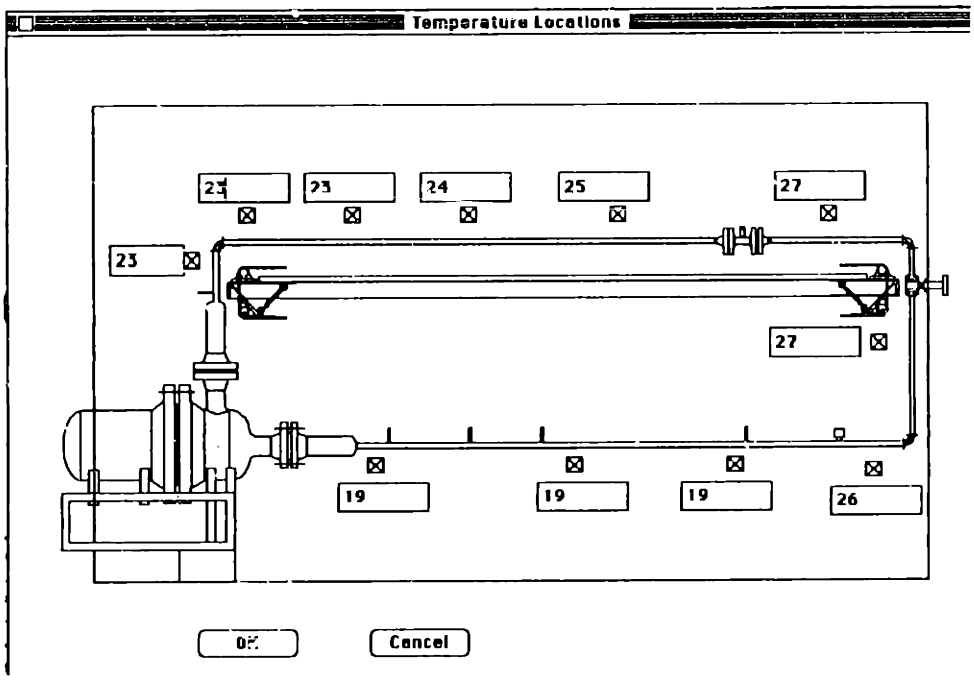

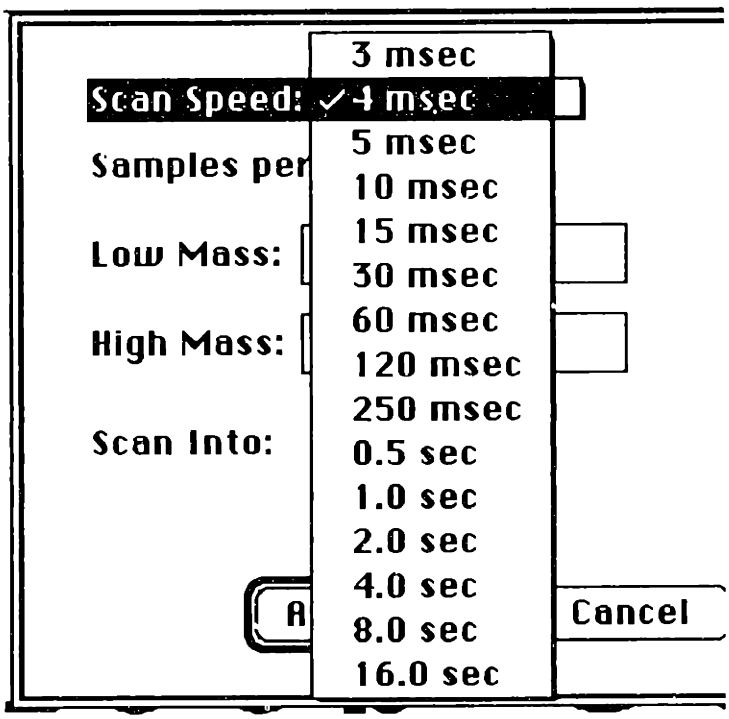

Figure 6.14
Interface to the Controller Code

Chapter 7

SOME EXPERIMENTAL RESULTS

7.1 Shakedown testing

Although full commisioning of the DABLE facility has been delayed by unanticipated funding problems, a number of key demonstrations of the loop's capabilities have been completed. In the original plan for the project, it was intended that the first phase of the project would end with the completion of the first deposition study. Changing priorities and delays in the construction of the facility have forced a scaling back of these plans. Nonetheless, the experimental work to date demonstrates the capabilities of the facility, and lays the groundwork for future studies.

7.1.1 Circulator map

The most important of the experimental work to date has been the demonstration of the loop's capability to circulate helium at temperatures up to 300°C, pressures to 5.2 MPa, and flow velocities in a 2.5 cm diameter pipe between 0 and 20 m/s. These conditions have been achieved while operating the loop in a near-isothermal condition. Higher pressures and temperatures could be achieved with only minor modifications to the loop. This work clearly demonstrates the ability of the loop to maintain conditions in the test section comparable to those found in MGR steam generators or recuperators, while simultaneously varying the flow rate in order to investigate deposition and lift-off phenomena.

While the loop as currently configured (with the exception of the circulator motor), is capable of indefinite operation at 230°C and 6.3 MPa, almost all of the tests on the ciruclator were performed at lower temperatures and pressures. There were several reasons why this course was selected–the primary being that the testing of the circulator involved repeated assembly and disassembly of the pressure vessel, and operation at lower loop pressure minimized helium consumption. In addition, some components of the loop limited the maximum temperature and pressure. The most important of these was the turbine flow meter, which was not rated for continuous use above 230°C. The turbine flow meter is connected to the test section by two 1" 600 lb flanges and can be easily replaced by

a dummy section to increase the operating temperature limit of the loop. This swap was not made in the course of the circulator testing, since the turbine flow meter is needed to measure the circulator performance map.

The primary goals of the circulator testing program were 1) demonstrate the operability of the circulator 2) map the performance of the device over the widest possible range, 3) demonstrate the ability to maintain flow conditions envisioned for the first series of iodine deposition tests, and 4) gather information to be used in later designs. All of these goals were accomplished successfully, although as will be detailed later, certain elements in the current design will need to be modified to give good long-term performance of the circulator.

The most important characterstics of the circulator/loop system are given in the form of a circulator performance map. This map shows the circulator pressure rise and flow rate. Together with a knowledge of the system resistance, the map defines the operating point of the circulator as a function of the motor rpm. Each point on the map is characterised by three values–the pressure rise accross the circulator, the flow rate, and the circulator rotational speed. This data is acquired by three instruments–a optical tachometer, a differential pressure gauge, and a turbine flow meter.

The performance data in this section were taken using a universal motor as a drive system. The initial choice of the switched reluctance drive was driven primarily by budgetary constraints. The delay in replacing the motor was the result of a funding cut-off, hence the use of the universal motor for these tests. This motor was intended to be used on a temporary basis only, while the replacement for the failed switched reluctance drive was manufactured. As a temporary system, it had a number of limitations which reduced the accuracy and reproducibility of the measurements. The most important of these is that the motor lacks closed-loop control. The motor speed was measured by an optical tachometer reading a reflective tape placed on the shaft. The output of this sensor was converted from frequency to voltage by a Cole Parmer model 8212 tachometer, then digitized with the DA board. Motor speed control was by manual adjustment of a variable voltage power supply. Since the speed control was open loop, some variation in speed was experienced as the loop resistance and the aerodynamic loading on the impeller changed. In a typical run, when the flow was varied from 5 to 15 m/s at a nominal 12,000 rpm, the speed varied ± 150 rpm around the nominal value.

The optical tachometer caused some problems of its own. Alignment was critical, and after several hours of operation, the sensor tended to move in its mounting fixture due to motor vibration. A more severe problem was the pressure limitation imposed by the

incandescent light bulb in the sensor, which could implode at pressures above 5 MPa. The failure of this unit forced the early termination of some tests.

The circulator pressure rise in these tests was measured by two total pressure probes. These probes were mounted in the main loop piping just outside the inlet and outlet nozzles. The differential pressure between the probes was measured by a differential pressure gauge. This gauge has a maximum linear differential pressure range of 0-4.8 kPa, although if a 10% error may be tolerated, the range can be extended to 7 kPa. This range was insufficient to cover the entire operating envelope of the loop at any density greater than 2.3 kg/m^3 (3 MPa @ 350°C typical), so the pressure rise measurements at the highest pressures and flow rates necessarily involve some extrapolations.

The flow rate in these tests was measured by the turbine flow meter. The arrangement of the loop does not allow the pitot tube and the circulator pressure rise probes to be read simultaneously (both are connected to the same ΔP gauge). Before each run, a calibration curve was taken where the turbine flow meter and the pitot tube were read simultaneously as the circulator rpm was varied. Figure 7.1 is a typical example of the data gathered in these tests.[1] The error bars represent a 10% uncertainty in the gas density. As can be seen from this graph, the pitot tube and the turbine flow meter do not yield identical measurements of the flow rate. Over a wide range of conditions, the ratio of the velocity inferred from the pitot tube measurements to that read by the turbine flow meter remained in the range of 1.1-1.2. Figure 7.2 shows this ratio for the same data as in the previous figure. A substantial amount of work was put into resolving this discrepancy, but no definitive conclusion was reached. The turbine flow meter cannot be easily calibrated using helium in our lab; we plan to have it re-calibrated by the manufacturer. This recalibration had not been performed at the time of this writing, so the difference remains somewhat of a mystery. A number of hypotheses regarding the difference were advanced, tested and ultimately rejected. Further details are presented in Appendix 2.

The turbine flow meter has a very good time response; it can track changes in the flow of up to 0.5 (m/s)/s with good accuracy. The pitot tube has a somewhat longer time scale, as can be seen in Figure 7.3, where a hysteresis is observed when the flow was ramped up rather slowly, then reduced at 0.42 (m/s)/s. In later testing, the rate of change of the circulator rpm was limited to avoid this efffect.

The structure of a circulator map is shown in Figure 7.4. The *y* axis gives the ratio of pressure rise to density in J/kg, and the *x* axis gives the flow rate in m/s. The map shows the constant rpm lines, a typical system curve, the design point and the contours of contsant

[1]only a portion of the data points are shown for clarity

efficiency. At any given circulator rpm, the flow rate and pressure rise of the system are determined uniquely by the intersection of the system curve, and the constant rpm curve. The system curves are parabolic in shape, characterised by the constant k in the expression

$$\Delta P = k\frac{\rho v^2}{2}$$

The curves of constant rpm are approximately parabolic for the impeller used in our experiments. For an optimum design, the design rpm curve and the design flow rate intersect at the design point. If the efficiency of the circulator or the system resistance are wrongly estimated, a different circulator speed will be required to achieve the design flow conditions.

In practice, the map is constructed as follows. The "open" system resistance curve is obtained by ramping the circulator speed slowly from ~4000 rpm to the maximum stable circulator speed. Pressure rise, flow rate and circulator speed data are taken once every 3 to 6 seconds during this ramp. The curves of constant rpm are approximated by curves of constant drive motor voltage by setting the voltage on the circulator to give the required rpm. Then a ball valve is slowly closed, increasing the system resistance and sweeping the constant rpm curve from right to left. This procedure is repeated at a number of different rpm to determine the circulator map.

As mentioned previously, the curves of constant rpm in these plots were approximated by curves of constant drive motor voltage. The accuracy of this approximation can be judged from Figure 7.5, which shows the time history of both the circulator rpm and the flow rate while the valve was being closed. The circulator speed varies around the nominal 13,400 rpm by only ±150 rpm while the flow velocity varies from 21 to 5 m/s. Below 5 m/s, the circulator rpm rises by approximately 900 rpm, or 6.7%.

The next three figures show experimental measurements of the circulator performance. The three plots represent the performance data at successively higher temperatures and pressures. The curves were taken in different experimental runs, and the circulator was disassembled between runs, so there may be some effect, primarily variation in clearance losses, between the three plots. Nonetheless certain trends can be observed. The second two plots both show better performance than the first, an effect believed to be a combination of lower pressure in the system and a larger impeller/shroud spacing during the first test. The data from the highest temperature and pressure test are limited due to the maximum pressure rise which could be read by the ΔP gauge, but complete flow information was obtained to 15,000 rpm. This plot shows very similar, but slightly better performance than the intermediate condition data of Figure 7.7.

The loop flow rate at constant rpm was observed to be a function of pressure for pressures below ~1.5 MPa. This effect can be seen qualitatively in Figure 7.9, where the measured flow velocity is plotted as a function of loop pressure. This data was taken by operating the circulator at a constant voltage while increasing the system pressure. It is not clear whether this is a real effect or an artifact of the instrument's non-linearity at low flow rates. Above 1.5 MPa, the flow rate is not a function of pressure, as expected. Figure 7.10 quantifies these observations with fits to the flow rate vs rpm data taken at both high and low pressures and temperatures.

Figure 7.11 shows the relationship between the circulator speed and the flow rate at 5.34 MPa and 290°C. This data was used along with that from Figures 7.7 and 7.8 to extrapolate the performance of the circulator at the conditions planned for the iodine tests (6 MPa, 350°C). This is a very small extrapolation, since the densities at the two conditions are nearly identical. The resulting predicted map is shown in Figure 7.12. The curves for cirulator speeds of up to 12,000 rpm are based on fitting parabolas to the measured data. Above 12,000 rpm, complete data on the pressure rise is not available. Instead, the curves were constructed as follows. The open system curve was extrapolated based on data taken at 3.5 and 5.3 MPa. Then Figure 7.11 was used to determine the open system flow rate at a given rpm. Then, based on the curve fits of the constant rpm curves at lower speeds, parabolas extending from the open system operating points were constructed. The quality of this extrapolation degrades with distance from the open system curve, so only a portion of each of the lines is shown.

During the course of the circulator testing, the heaters were operated at temperatures of up to 300°C. These temperatures could be achieved with only six of the seven heater sections operating, and incomplete thermal insulation. The heater design has proved workable, with the only faults occuring early in the course of testing when thermal expansion shorted some poorly insulated leads to the main heater section. After these were replaced, no further problems were encountered. The heater performance seems to be adequate for testing at temperatures up to ~450-500°C. Above this temperature, it may be necessary to heat certain unheated sections of the loop in order to provide additional power. At 300°C, the steady state loop thermal power requirement is approximately 3 kW.

To summarize, flows in the range required for a wide range of deposition and lift-off tests have been achieved in the loop. This has been accomplished using an off-the-shelf, unsophisticated circulator drive. We expect the performance to improve with the installation of the DC drive, a new shaft and gas bearings.

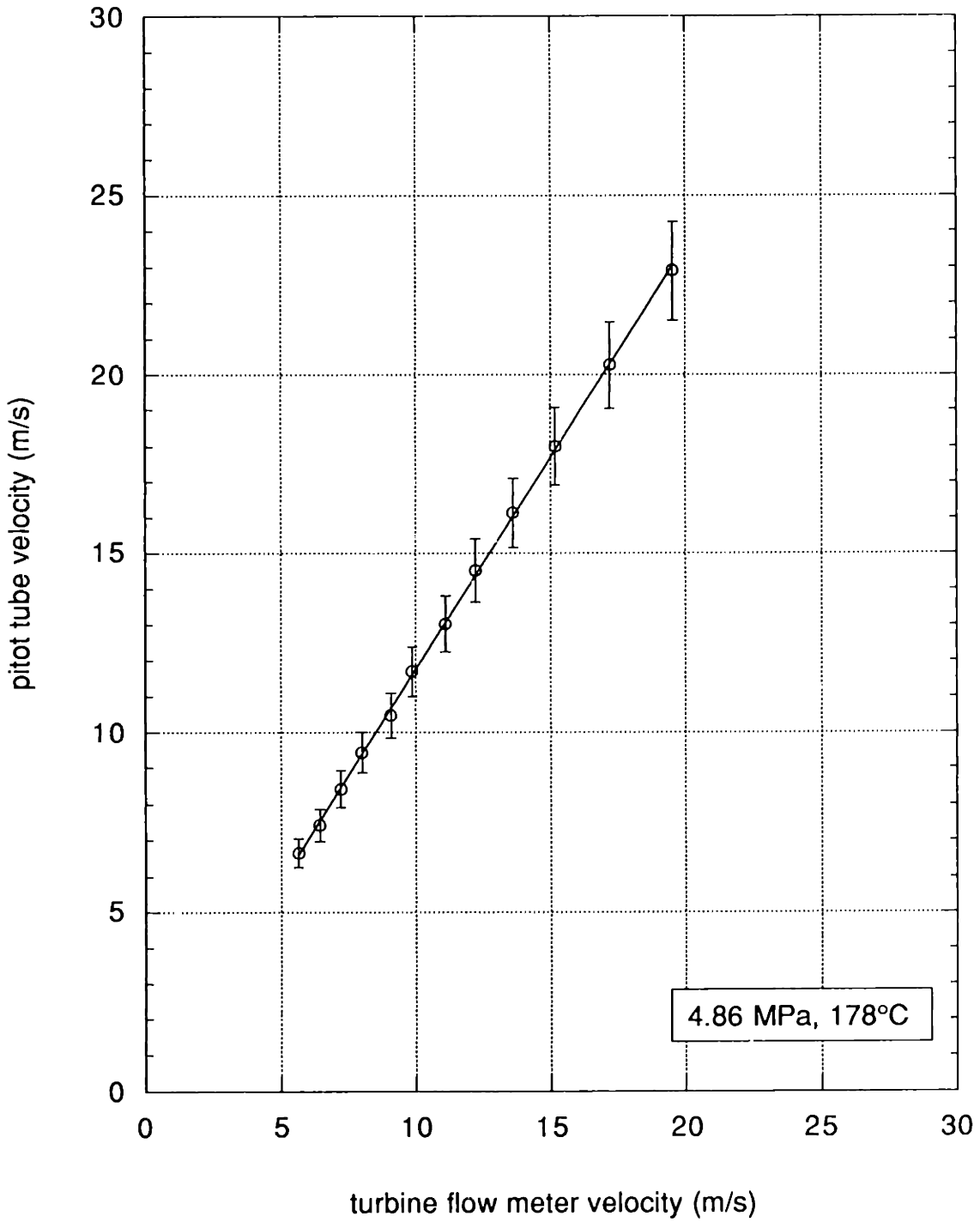

Figure 7.1

Pitot tube and turbine flow meter readings

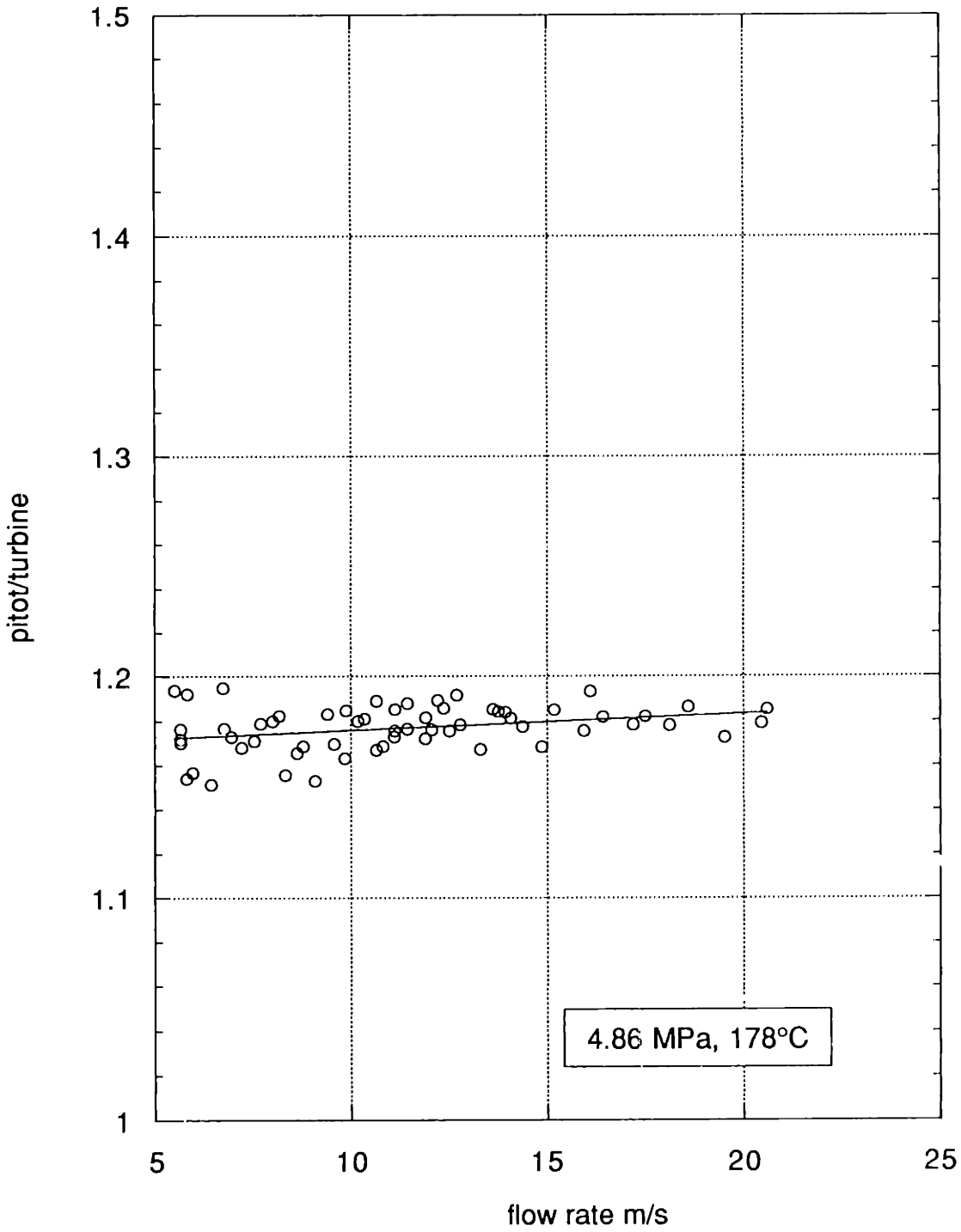

Figure 7.2

Ratio of pitot tube to turbine flow meter measured velocity

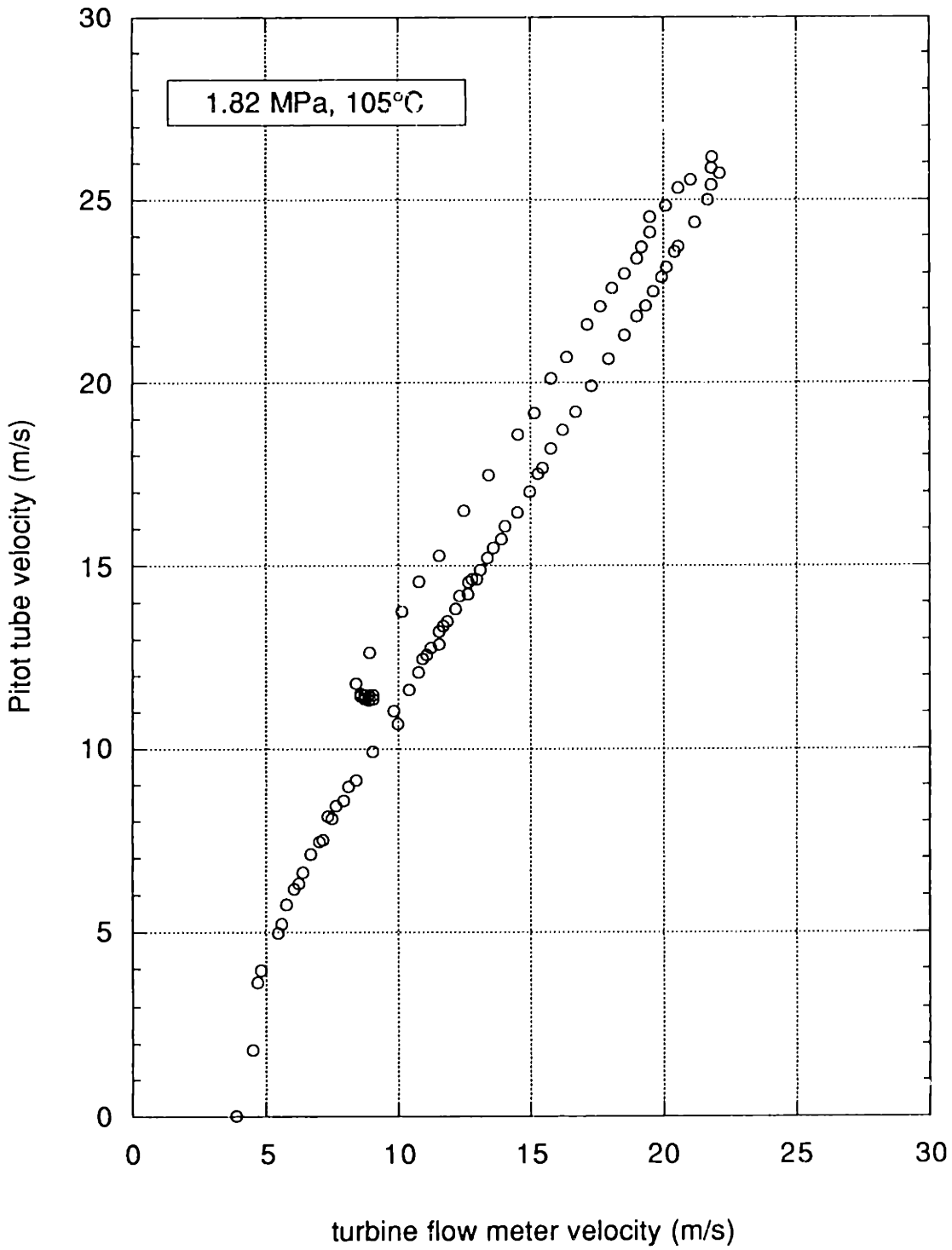

Figure 7.3

Hysteresis in the pitot tube readings

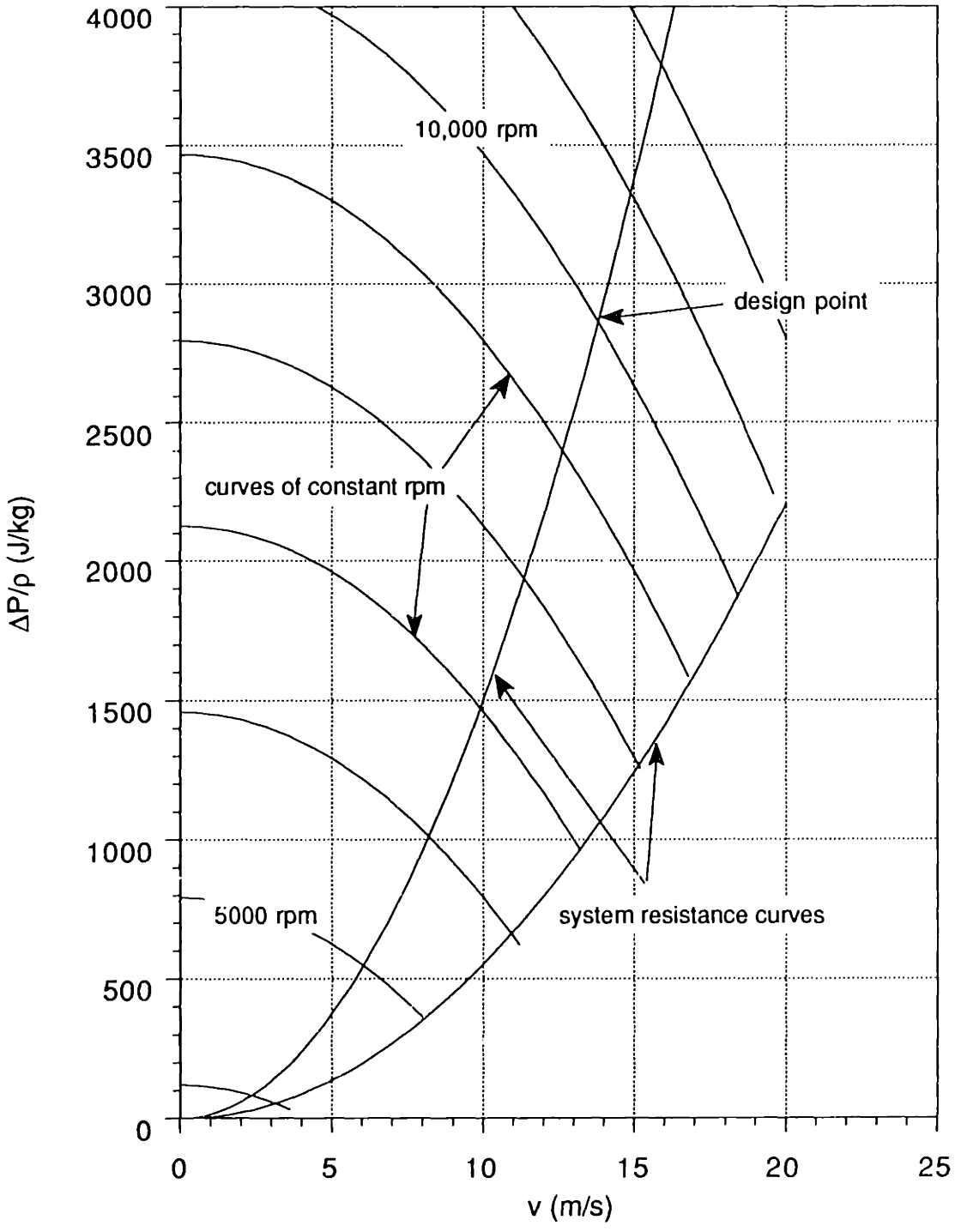

Figure 7.4

Example Circulator Map

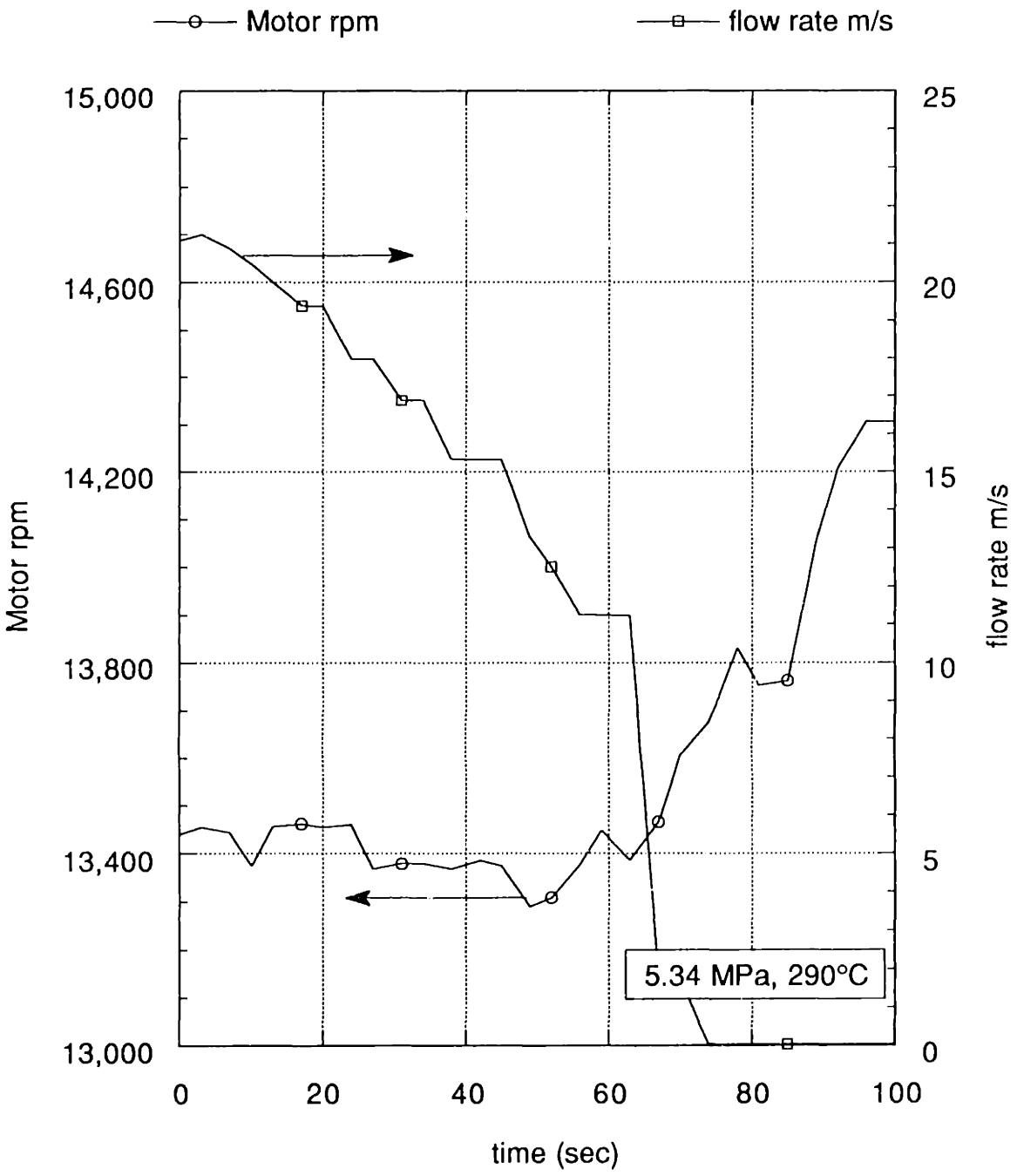

Figure 7.5
Variation of rpm at constant voltage

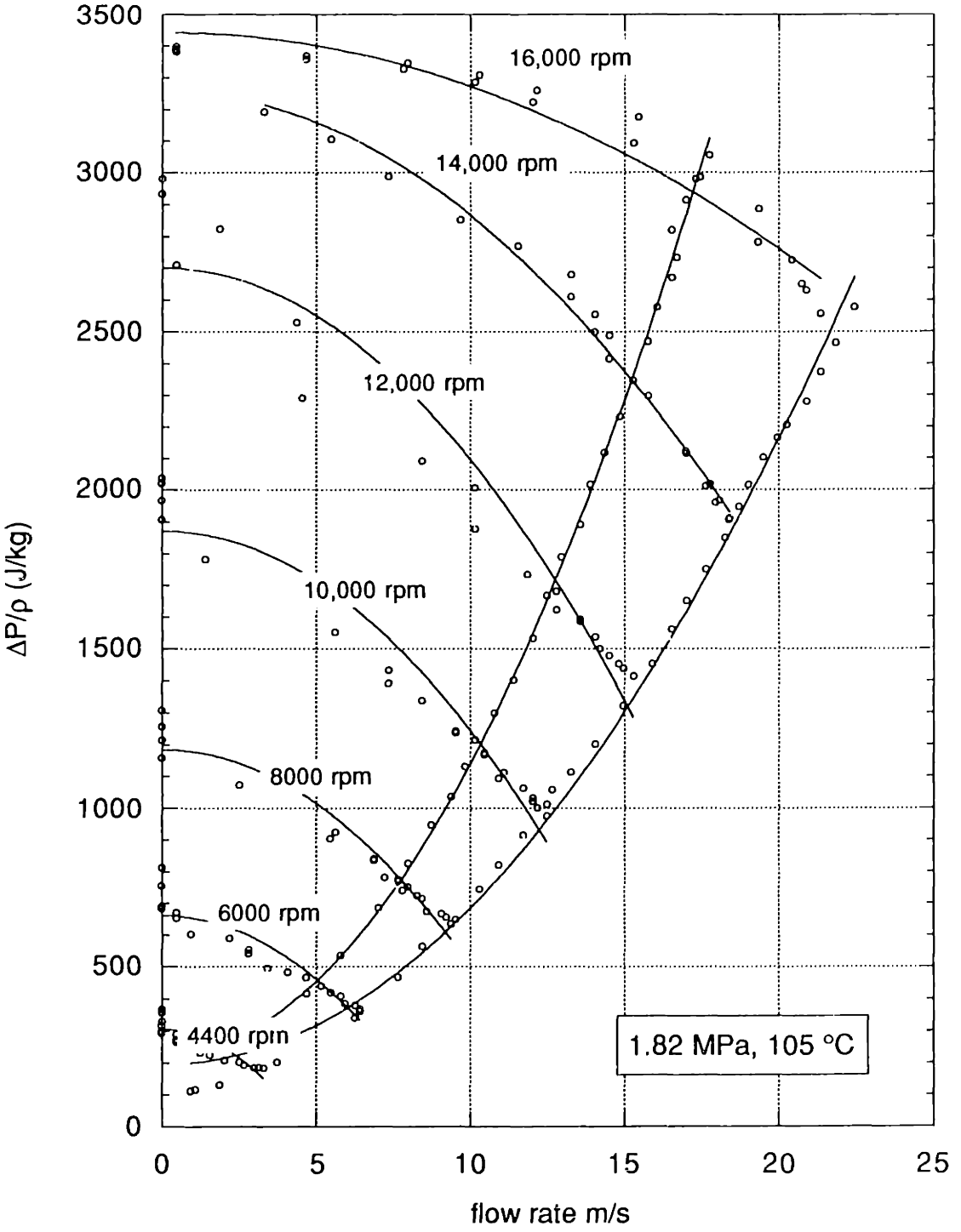

Figure 7.6
Circulator Map at 1.82 MPa, 105°C

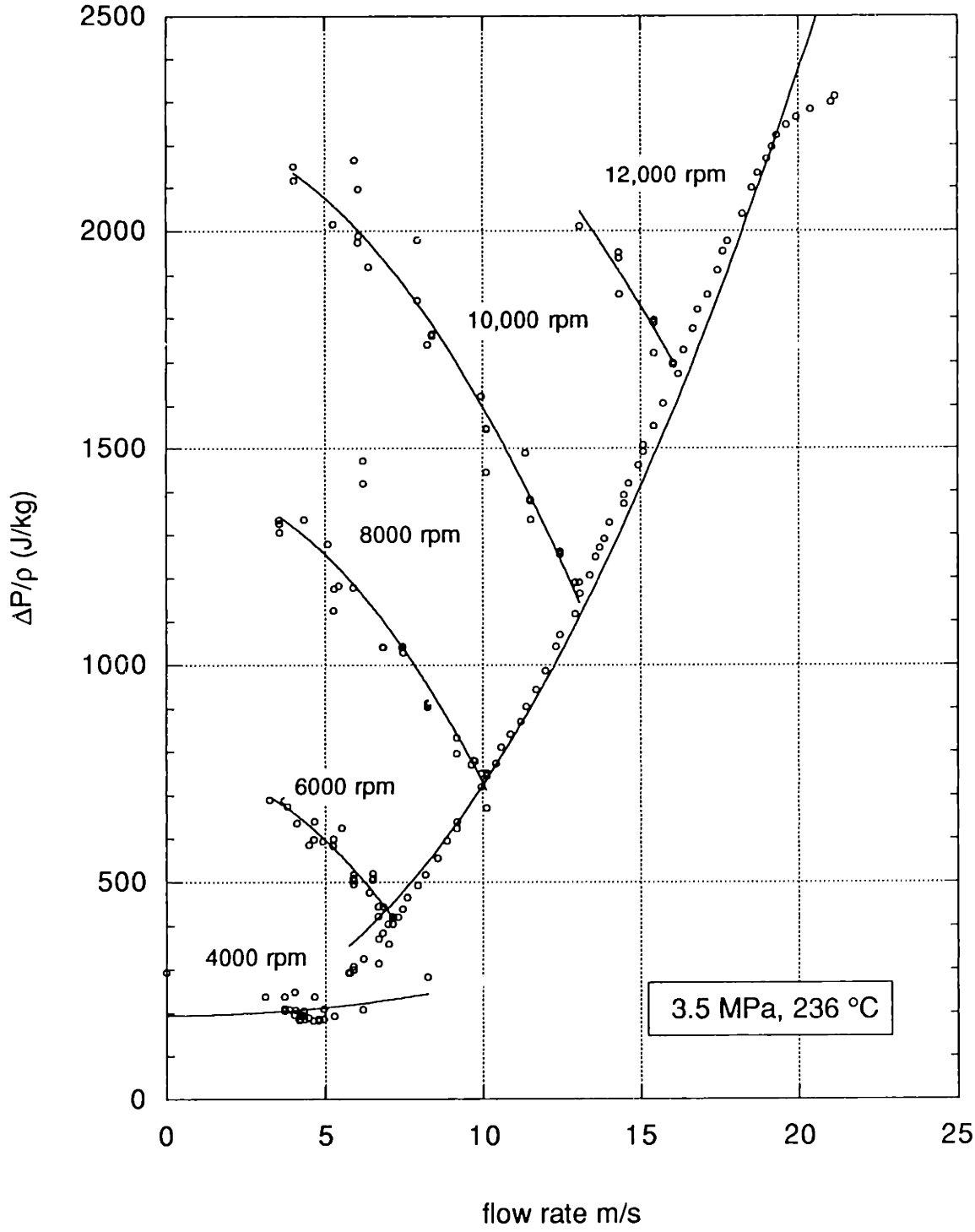

Figure 7.7
Circulator Map at 3.5 MPa, 236°C

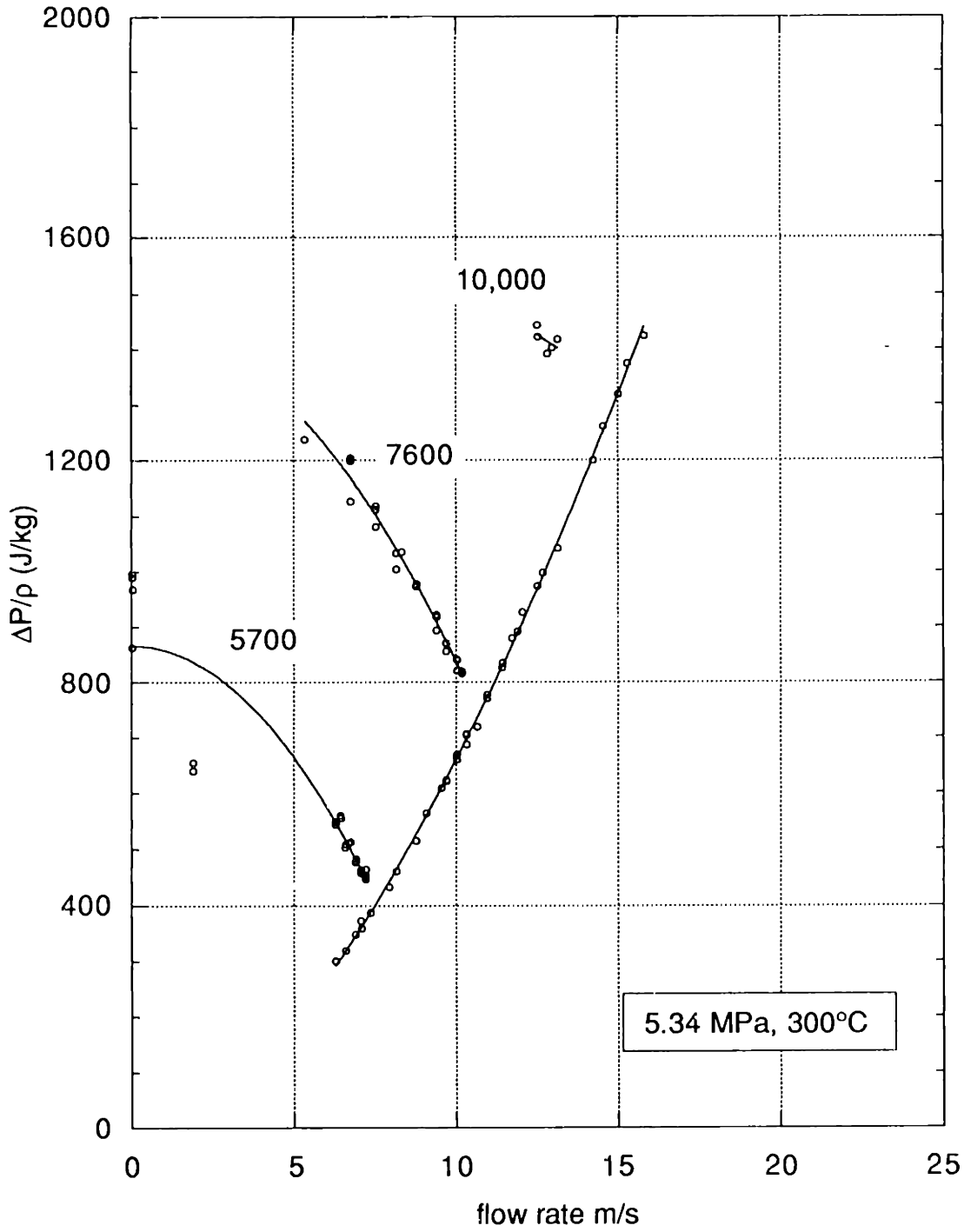

Figure 7.8

Partial circulator map at 5.34 MPa, 300°C

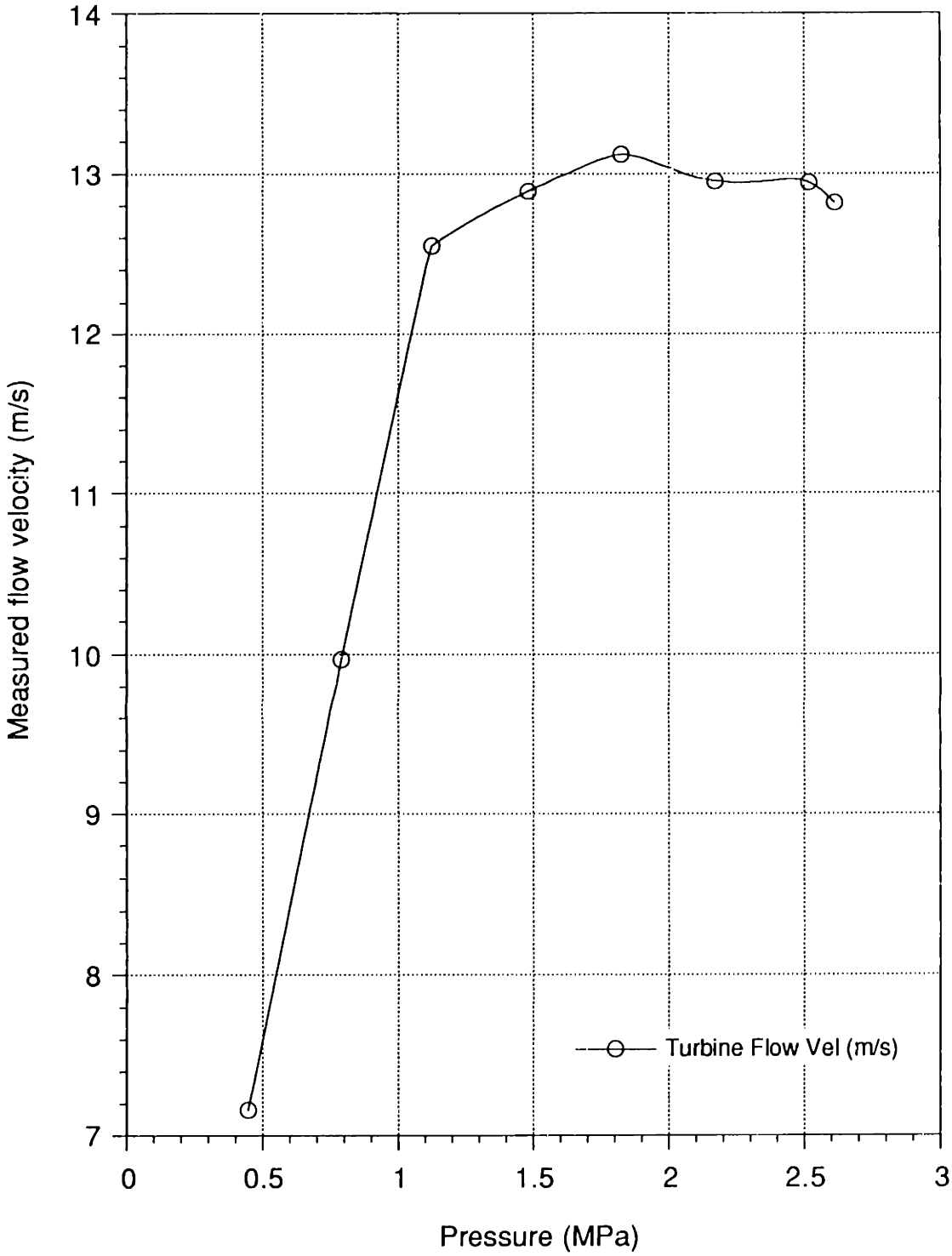

Figure 7.9
Flow rate vs system pressure

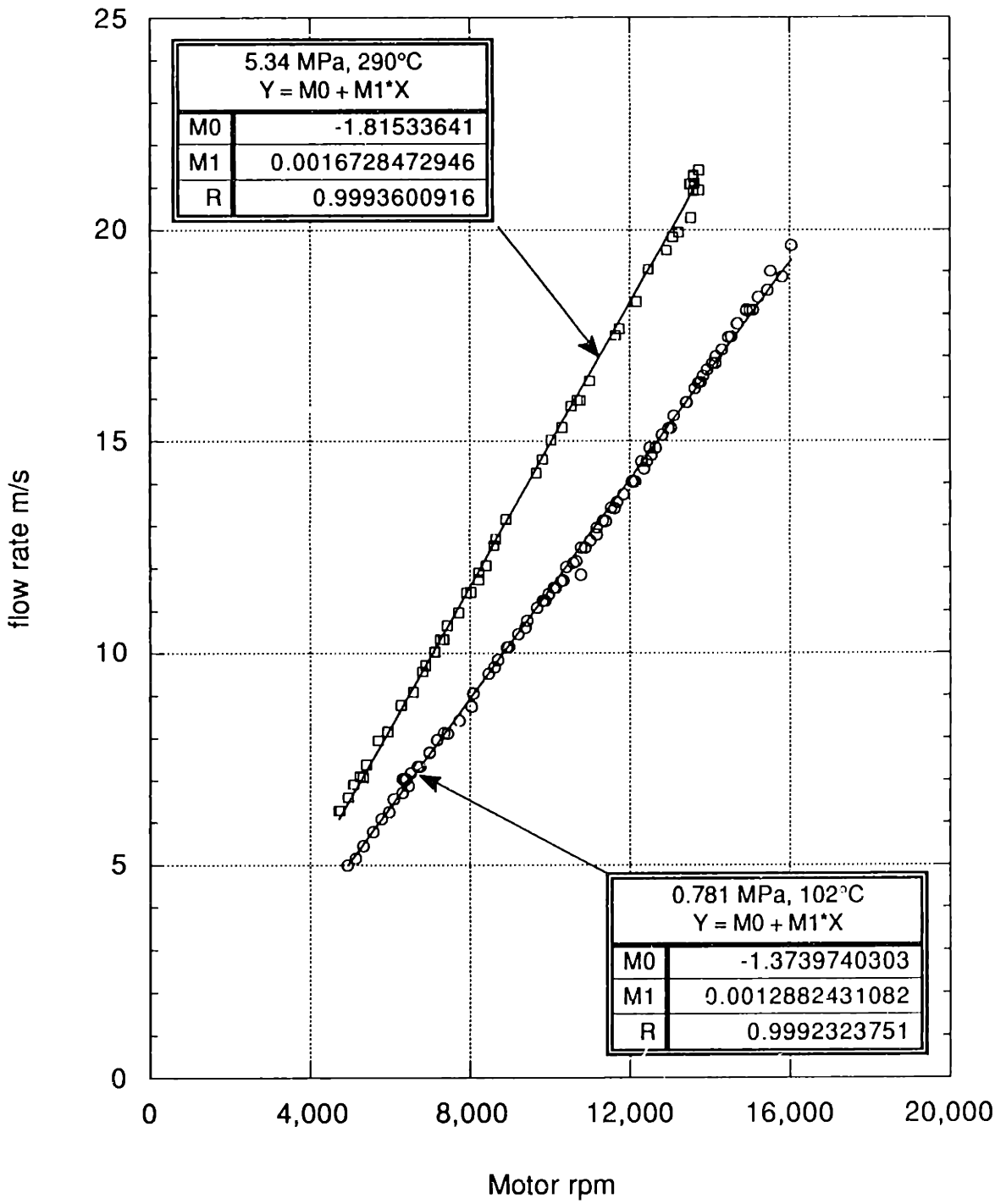

Figure 7.10

Flow vs rpm at two pressures

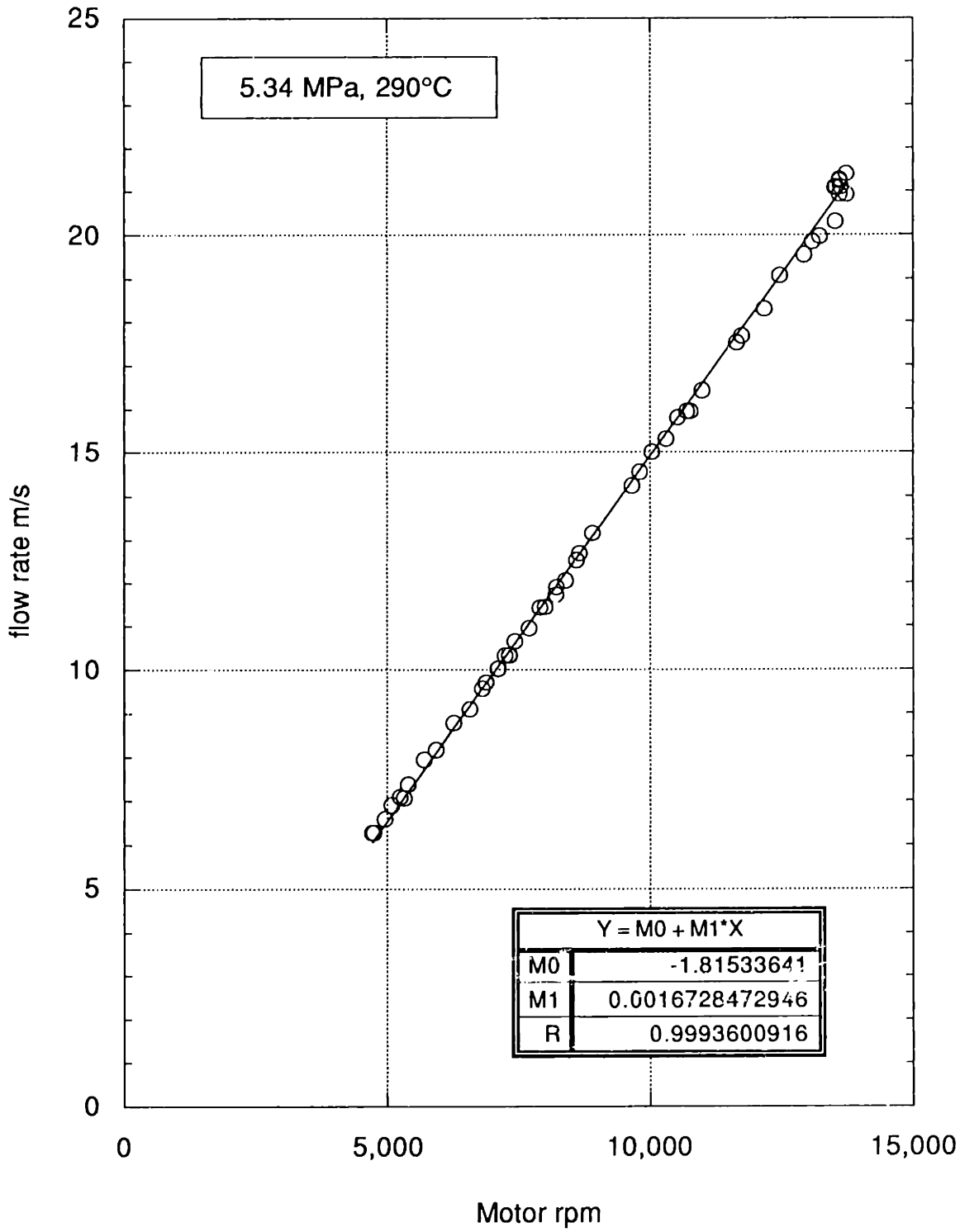

Figure 7.11

Flow rate vs circulator speed at 5.34 MPa, and 290°C

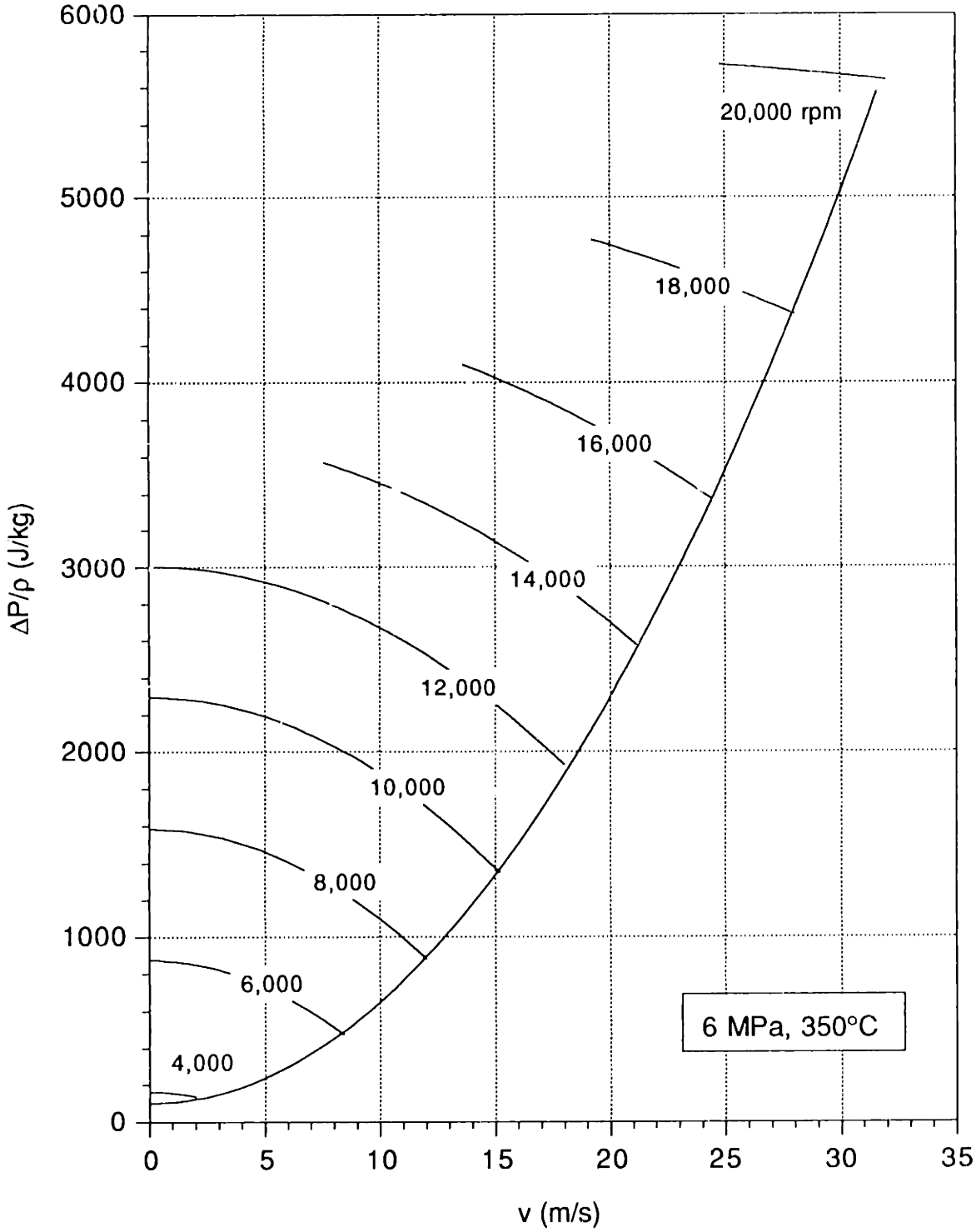

Figure 7.12
Predicted circulator performance at 6 MPa, 350°C

7.1.2 Gas Purity measurement

The gas purity was monitored using the quadrupole Residual Gas Analyzer (RGA). The details of this system were discussed in chapter 6. Here only the typical results are presented. Figure 7.13 shows the background contamination level in the vacuum chamber. Figure 7.14 shows a scan of the loop atmosphere with the background subtracted. If we assume the machine to be properly calibrated, an analysis of the loop atmosphere yields the following composition for the atmosphere, with the quantity of each gas expressed as a fraction of the total pressure

Table 7.1

Preliminary Analysis of Loop Gas Composition

Species	*Fraction of loop pressure*
Helium	99.0%
Nitrogen	0.3%
Oxygen	0.2%
H_2O	0.5%
CO_2	300 ppm
Argon	100 ppm

It is likely that this analysis overestimates the impurity level in the loop, since the RGA, unless compensated, is less sensitive to lower atomic wight gases. Since the gas composition was determined by taking the ratio of each peak area to the total pressure under the spectrum, if the helium peak is smaller than expected, the fractional impurity level will be overestimated. These estimates will be refined when the instrument calibration is complete.

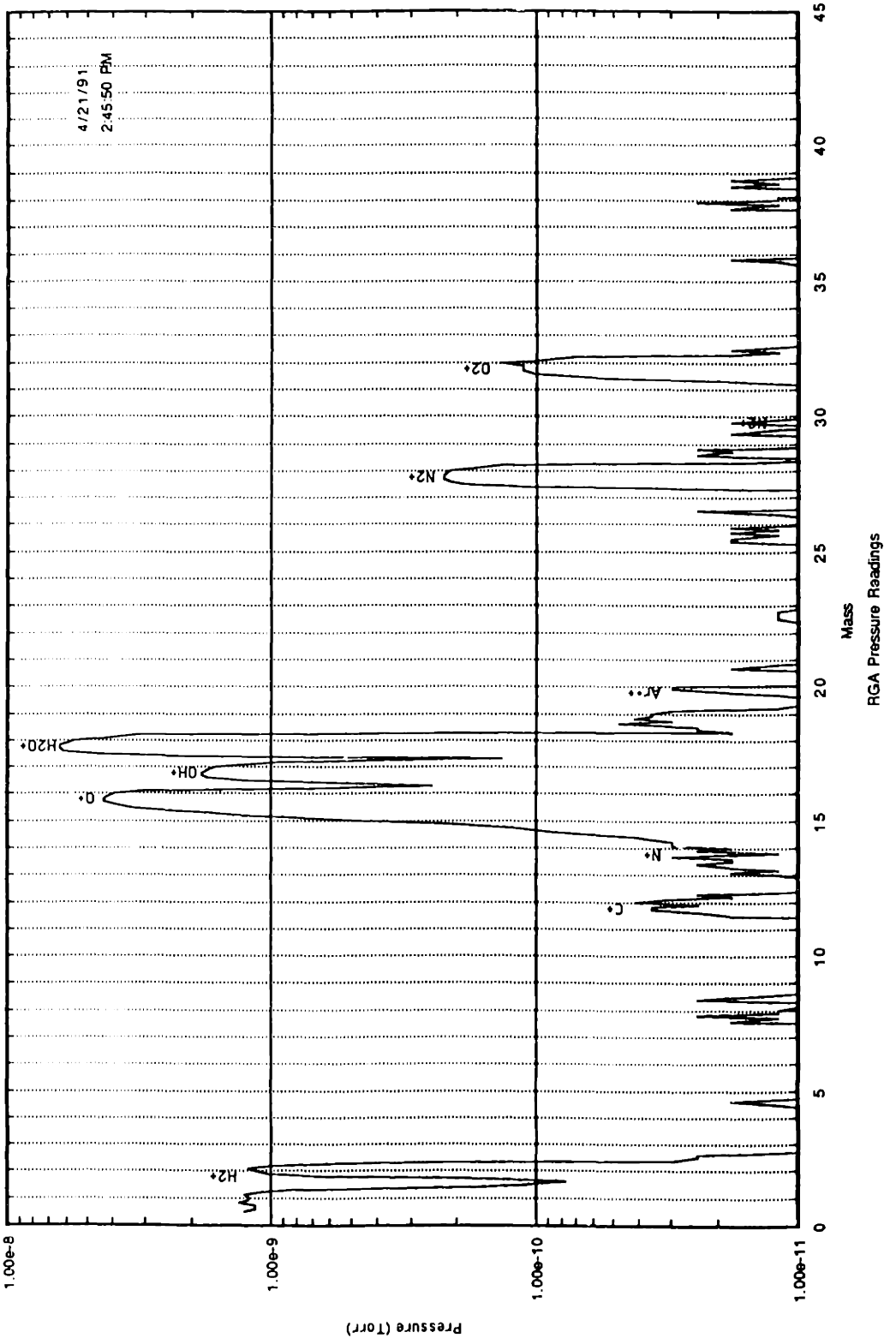

Figure 7.13
Background in the RGA Vacuum Chamber

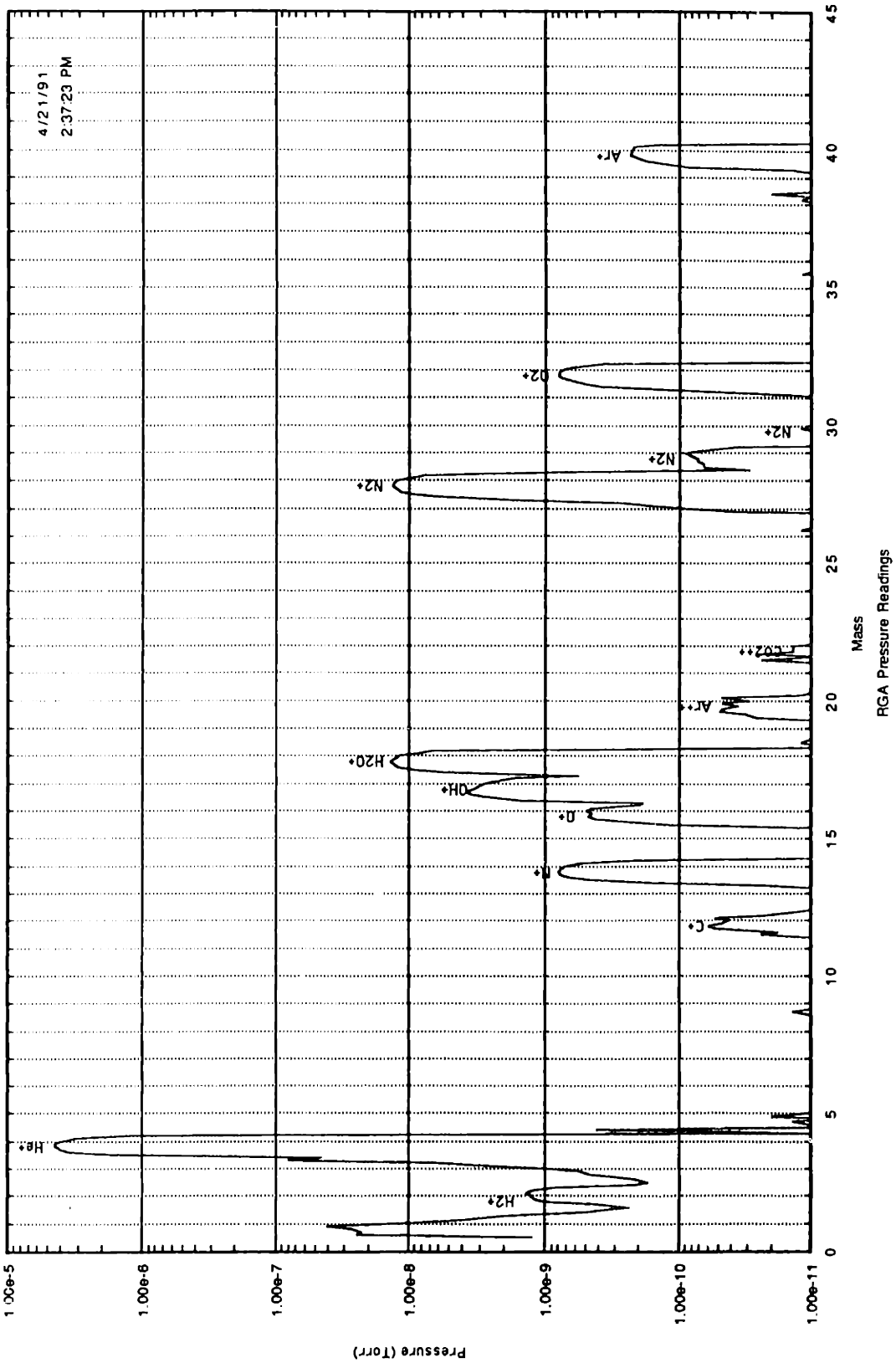

Figure 7.14
Loop Atmosphere with background subtracted

Chapter 8:

RECOMENDATIONS

8.1 Improvements to existing systems

The design of various loop components continues to evolve as additional data is acquired, problems surface, and priorities change. This section details the suggested changes in some of the loop subsystems.

Heaters

While the heater system has worked well in the preliminary testing, certain aspects of the design do not lend themselves well to rapid changes in the test section geometry. The design was based on an attempt to minimize the cost and gamma attenuation of the heaters and their insulation. This was accomplished, but the resulting design, although exceptionally compact and inexpensive, was very labor intensive to install, and has to be completely replaced with each test section. The heaters are built directly on the test section by first wrapping the pipe with two layers of silica tape, followed by the bare wire and several layers of 0.6 mm thick fibrous alumina-silica insulation. This procedure was very time-consuming, particularly the installation of the insulation layers.

The proposed redesign of the heaters would replace the inner silica tape with a ceramic cement coating. This coating could be applied to the test section, then fired in place at 200°C by using the bottom leg heaters to circulate hot helium through the test section. The outer insulation should be bonded with a rigidizer to form it into a more easily handled single piece. Alternately, the fibrous insulation could be replaced with a low-density rigid half-cylinder. The use of larger, rigid insulation would greatly speed the assembly of the heater section. In addition, disassembly of one of the heater sections uncovered some degradation of the inner electrical insulation directly underneath the wires. It is possible that continued operation at temperatures beyond 600°C could cause the insulation to fail, forcing the shutdown of that section. Ceramic cement coatings are available with use temperatures in excess of 1650°C, so their use would extend the temperature range of the heaters.

Circulator

Although a successful design in the aerodynamic sense, the circulator has been a source of mechanical difficulties. Extended operation of the circulator will likely require some improvements to the housing and bearings in order to guarantee good performance.

A number of the problems experienced with the circulator to date have been associated with the difficulty in assuring proper alignment between the drive and the circulator housing. In the early designs, the difficulty of maintaining this alignment was not fully appreciated, and as a result, fairly wide tolerances were specified on a number of components. Figure 8.1 shows the key features of the current design. Proper alignment is controlled by the close fitting of the circulator housing rear plate into a recess on the housing, and by the close fit of this housing into the core barrel ribs at the locations specified by the heavy black arrows. Unfortunately, the tolerances on each of these fits are sufficiently large to present difficulties in proper alignment of the drive shaft, the bearings and the impeller housing. In particular, the fit between the ribs and the housing presents a problem. Since this fit is a close fit between two large diameter cylinders, if the axes of the core barrel and the housing were not precisely co-linear during assembly, the assembly would jam. Avoiding this problem called for increasing the diametral clearance between the parts to allow for small errors in the initial assembly.

The other problem with the current design is it does not provide a good method for observing the behavior of the impeller directly during initial assembly and testing. A design which would allow access to the impeller while running inside its housing would be of great usefulness in the initial testing stages.

The final, and most important consideration for the design is the choice of bearings. As detailed in chapter 5, the design has evolved through using only the motor bearings, using a graphite plain journal bearing, to a low-temperature design utilizing needle bearings. None of these has proved satisfactory. It was hoped in the original design that the loading on the bearings would be sufficiently low that these concepts would be viable. This has not turned out to be the case. More sophisticated bearings will be needed for extended operation at high temperatures. Such bearings, although expensive, are widely available. For our application, tilting pad, gas lubricated hydrodynamic journal bearings are perhaps the best choice. Such bearings have been used in other small helium turbomachines. Coates describes the use of this type of bearing in a prototype 24,000 rpm, 30 kW closed cycle gas turbine. Similar bearings were operated at temperatures of 870°C and speeds to 60,000 rpm in a small argon turbine. [C8]

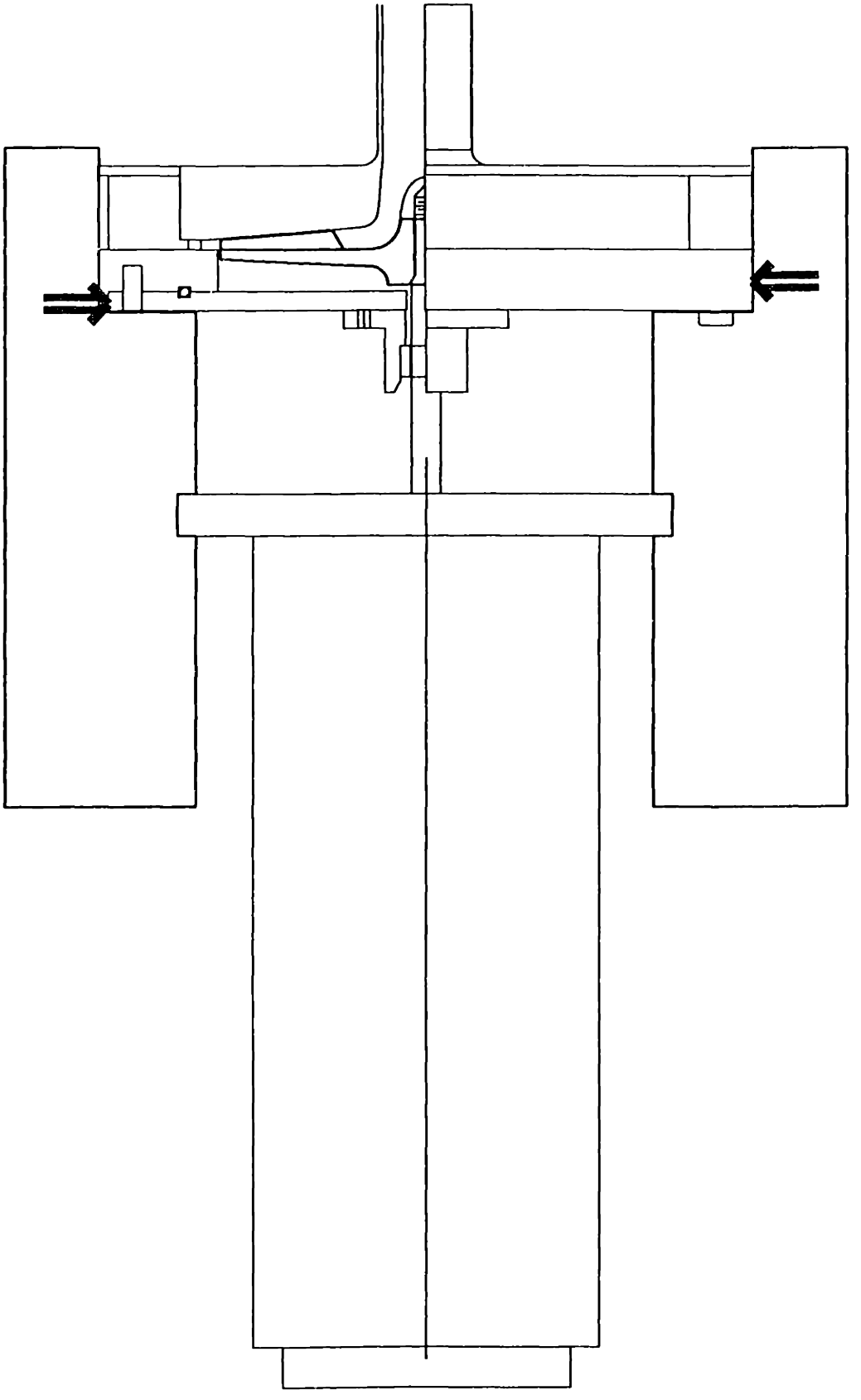

Figure 8.1
Alignment Points in the Current Housing Design

With these considerations in mind, the following design changes are suggested for the next circulator design:

- Rebuild the circulator housing to incorporate a fixed rear plate and a removable front shroud.
- Use dowel pins, rather than concentric cylinders to position the housing radially.
- Use gas journal bearings for radial support of the impeller shaft.
- Incorporate a flexible coupling between the drive motor shaft and the impeller shaft
- Use a hollow impeller shaft

The revised circulator housing is shown in Figure 8.2 The front plate is arranged such that it may be removed to measure the impeller run-out after assembly. Axial positioning of the impeller is still provided by moving the motor in its mount. I believe this to be the simplest possible solution. If this is found to be un-workable, a gas-lubricated thrust bearing could be provided. The shaft is supported radially by two tilting-pad journal bearings, which are mounted in a cylinder attached directly to the core barrel ribs.

The motor shaft is connected to the impeller shaft using a flexible coupling. This compensates for any small misalignments between the motor and the impeller shaft. The motor is mounted in a cylindrical housing with internal helical grooves. Pins on the motor housing mate with these grooves, allowing simple adjustment of the impeller to shroud spacing.

8.2 Additions to loop capabilities

In order to move on to the next phase of research using the DABLE facility, a number of additions to the loop capabilities will have to be made. Among these are the installation of the iodine source, the gamma detector electronics and the hot cell filtration system. In addition, the test section which is currently 304 SS, will have to be replaced with 2.25 Cr-1Mo. These changes will allow a variety of deposition tests to be made, along with investigations of absorption and desorption kinetics at temperatures between 100 and 450°C. It is also likely that a gas cleanup system will be required to maintain the impurity concentrations in the loop atmosphere at an acceptable level. Except for the iodine source, each of these is straightforward to implement. The iodine source should not be a significant problem, as the basic technology has been in use at ORNL for over a year, and the autoclave is an standard product.

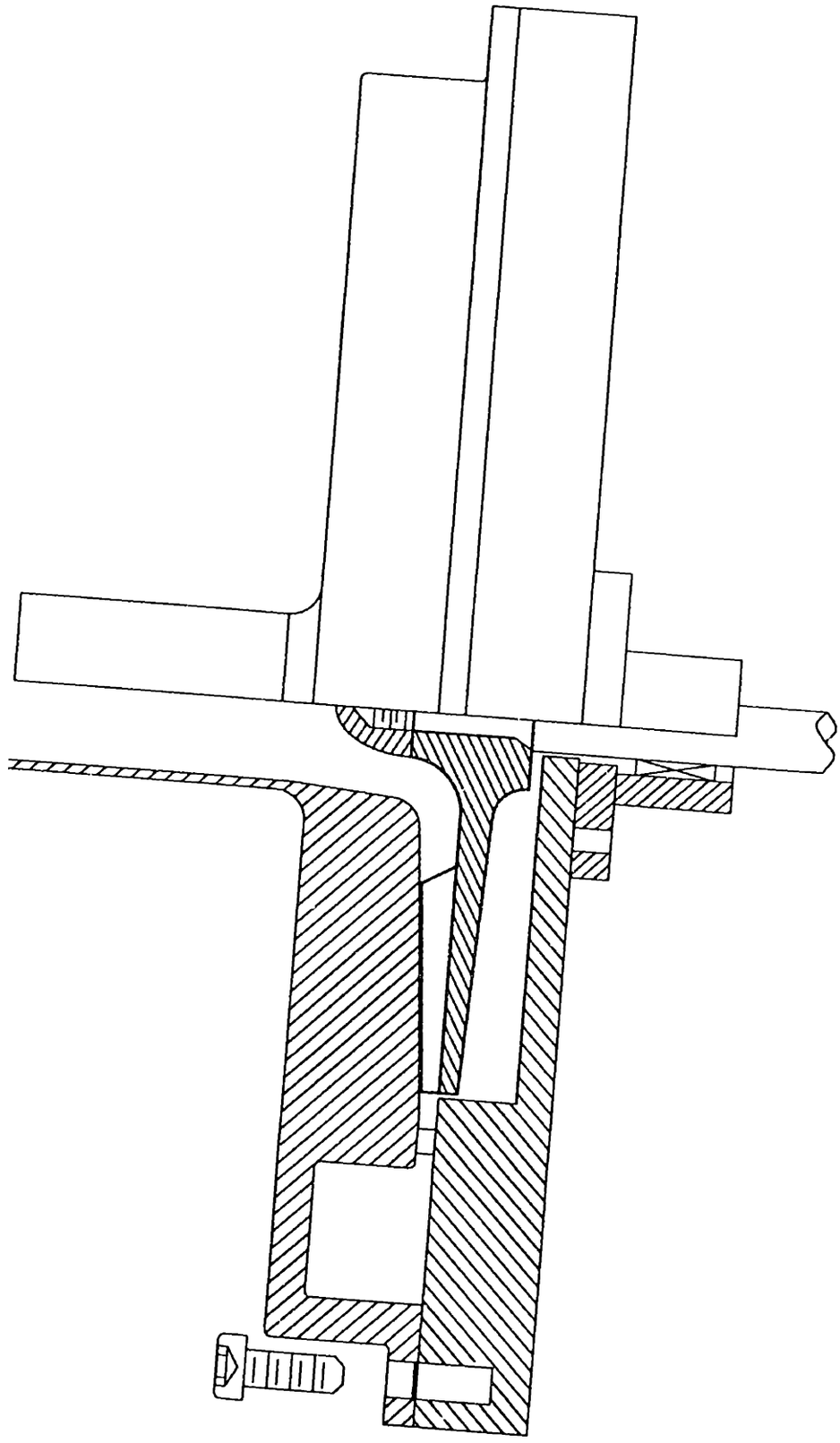

Figure 8.2
Revised Circulator Housing

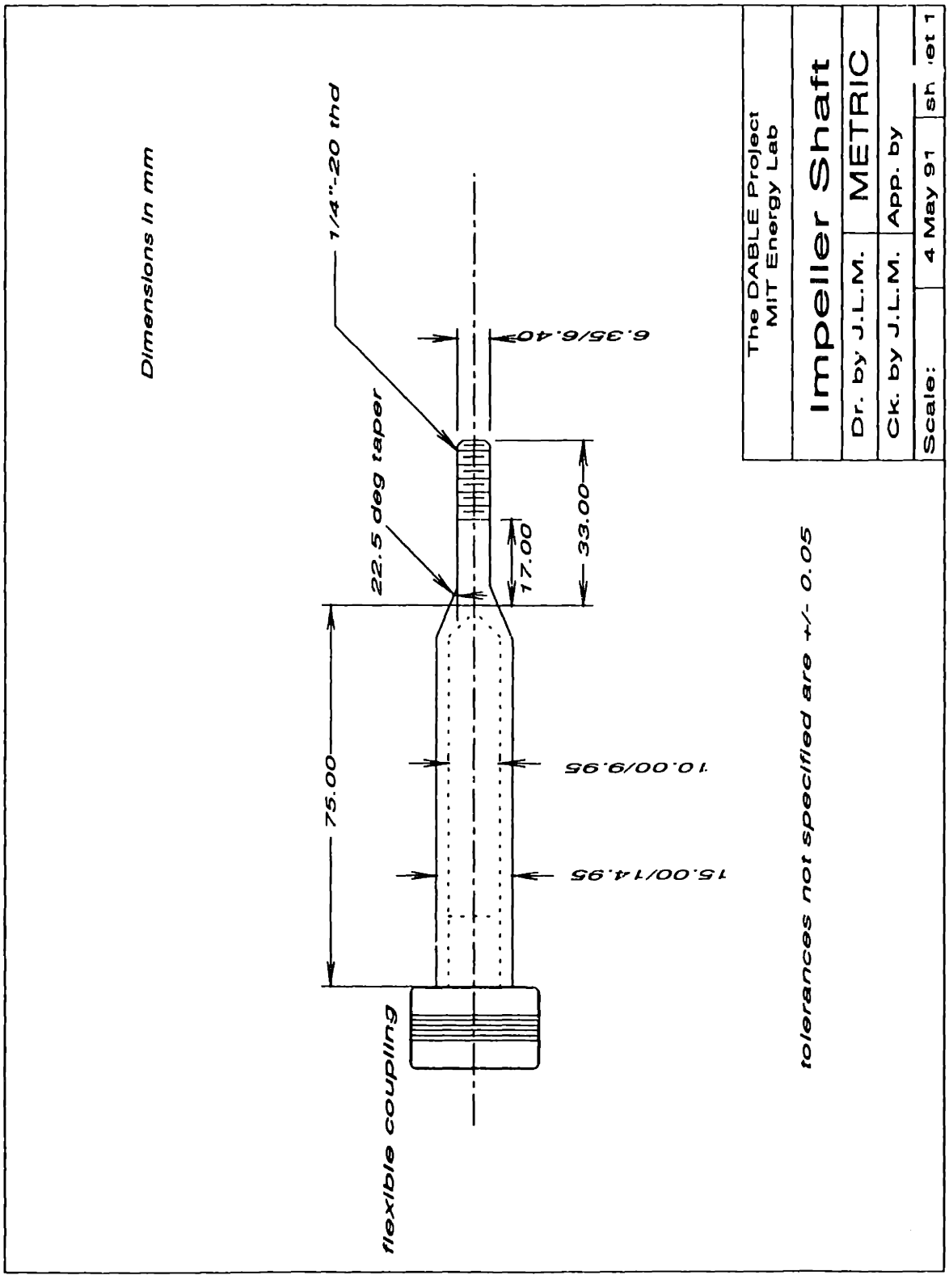

Figure 8.3
New Impeller Shaft Design

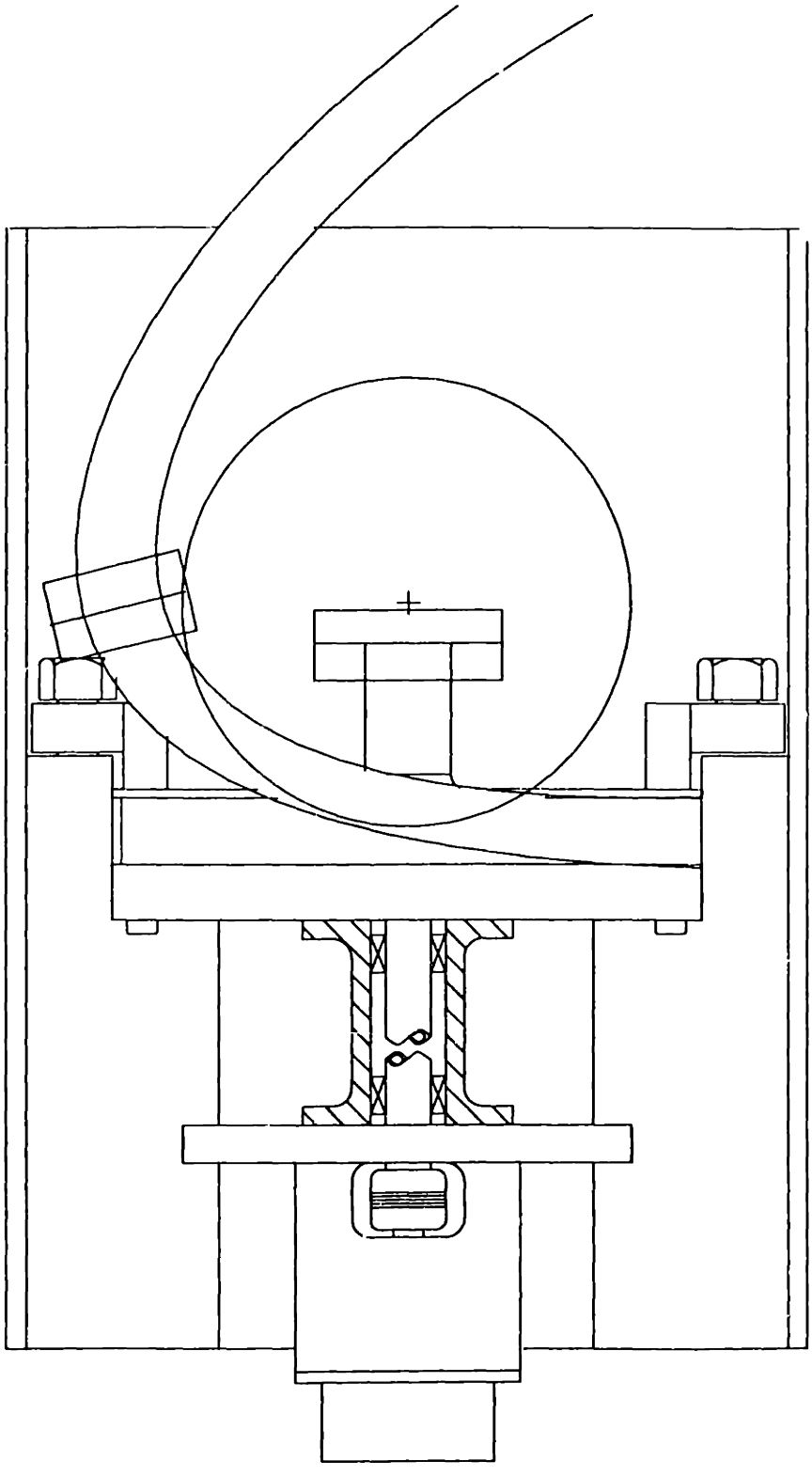

Figure 8.4
Assembly Drawing for Updated Circulator and Bearing Housing

For the longer term work, there are several paths the development of the facility could take. Extensive investigation into lift-off under dusty conditions will almost surely require the use of a full-flow filter to collect the re-entrained particles. We know of no filters which would give an sufficiently small pressure drop that lift-off experiments could be run over a wide range of flow rates, however, their exists some possibility to collect particles by other means, such as impactors. If it were necessary to run the experiments using conventional filters, the loop could be depressurized through the filters. This would necessitate the installation of a blow-down train and appropriate valving.

8.3 Proposed experiments

This section outlines the experiments proposed for the first series of tests in the DABLE loop. It is not intended to be a detailed experiment specification, but rather to outline the investigations we will perform. For the details of the experimental procedure, see reference [H4]. Each of these proposed experiments could provide basic data on a poorly-understood phenomena, and would feed directly into reducing the uncertainty in safety analyses.

We will begin by performing iodine deposition experiments in a clean, dry system with the intent of gathering basic data on the deposition rate under the flow conditions of the loop. These experiments will be performed with the loop essentially isothermal. If steady state is reached quickly enough, deposition at a number of different temperatures will be investigated during the course of single run. The material for these tests will be the currently installed test section, an as-recieved 304 SS pipe. Since this is not a material to be used in the MGR, these tests will be of minimal interest to the HTGR community, but will be very important to our research and the development of experimental procedures. These tests will serve to shakedown the iodine source and to quantify the detection limits for the gamma detector array. Based on the results of these scoping tests, we will replace the test section with a T-22 (2.25 Cr/1-Mo) tube and begin our investigations of iodine deposition on steam generator material. In these tests, we will attempt to determine the sorption isotherms for iodine on T-22, and compare our results with those found by Oak Ridge in smaller tests. By selectively cooling a short length of the test section, we will attempt to create a significant spatial variation in the deposition profile. Then, by reheating this section, we can investigate the desorption kinetics and determine the limits on the fractional deposition change which can be accurately measured.

In the early stages of this testing, the most important contributions will be the accurate measurement of deposition profiles on materials of interest to the HTGR community, under conditions which will not require the order-of-magnitude extrapolations much of the current data base requires. Investigations of the effect of the bulk flow parameters (Reynolds number, mass transfer coefficient, system pressure, etc.) on the deposition kinetics will give basic data necessary to update predictive models for deposition and lift-off. During this phase of the work, existing deposition models will be evaluated, and compared against the data from the DABLE experiments.

After a series of investigations on the basic physics of iodine deposition in clean, dry systems, there are a number of directions the facility might take. Investigations of cesium transport is one obvious choice, however, it remains unclear if the disposal problems can be dealt with in a university setting. Perhaps a better choice is to begin investigations of the effect of dust on the fission product transport. Several aerosol injection systems have been devised for high-pressure use; one could be adapted for use in the DABLE loop. [P1, S4] This would allow a wide variety of investigations on the nature of fission product transport on dust.

Chapter 9:

SUMMARY AND CONCLUSIONS

The modular gas-cooled reactor, particularly in a direct-cycle configuration, has the potential to meet almost all utility requiremtents for a next-generation nuclear reactor. It is relatively small (<450 MWth), it should be easier to license, it has features which will enhance its availablity, and it has the potential to be economically viable. A number of these features stem directly from a design philosophy which emphasizes passive means of minimizing fission product release from the core during accidents. Part of this philiosophy is to rely on mechanistic predictions of fission product release from the primary system, rather than a probablistic analysis of accident frequencies. For this philosophy to be used as a licensing criteria, there must be a sound experimental and theoretical basis for fission product release predictions. The DABLE loop can play an important role in the development of a physical understanding of the controlling parameters.

To some extent, the MGR has been a victim of its own sucess in the reduction of the source term. Steady improvements in fuel quality, thermal hydraulics, and control systems have made the design of a completely new type of reactor possible–a reactor in which massive fuel failure becomes a physical impossibility. It is only after the mechanisms for large releases of radioactivity to the public have been eliminated that one has the opportunity or reason to investigate mechanisms which might contribute to small releases. Plate-out and lift-off certainly fall within this category. The very idea of trying to track fity Curies of cesium blowing around the reactor on dust particles would not occur to an engineer concerned with the penetration of a million-Curie molten core through a pressure vessel wall.

Nonetheless, fifty Curies of iodine or cesium is nothing to be hand-waved away, particularly if the reactor is to operate without a containment. The movement of these isotopes around the reactor circuit determines the maintenance doses, the circulating activity, and ultimately, much of the limited hazard these reactors present to the public. A better understanding of the mechanisms controlling the deposition and lift-off

phenomena would allow better control of the circulating activity, better control of occupational exposure, and might result in reduced risk.

The DABLE loop is uniquely suited for this research. The simplicity of the design, combined with good instrumentation, and a relatively wide operating envelope, allows for an in-depth study of individual effects on the phenomena of interest. There are several directions the facility might take from its current state.

One possible direction for further study is to investigate the adsoprtion and desorption of isotopes on a variety of alloys. By constructing a test section with several alloys, the effect of varying alloy compostion could be studied. The investigation of the effect of surface finish is another study which might be of interest. Previous work has demonstrated the effect of surface finish on oxidation kinetics–it is likely that an effect on deposition would likely be found, also.

To this date, the development of the facility has necessarily focussed on the mechanical aspects of the design. Now, we may begin to turn our attention to the metallurgy of deposition. Particularly for the experiments on iodine, where it is practical to wait several half-lives, the examination of the surface by electron microscopy after deposition could yield insights into the nature of the process.

Physical or chemical removal of fission products by water vapor is an unresolved safety issue in steam-cycle MGR's. With the addition of a water injection system, the DABLE loop could be used to investigate steam-off in non-condensing helium-water mixtures. For condensing mixtures, a gas seal on the circulator shaft would most likely be required to protect the motor.

Conclusions

The DABLE loop is poised to make several key contributions to the study of fission product transport in gas-cooled reactors. The use of a high-temperature, centrifugal circulator greatly simplifies the operation and control of the loop. With the information gained in the development of this circulator, it should be possible to build other circulators of this type which will compete favorably with room-temperature diaphragm compressors for use in recirculating loops. The movable detector array will provide good efficiency and better spatial resolution than has been previously achieved. If the quadrupole RGA proves sufficiently accurate, a new technique will become available for the monitoring of gaseous impurities in the helium stream.

At this stage in the development of the facility, the DABLE project has achieved a number of its goals. The feasibility of operating a high-temperature, isothermal loop has been proven. The mechanical systems necessary to achieve a ~ 5 cm spatial resolution

have been demonstrated. Software to integrate all the functions of the loop has been developed. The loop has been operated at conditions typical of MGR heat exchangers. The practicality of using a quadrupole RGA for monitoring of gaseous impurities has been investigated, although a final conclusion is not yet available.

All of the pieces are in place, or soon will be. With the upgrade of the circulator driver and the addition of the iodine source, the loop will begin the second phase of the project, the investigation of fission product transport in gas-cooled reactors. The results produced in that phase may to make an important contribution to the understanding of fission product transport in gas-cooled reactors, a contribution that could translate into reduced uncertainty, and potentially, reduced risk.

I await the results eagerly.

Appendix 1

Calculations Supporting the Pressure Vessel Design

Table A.1 Stress calculations for the pressure vessel (English units)

Stock 600 lb flange		good design!
		Bolts okay
Stress Calculations		
1.5Sfo	22950.000	
Sfo	15300.000	
SH	8378.171	Longitudinal stress in hub
SR	10044.898	Radial stress in flange
ST	3764.513	Tangential stress in flange
	9211.535	
Design Pressure, P	1160.000	
Design Temperature(°F)	212.000	
Flange Material	carbon steel	
Bolting Material	carbon steel	
Corrosion Allowance	0.000	
Allowable Stresses		
Flange: Operating Temp	15300.000	Sfo
Bolting: Operating Temp	40000.000	Sb
Gasket		.093 diam metallic O-Ring or Equiv.
N	0.093	width of gasket
*b_*	0.093	effective gasket width
G	12.000	diameter at gasket load reaction
*y_*	3000.000	gasket design seating stress
*m_*	2.000	gasket factor
Load and Bolt Calcs		
number of bolts	20.000	
bolt diameter	1.250	
*Bolt Circle, C_*	19.250	
Wm2	10518.052	required bolt load to seat gasket
Hp	16267.921	total joint contact surface comp. load
H	131192.909	hydrostatic end force
Wm1	147460.830	required bolt load, operating
Am	0.263	total required area of bolts (for gasket)
Ab	24.544	cross-sectional area of bolts, (in^2)
W	496132.878	flange bolt design load
Moment		

flange ID, B	11.374	flange ID
flange OD, A	22.000	flange OD
g0	0.688	thickness of hub at small end
g_1	2.188	thickness of hub at back of flange
R_	1.750	radial dist. from hub to BC
E	1.375	radial dstance from BC to Flange OD
*h_*	6.125	hub length
HD	117862.139	hydrostatic end force on area inside of flange
HG	16267.921	gasket load, operating
HT	13330.770	pressure force on flange
hd_	3.594	lever arm
hg_	3.625	lever arm
ht_	3.782	lever arm
MD	423596.527	moment
MG	58971.213	moment
MT	50410.308	moment
Mo	532978.048	total moment
Mo prime	1798481.684	total seating moment on flange
K and Hub factors		
K	1.934	
T	1.532	
Z	1.730	
Y	3.108	
U	3.416	
g_1/g0	3.180	
h0	2.797	hub factor
h_/h0	2.190	
F	0.580	
V	0.040	
*f_*	1.000	
e_	0.207	
d_	113.072	hub shape factor
Stress formula Factors		
*t_*	2.625	flange thickness
alpha	1.544	
beta	1.726	
gamma	1.008	
delta	0.160	
lambda	1.168	
m0_	46859.332	
mg_	158122.181	
Stress Calculations		
1.5Sfo	22950.000	
Sfo	15300.000	
SH	8378.171	
SR	10044.898	
ST	3764.513	
	9211.535	

Table A.2 Equations for calculating stresses in pressure vessels

Stock 600 lb flange	
Stress Calculations	
1.5Sfo	=1.5*Sfo
Sfo	=Sfo
SH	=SH
SR	=SR
ST	=ST
	=MAX(0.5*(SH+SR),(0.5*(SH+ST)))

Design Pressure, P	1160
Design Temperature(°F)	212
Flange Material	carbon steel
Bolting Material	carbon steel
Corrosion Allowance	0
Allowable Stresses	
Flange: Operating Temp	15300
Bolting: Operating Temp	40000
Gasket	
N	0.093
*b_*	0.093
G	12
*y_*	3000
*m_*	2
Load and Bolt Calcs	
number of bolts	20
bolt diameter	1.25
*Bolt Circle, C_*	19.25
Wm2	=b_*PI()*G*y_
Hp	=2*b_*PI()*G*m_*P
H	=G*G*PI()*P/4
Wm1	=Hp+H
Am	=Wm2/Sb
Ab	=PI()*bolt_diam^2/4*num_bolts
W	=0.5*(Am+Ab)*Sb
Moment	
flange ID, B	11.374
flange OD, A	22
g0	0.688
g_1	2.188
R_	=(Bolt_Circle-B-2*g_1)/2
E	=(A-Bolt_Circle)/2
*h_*	6.125
HD	=P*PI()*B^2/4
HG	=Wm1-H
HT	=H-HD
hd_	=(C_-B-g0)/2
hg_	=0.5*(C_-G)
ht_	=0.5*(R_+g_1+hg_)
MD	=HD*hd_

MG	=HG*hg_
MT	=HT*ht_
Mo	=MD+MG+MT
Mo prime	=W*0.5*(C_-G)

K and Hub factors

K	=A/B
T	=(1-0.3^2)*(K^2-1)*U/((1-0.3)+(1+0.3)*K^2)
Z	=(K^2+1)/(K^2-1)
Y	=(1-0.3^2)*U
U	=(K^2*(1+4.6052*((1+0.3)/(1-0.3))*LOG10(K))-1)/(1.0472*(K^2-1)*(K-1)*(1+0.3))
g_1/g0	=g_1/g0
h0	=SQRT(B*g0)
h_/h0	=h_/h0
F	0.58
V	0.04
*f_*	1
e_	=F/h0
d_	=U*h0*g0^2/V

Stress formula Factors

*t_*	2.625
alpha	=t_*e_+1
beta	=4/3*t_*e_+1
gamma	=alpha/T
delta	=t_^3/d_
lambda	=gamma+delta
m0_	=Mo/B
mg_	=Mo_prime/B

Stress Calculations

1.5Sfo	=1.5*Sfo
Sfo	=Sfo
SH	=f_*m0_/(lambda*g_1^2)
SR	=beta*m0_/(lambda*t_^2)
ST	=m0_*Y/t_^2-Z*SR
	=MAX(0.5*(SH+SR),(0.5*(SH+ST)))

Appendix 2

Analysis of Flow Measurement Differences

The flow velocity measurements made from the pitot tube and the turbine flow mter did not agree. There was typically a 10 to 20% discrepancy between the two measurements. A number of hypotheses were advanced to explain the discrepancy, but none were verified. This Appendix details the calculations and experiments used to evaluate the potential sources of errors in the two instruments.

The first of potential source of error in the pitot tube measurement regarded the need to assume the density of the loop atmosphere. This density is calculated from the gas temperature, the loop pressure and, in the case of impurities in the helium, the gas composition. For pure helium, the gas density may be determined from the formula

$$\rho = 48.1394 \frac{P}{T}\left[1 + 0.53x10^{-3} P \left(\frac{T_0}{T}\right)^{1.2}\right]^{-1} \; kg/m^3$$

where P is given in bar absolute, T is in Kelvin, and T_0 is 273.16 K.[Harwell data] Helium is very nearly an ideal gas; if accuracy within 1.2% is acceptable, the perfect gas law may be used in place of the formula given above.

Impurities in the helium will, with the exception of hydrogen, increase its density. The effect a few percent by volume of nitrogen on the density of the mixture is amplified by the ratio of the molecular weights. The density of a helium/air mixture is given by

$$\rho_m = \frac{P_{tot}\left(1 - \frac{p_{air}}{p_{He}}\right)}{R_{He} T}\left(1 + 7.24\frac{p_{air}}{p_{He}}\right)$$

where ρ_m is the density of the mixture, and 7.24 is the ratio of the average molecular weights of air and helium. For partial pressures of the contaminants less than 1%, this formula may be approximated by the more obvious form

$$\rho_m = \rho_{He}\left(1 + 7.24\frac{p_{air}}{p_{He}}\right)$$

Under the conditions most of this work was performed, typical air contamination in the helium was on the order of 1-2%. This would lead to a increase in the mixture density of

7-14%, tending toward the lower end of that range since the primary contaminant was water vapor.

The temperature needed for the density calculation was measured by a thermocouple mounted directly at the pitot tube tip. This measurement is accurate to within ±4 °C. There is the possibility that the gas temperature changes from this value between the two instruments. The pitot tube is mounted on the lower leg of the experiment, just before the circulator. The turbine flow meter is mounted on the test section, approximately 3 meters away. During most of the testing, the heater just in front of the turbine flow meter was not operating, so the gas temperature fell in this section. There is no direct measurement of gas temperature here, but an estimate based on the rate of heat loss through the insulation would indicate a less than 10°C drop over this section. This reduction in gas temperature reduces the volumetric flow rate in the turbine flow meter. Nonetheless, the difference is small, amounting to less than 2% density change at 200 °C.

With each of these factors in mind, the following hypotheses were put forth to explain the discrepancy.

- the gas density is higher than assumed.
- the pitot tube is not well centered.
- the ΔP gauge is not correctly calibrated.
- the gas density at the measuring points is different
- the turbine flow meter is not reading accurately
- the turbine flow meter is incorrectly calibrated.

All but the last of these was rejected. The gas density may vary due to contamination, errors in temperature measurement, and errors in the total pressure measurement. Each of these was investigated independently. The total pressure measurement was checked with a test gauge calibrated to within 0.0138 MPa. The temperature measurement was accurate to within 4 °C, with a potential for an additional 10°C difference between the two measurement positions. Gas contamination could have raised the density by ~10% For the worst case, one-sided error in each of these measurements, the error in density is ~12%. The velocity measured by the pitot tube is given by

$$v = \sqrt{\frac{2\Delta p}{\rho}}$$

where Δp is the diffrence between the measured total and static pressures, and ρ is the gas density. Because of the square root dependence of the velocity on the density, the 12% error in density gives only a 5.8% error in flow velocity.

The flow velocity measured by the pitot tube is the flow velocity at the pipe centerline. The velocity measured by the turbine flow meter is the average flow velocity. The two may be correlated by assuming a turbulent velocity profile. For this calculation, a simple power law expression of the form

$$\frac{u}{u_{max}} = \left(\frac{r}{r_0}\right)^{1/n}$$

where $1/n \approx \sqrt{f}$, the friction factor.[P3] By integrating this expression from the pipe wall to the centerline, the following simple expression may be derived relating the average and maximum velocities

$$\frac{u_{avg}}{u_{max}} = \frac{2n}{2n+1}$$

For helium flow at 350°C, 6 MPa, and 10 m/s, the Reynolds number is 3.3×10^4, and the friction factor is 0.0235, for an n of 6.5. The ratio of the average flow velocity to the maximum flow velocity is then about 0.929. n is a slowly varying function of Reynolds number for flows above 10 m/s, ranging from about 6 to 7 over most of the conditons of interest. The ratio of mean to maximum flow velocity then varies from 0.923 to 0.933.

In addition to the above analysis, a number of tests were run to reject independently the possible effects on the density calulation. Tests were made in air to isolate the effect of gas compostion, at room temperature to isolate the temperature effects and at various pressures to isolate the pressure effects. Of these, only the pressure was seen to have an effect on the system. Higher pressures extended the linear range of the turbine flow meter to lower flow rates. The ΔP gauge was calibrated both from the manufacturer's electrical calibration and from a water manometer. Both agreed within the accuracy of the device (1% or 0.048 kPa). Positioning accuracy with the pitot tube is unlikely to be an effect, since tube is not particularly sensitive to angular errors of up to 30°. [United Sensor] In addition, radial positioning errors lead to lower flow rates than expected, while the errors observed were all in the opposite direction.

References

[A1] AERE Harwell Labs, Reactor Physical Data (Excerpts from Harwell report TRG 1000) , KFA 1979

[A2] Arpaci

[B1] K. Bammert, G. Krey, and K.D. Küper, Performance of high-temperature reactors with helium turbines, Advanced and High-Temperature Gas-cooled Reactors, IAEA, 1969

[B2] H.G.A. Bates, W. Betteridge, R.H. Cook, L.W. Graham, and D.F. Lupton, The Behavior of Metals in High-Temperature Reactor Helium for Steam Generators, Nuclear Technology, 28, March 1976, 424-440

[B3] R.J. Blanchard, In Pile Loop COMEDIE, IAEA Specialist's Meeting on Fission Product Release and Transport in Gas-Cooled Reactors, 1985

[B4] H.L. Brey and H.G. Olson, The Fort St. Vrain High Temperature Gas-cooled Reactor: XIII. Radiological and shielding performance of Fort St. Vrain, Nuclear Eng. and Design 72 (1982) 147-152

[B5] F.G. Brightman, C.J. Chapman, J.A. Garland, R.Hargreaves, and E.J. Higham, The Windscale AGR concluding experiments: circuit activity measurements, Gas-Cooled Reactors Today, Vol 3, 43-52

[C1] M. Cappeleare, M. Perrot, and J Sannier, Behavior of Metallic Materials between 550 and 870°C in High-Temperature Gas-Cooled Reactor Helium under Pressures of 2 and 50 Bar, Nuclear Technology, 66 Aug 1984, 465-478

[C2] C.J. Chapman, D.V. Freck, and R.L. Woolley, Progress in research on the retention of caesium and iodine fission products by the gas circuit surfaces in AGR's, Gas-Cooled Reactors Today, Vol 3,59-66

[C3] J.W. Cleaver and B. Yates, Mechanism of Detachment of Colloidal Particles from a Flat Plate in Turbulent Flow, Journal of Colloid and Interface Science, Vol 44, No 3, Sept 1973, 464-474

[C4] S.D. Clinton, J.C. Mailen, T.V. Dinsmore, Iodine Adsoprtion/Desoprtion and Lift-off from 2.25 Cr -1 Mo Alloy in a Bench-Scale Facility, draft of a report of milestones 1601.2.14 and 1601.2.15, July 1989

[C5] P.N. Clough and E.M. Hood, Modelling of Iodine Chemistry and Plateout in a CAGR, IAEA Specialist's Meeting on Fission Product Release and Transport in Gas-Cooled Reactors, 1985

[C6] P.N. Clough, E.M. Hood, and A.R. Taig, Plate-out modelling in assessing the consequences of hypothetical AGR accidents, Gas-Cooled Reactors Today, Vol 3, 53-48

[C7] E.R.Corino and R.S. Brodkey, A visual investigation of the wall region in turbulent flow, Journal of Fluid Mechanics, 37, 1969, 1-30

[C8] N.H. Coates, J. McGee, J. W. Eckerd, Bureau of Mines Program for Developing the Closed Cycle Gas Turbine, Advanced and High-Tempertaure Gas-cooled Reactors, IAEA, 1969

[D1] G. Dibelius, S. Förster, J. Heil, K.U. Schneider, Gas-cooled reactors with gas turbines using helium, neon or carbon dioxide, Advanced and High-Tempertaure Gas-cooled Reactors, IAEA, 1969

[E1] J. Engelhard, K, Krüger, H. Gottaut, Investigation of the impurities and fission products in the AVR coolant gas at an average hot-gas temperature of 950°C, Nuclear Eng. and Design, 34, (1975) 85-92

[E2] J. Elson, R. Fieldhack, J. Guillen, E. Love, J. Martin, E. Tanker, DABLE (Deposition and Blowdown/Lift-off Experiment), Final Report for MIT Class 22.033, June 1986

[F1] K.N. Fleming, HTGR Accident Initiation and Progression Analysis Status Report, GA-A15000, April 1978

[G1] J.A. Garland, A.C. Wells, J.B. Hedgecock, Behavior of Praticles in a Commercial Advanced Gas Reactor, IAEA Specialist's Meeting on Fission Product Release and Transport in Gas-Cooled Reactors, 1985

[G2] D.T. Goodin and H. Nabielek, The performance of HTR fuel in accidents, HBK-TN-19/85, Dec 1985

[G3] Gottaut and Wawrzik, Ablagerungsloop VAMPYR II im AVR, HTR-Anlagen

[H1] F.W. Haase, Versuchsstand zur Spaltproductablagerung, HRB report 645-107, 1981

[H2] F.W. Haase, Auswertung der Laminar-Loop-Experimente, HRB report 205-007

[H3] D.Hanson, Plateout Analytsis for PWS FP-4 and CC1, GA 907518

[H4] D Hanson, Test Specification for MIT "DABLE" Loop, DOE-HTGR-88396, 1990

[H5] W.W. Hudritsch, PADLOC, a one-dimensional computer code for calculating coolant and plateout fission product concentrations, part II, GA-A14401, Sept, 1981

[H6] J.N. Hurst, Some considerations affecting the integration of gas turbines with direct-cycle gas-cooled reactors, Advanced and High-Tempertaure Gas-cooled Reactors, IAEA, 1969

[H7] D.L. Hanson, Results of the General Atomic Deposition Loop Program, GA-A13140, April 1976

[I1] N. Iniotakis, et al, Initial Results of Investigations into Fission Product Deposition in In-Pile Experiments, Nuclear Engineeering and Design 34 (1975) 169-180

[I2] N. Iniotakis, C.B. von der Decken, K. Röllig, H. J. Schlesinger, Plate-out of fission products and its effect on maintenance and repair, Nuclear Engineering and Design 78 (1984) 273-284

[I5] M.G. Izenson, D.D. Lanning, L.M. Lidsky, and J.L. Maneke, Identification of the sfatey requirements of a new reactor concept, the MHTGR as an example, MIT-NPI-TR-006

[J1] W. Jansen, Rotating stall in a vaneless diffuser, Trans ASME J. Basic Eng, 86, 750-758

[L1] L.M. Lidsky, D.D. Lanning, J.E. Staudt, and X.L. Yan, A direct-cycle gas turbine power plant for near-term application: MGR-GT, Energy 16, 1991, 177-186

[L2] E. Love, Final Report for Special Problem 22.901, MIT Department of Nuclear Eng., 1987

[M1] J.C. Mailen, personal communication to J.L. Martin, May 1990

[M2] J.C. Mailen, Update on Methods for Generating Iodine, internal report to DABLE Project, July 90

[M3] J.L. Maneke, PhD Thesis, MIT Department of Nuclear Engineering, 1988

[M4] J.L. Martin, Software for the DABLE Loop, internal report to LM. Lidsky, June 1991

[M5] J.L. Martin, L.M. Lidsky, and D.D.Lanning, MHTGR Plateout and Lift-off: Data Needs and Experimental plans, NUREG CP-0091

[M6] G. Melese and R. Katz, Thermal and flow design of helium-cooled reactors, AMerican Nuclear Society, IL, 1984

[M7] B.F. Meyers, Personal communication to J.L. Martin, Feb 1989

[M8] B.F. Meyers, Personal communication to J.L. Martin, Apr 1989

[N1] H. Nabielek (ed) , US/FRG Experts Meeting on Fuel Performance under Accident Conditions, HTA-IB-2/90 June 1990

[N2] H. Nabielek, W. Schenk, W. Hewit, A-W. Mehner, D.T. Goodin, The performance of high-temperature reactor fuel particles at extreme temperatures, Nuclear Technology, 84, Jan 1989, 62-81

[N3] H. Nabielek, G. Kaiser, H. Huschka, H. Ragoß, M. Wimmers, W. Theyman, Fuel for pebble bed HTR's, Nuclear Engineering and Design 78 (1984)

[O1] M.F. Osborne, R.B. Briggs, and R.P. Wichner, "Iodine Soprtion on Low Chromium Alloy Steel", ORNL/TM-7755 Oak Ridge NAtional Laboratory, Jan 1982

[P1] M.E. Phillips, Modelling of Cesium Deposition in CAGR Reactor Circuits, IAEA Specialist's Meeting on Fission Product Release and Transport in Gas-Cooled Reactors, 1985

[P2] W.H. Press, B.R. Flannery, S.A. Teukolsky, W.A. Vetterling, Numerical Recipies in C: The Art of Scientific Computing, Cambridge University Press, 1988

[R1] H. Ragoß, Description of Particle Behavior and Release characteristics as Used in Radiological Analysis for the HTR Modul, US/FRG Experts Meeting on MHTGR/HTR Fuel Performance under Accident Conditions, ORNL June 1989, HTA Interner Bericht, HTA-IB-02/90

[R2] J. Reed, D. Hall, M.W. Reeks, The Variation of Particle Gas-borne Concentration with Time in a Gas-cooled Reactor, IAEA Specialist's Meeting on Fission Product Release and Transport in Gas-Cooled Reactors, 1985

[R3] K. Röllig, A. Christ, F.W. Haase, and J. Wiedmann, Caesium Deposition on HTR Primary Circuit Materials, IAEA Specialist's Meeting on Fission Product Release and Transport in Gas-Cooled Reactors, 1985

[S1] W. Schenk, Experimental requirements for accident condition testing with irradiated fuels, US/FRG Experts Meeting on Fuel Performance under Accident Conditions, H Nabielek (ed) HTA-IB-2/90 June 1990

[S2] W. Schenk, D. Pitzer, H. Nabielek, Fission product release profiles from spherical fuel elements at accident temperatures, KFA report Jül-2234, 1988

[S3] W. Schenk and H. Nabielek, Accient simulation testing with spherical HTR fuel elements, in KFA annual report 1986/87, Kerforschungsanlage Jülich, 1987

[S4] A. Schneider, A.B. Dewald, Jr, A.E. Levin, A Study of Dust Formation in High-Temperature Gas-Cooled Reactors, Final report of project E25-661), Georgia Tech School of Nuclear Eng, 1988

[S5] Schreiber, Nachrechnung des Versuchs VAMPYR II-01 mit PATRAS, Interatom note 70.04311.0

[S6] L.R. Shepard, Modular high-temperature gas-cooled reactor, Nuclear Energy, 27, 1988, 37-47

[S7] G. Skyrme, Attachment of Gaseous Fission Products to Aerosols, IAEA Specialist's Meeting on Fission Product Release and Transport in Gas-Cooled Reactors, 1985

[S8] J. Staudt, , Ph.D. Thesis MIT Department of Nuclear Engineering, 1987

[T1] J. D. Thorn, K. Prince, and G. Coast, Nuclear gas turbine concepts, Advanced and High-Tempertaure Gas-cooled Reactors, IAEA, 1969

[T2] R.F. Turner, Requirements for fuel materials performance in the MHTGR, US/FRG Experts Meeting on Fuel Performance under Accident Conditions, HTA-IB-2/90 June 1990

[U1] United Sensor, Pitot-Static Pressure Probes, Bulletin 1. 6-83 United Sensor Div, United Electric Controls Co, Watertown, MA

[W1] D.G. Wilson, The design of high-efficiency turbomachinery and gas turbines, MIT Press, Cambridge MA

[Y1] X.L. Yan, K. Kunitomi, L.M. Lidsky, MGR-GTS: An improved direct Brayton-cycle nuclear power plant, draft to be published as a MIT report

[Y1] X.L. Yan and L.M. Lidsky, Highly efficeint automated control for a MGR gas turbine power plant, Presented at the International Gas Turbine and Aeroengine Congress and Exposition, June 1991